Molecular Modeling of Nanostructures, Polymer Electrolytes, and Ionic Liquids for Energy, Environmental, and Catalysis Applications

Hadi Abroshan

April 2017

A dissertation submitted in partial fulfillment
of the requirements for the degree of
Doctor of Philosophy

In the subject of
Chemistry

Carnegie Mellon University
Pittsburgh, PA 15213

Thesis Committee:
Dr. Hyung J. Kim, Advisor
Dr. Emile L. Bominaar, Chair
Dr. David J. Yaron
Dr. Rongchao Jin
Dr. Peng Liu, University of Pittsburgh

Dedicated to my parents and family for their continuous support and help

To anyone how believes in "Peace, Love, and Friendship" for everyone

Abstract

This thesis centers around the structural, electronic, and physicochemical properties of some nanostructures, polymer electrolytes, and ionic liquids for energy, environmental, and catalysis applications. A variety of theoretical tools are employed to enable predictive study, design, and development of the systems. Theoretical concepts are developed for rational explanation of reaction mechanism, surface activity, ionic conductivity, formation, and fragmentation of the materials with respect to structure-activity and structure-selectivity correlations. The outline of this thesis is as follows:

First, the structural stability of isoreticular metal organic frameworks (IRMOFs) confining ionic liquids (ILs) inside their nano-porous cavities is studied. It is shown the IRMOFs are structurally unstable and deforms dramatically from its crystal structure in the presence of ILs. Simulation results also show that metallic parts of IRMOF-1 mainly interact with anions. These results raise an important question if IL/IRMOF composites are good candidates for gas storage or separation.

Second, interactions of the lithium bis(trifluoromethane sulfonyl)imide ($LiTf_2N$) salt with polyethers are investigated to shed light on the origin of difference in ionic conductivity of the two electrolytes: (1) polyethyleneoxide (PEO) and (2) perfluoropolyether (PFPE). Results indicate that substitution of hydrogens by fluorines leads to less interaction of cation Li^+ with the polymers, which provide an atomistic understanding of experimental ionic conductivity results.

Third, $Au_{25}(SR)_{18}$ nanoclusters with atomic precision is served as a model system to scrutinize structure-reactivity correlation of thiolate protected gold nanoclusters. In

particular, the promotional catalytic effect by imidazolium-based ILs, transition metal ions, and aromatic thiolate ligands are studied. Results show the ILs and the ions can significantly enhance activation of the nanoclusters at relatively low temperatures via partial removal of "Au-SR" units from Au_{25} cluster. Further, guidelines are offered for tailoring nanoclusters' properties by ligand engineering for specific applications.

Fourth, controllable incorporation of a single dopant metal to specific sites of gold nanoparticle is studied. A centrally hollow, Au_{24} nanoparticle is used to investigate single atom shuttling in/out of the nanoparticle. Using Ag and Cu as the tracers, the pathways of single atom shuttling are mapped out. The results not only demonstrate single-atom level doping via hollow nanoparticles, but also reveal the intriguing atom shuttling behavior.

Finally, mechanistic insights into promotional effects of ionic liquids on transesterification of cellulose is provides. Results explains IL anions play the most crucial role to facilitate the reaction. This study provides molecular insights for experimentalists to optimize reaction conditions of protocols of cellulose modifications using ILs.

I believe a key element to research is collaborating with chemists in other fields, as complex problems require input from many chemists with different specialties. I have had the opportunity to collaborate closely with experimental groups at Carnegie Mellon University (Prof. Rongchao Jin), Anhui University (Prof. Zhu), Dalian Institute of Chemical Physics (Prof. Gao Li), and Kanazawa University (Prof. Kenji Takahashi) to develop the third-to-fifth projects mentioned above. Our collaborative works require clearly communicating the intrinsic principles behind the complex results. This involve regular exchanges of different viewpoints to establish guidelines for the development of materials with desired performance. This thesis emphasizes on the computational contribution to the projects.

Acknowledgments

It would not be possible to succeed completion of my PhD journey without the wonderful contribution of many extraordinary people, who guided and supported me through my academic and personal life.

I like to thank Dr. Hyung J. Kim for being my PhD advisor and guiding me towards the right path to explore computational physical chemistry. Dear Hyung, you are an inspirational teacher for me, and I am always very grateful to you for all the hard work and efforts you have done to educate me. I never forget your inspirational words, motivational advice, and never-ending support.

I was honored to have Dr. Emile L. Bominaar, Dr. Rongchao Jin, Dr. David Yaron, and Dr. Peng Liu as members of my thesis defense committee. Thank you for your help in progress towards my final goal, to be a better physical chemist.

Many thanks to my experimental collaborators, Dr. Rongchao Jin, Dr. Mark Bier, Dr. Kenji Takahashi, Dr. Gao Li, Dr. Manzhou Zhu, Dr. Shuxin Wang, Dr. Ryohei Kakuchi, Logan D. Plath, Shuo Zhao, Yongbo Song, and Qi Li. The collaborations with the leading experimental groups provided me a wonderful opportunity to strength my knowledge and to work on cutting-edge and interesting research topics.

Dr. Rea Freeland’s regular thoughtful guidance is greatly appreciated. I like to thank Valerie Bridge, Brenda Chambers, Timothy Sager, Patsey Haddock, and Sara Wainer. I do not know how can I ever thank you enough for all you've done for me. You have been extremely supportive through difficult and stressful time. Thank you!

I am always very grateful to my professors of undergraduate studies in University of Mohaghegh Ardabili, Dr. Habibollah Eskandari, Dr. Abolfazl Bezaatpour, Dr. Yagoub Mansoori, Dr. Gholamhassan Hassan Imanzadeh, Dr. Mohammad Reza Zamanloo, Dr. Aziz Habibi-Yangjeh, Dr. Davod Seifzadeh.

I am thankful for my fantastic friends who always encourage and support me, Dr. Fazel Shojaei, Ali Rezaei Mazarei, Dr. Farhad Taher Ghahramani, Dr. Farid Taherkhani, Dr. Hamed Akbarzadeh, Mohammad Taghi Sharbati, Jon Willcox, Dr. Matteus Tanha, Dr. Lea Veras, Dr. Jose Flores, Dr. Sang-Won Park, Dr. Gizelle Sherwood, Dr. Nicolae Albu, Dr. John Pettersson, Andrew DeYoung, SouDe Dadras, Dr. Reza Nourjou, Christopher Collins, Haichen Li, Kevin Hunter, Lillian Crawford, Dr. Luoting Fu, Dr. Yang Yang, and Kheyam Nariman.

And Finally, I thank very much my parents, Shokat and Hamdollah, and my sister and brother, Azam and Ehsan. I am truly blessed to be your son and brother. Needless to say that any achievements that I have made in my life is because of your love, guidance, and support. Thank you very much!

Table of Contents

List of Tables

List of Figures

Chapter 1: *Structural stability of ionic liquid/IRMOF-1 composites*

1.1 Abstract

Structural stability of isoreticular metal organic frameworks, IRMOF-1 and IRMOF-10, confining ionic liquids (ILs) inside their nano-porous cavities is studied via molecular dynamics (MD) simulations. Imidazolium- and pyridinium-based ILs, including $BMI^+PF_6^-$, BMI^+Br^-, $BMI^+Tf_2N^-$, BMI^+DCA^-, and $BuPy^+Tf_2N^-$ (BMI^+ = 1-butyl-3-methylimidazolium, PF_6^- = hexafluorophosphate, Br^- = bromide, Tf_2N^- = bis(trifluoromethylsulfonyl)imide, DCA^- = dicyanamide, and $BuPy^+$ = N-butylpyridinium), at different loadings are considered. It is found that IRMOFs are structurally unstable and deform dramatically from their crystal structure in the presence of ILs. The interactions between the metallic parts of IRMOF and IL anions play a major role in structural disruption and collapse of these MOFs. Thus elongated anions such as Tf_2N^- and DCA^- that can interact with two different metal sites tend to lower IRMOF stability compared to spherical anions Br^- and PF_6^-. A further analysis via density functional theory (DFT) and *ab initio* molecular dynamics (AIMD) simulations lends support to the MD results for structural instability of IRMOFs in the presence of ILs.

Keywords: IRMOF-1, Ionic Liquid, molecular dynamics simulation, DFT calculations, *ab initio* molecular dynamics, structural stability

1.2 Introduction

Metal-organic frameworks (MOFs) are a relatively new class of nano-porous materials in which metallic components are connected together by organic molecules, called “linkers”. The use of different building blocks---both metallic parts and linkers of varying lengths with differing functional groups---results in a wide range of different types of MOFs, which

vary substantially in geometries and pore size, and thus their physicochemical properties.[1,2] Thanks to their large surface areas, adjustable pore size and controllable pore surface properties, IRMOFs, consisting of zinc oxide clusters (Zn_4O) connected by organic linkers, have been studied extensively for applications such as gas storage and separation. One important example is CO_2 capture, which has received special attention because of concerns over greenhouse gas emissions and global warming issues.[3-7]

ILs have gained overwhelming interest over the last decade or so due to their attractive properties, such as low melting points, non-volatility, non-flammability as well as good thermal and chemical stability.[8,9] It has been shown that ILs have good potential for adsorbing and separating CO_2 from a gas mixture.[10] Nevertheless, high viscosity of ILs poses a significant barrier to the diffusion of adsorbates in ILs. This drawback can be partially addressed by utilizing ILs supported in cavities of porous solids.[11] Compared with neat ILs, supported IL phase reduces the ILs' viscosity and improves the mechanical strength and separation efficiency.[11,12] Recent molecular simulations by Jiang and co-workers[13,14] suggest that ILs supported in IRMOF-1 (in which the linker is 1,4-benzenedicarboxylate) might be useful for CO_2 capture. Their study also indicates that the increase in the IL concentration in the IL/IRMOF-1 composites may improve CO_2 selectivity, i.e., enhancement of CO_2 adsorption from a CO_2/N_2 mixture.

Another interesting application of ILs in connection with MOFs is ionothermal synthesis advanced by Morris and co-workers.[15,16] With ILs used as a solvent and a template/structure-directing agent in materials synthesis, ionothermal synthesis offers a versatile and promising approach to prepare many different types of solids, including novel MOFs.[17-23] As such, it has received increasing attention as a robust pathway towards

synthesizing new solids and hence advancing functional materials.[24-27] Because of ILs' roles both as the spectator solvent and as the active reactants, structural building blocks, and charge-compensating groups, they can influence and even govern the final crystal structure and morphologies of solids. In this context, the molecular-level insight on IL-solid interactions is important to understand structure and stability of the materials, such as MOF in ILs.

Computer simulations are a useful method to probe and analyze IL-MOF interactions. MOFs are often treated as non-dissociable frameworks in simulation studies although in reality, they are flexible and dissociable. One important consequence of flexible and dissociable frameworks is capturing of molecules that are larger than MOF pore dimension, e.g., toluene inside nickel-pyridine MOF.[28] Another is structural and chemical instability of IRMOFs. For instance, IRMOFs are vulnerable to humid air[29-33] and quick hydrolysis of their frameworks leads to a dramatic drop in surface area.[33,34] Since these features cannot be accounted for with a non-dissociable model,[13,14] it is both worthwhile and desirable to re-examine IRMOFs in the presence of ILs using a flexible and dissociable description and compare with the predictions of the non-dissociable model. There are a few flexible force field descriptions[35-44] that correctly capture a range of structural properties of MOFs, such as thermal expansion, elastic moduli, and vibrational spectra as well as guest dynamics. In this chapter, we examine the structural stability of IRMOF-1 and IRMOF-10 in the presence of ILs via MD using the force-field description proposed by Greathouse and Allendorf.[35] To assess the results obtained with classical MD, a further analysis via DFT and *ab initio* molecular dynamics simulations is performed. Our study shows that in the presence of ILs, IRMOF structure is unstable or, at least, highly

prone to undergo major changes. This finding indicates that IRMOFs may not provide a viable system to support ILs inside their pores.

The outline of this chapter is as follows: The models and methods employed in simulations and DFT calculations are first described briefly. The results for MOF structure in the presence of ILs are discussed next. Concluding remarks are offered at the end.

1.3 Simulation Method

1.3.1 MD simulations. The unit cell of IRMOF-1 was adopted from its crystal structure with the lattice spacing 25.67 Å.[45] A 2 × 2 × 2 supercell of this framework with a total of 8 unit cells was constructed and an IL was placed inside the supercell (Figure 1.1). In addition to imidazolium-based ILs that allow a direct comparison with earlier work with a non-dissociable MOF description,[13,14] pyridinium-based ILs are considered. We varied the number of guest ion pairs in the supercell to examine the effect of IL concentration on the MOF stability (see Table 1.1). For each system, energy optimization, *NVT* annealing from 800 K to 300 K, and equilibration were first conducted in the presence of rigid MOF structure. This was followed by energy minimization on the entire system (MOF + IL) using a dissociable MOF description. MD simulations were carried out for 10 ns on the resulting structure using *NPT* ensemble at 1 *atm* and 300 K. All simulations were performed using the NAMD package.[46] The Langevin dynamics and Nose-Hoover Langevin piston were used to keep the temperature and pressure constant, respectively.[47] No symmetry constraints were applied, so that lattice parameters were allowed to change in each direction independently. The particle mesh Ewald (PME) algorithm was used to

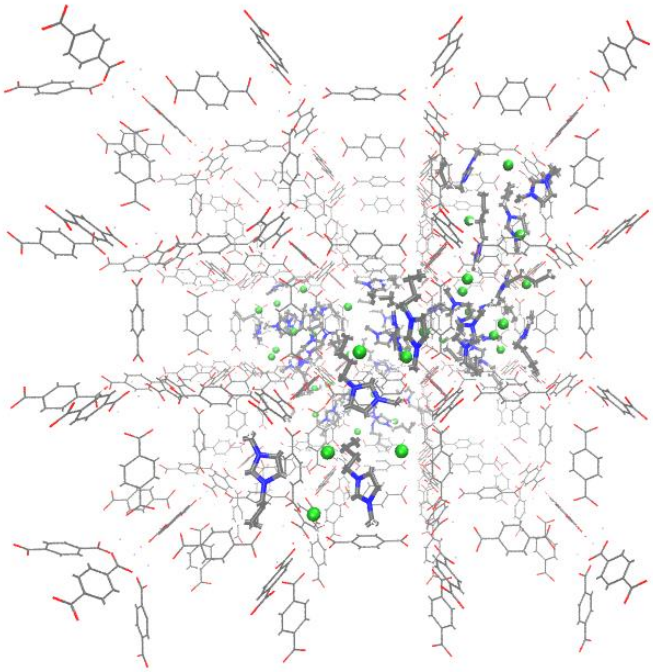

Figure 1.1. Snapshot of the IRMOF-1 supercell with 35 ion pairs of BMI^+Br^-. A rigid MOF framework was employed in the simulation. Bromine, oxygen, nitrogen, carbon, and hydrogen atoms are shown in green, red, blue, dark gray, and light gray, respectively.

Table 1.1. IRMOF-1 stability in the presence of guest ion pairs in the simulation supercell.[a]

Number of ion pairs	$BMI^+PF_6^-$	BMI^+Br^-	$BMI^+Tf_2N^-$	BMI^+DCA^-	$BuPy^+Tf_2N^-$	$BMI^+PF_6^-$*
7	S	S	S	S	S	S
9	S	S	S	NS	S	S
11	S	S	S	NS	S	S
13	S	S	NS	NS	S	S
15	NS	NS	NS	NS	NS	S
17	NS	NS	NS	NS	NS	S
35	NS	NS	NS	NS	NS	S
37	NS	NS	NS	NS	NS	NS

[a] S (NS) denotes that the MOF/IL system is stable (unstable). Calculated lattice parameter of pure IRMOF-1 is 25.61 ± 0.03 Å.
*Results obtained with the force field parameterization of ref 66.

calculate the long-range electrostatic interactions.[48] The van der Waals forces were truncated using a cutoff of 12 Å. Short and long range energy terms were calculated every 0.5 fs and 1.0 fs, respectively. The potential model based on OPLS-AA was employed to describe interactions involving ILs.[49-52] We note parenthetically that structure of ILs inside carbon nanotubes was studied previously using the same model description.[53,54] For IRMOF, we employed both the dissociable and non-dissociable force field descriptions of ref 35. The dissociable description,[35] based on the CVFF force field combined with non-bonded parameterization of ZnO, successfully predicts[55] collapse of MOF above a critical water concentration in concert with experiments.[33]

1.3.2 DFT calculations. A zinc oxide cluster (Zn_4O) coordinated by six formate (HCO_2^-) anions was used as a model IRMOF system for DFT calculations (Figure 1.2). Its molecular structure in the absence and presence of IL ions was optimized via DFT using the B3LYP hybrid functional in all-electron 6-31G(d,p) basis set.[56-59] According to a prior study, this method predicts MOF structures reasonably.[37] A vibrational frequency analysis was performed to ensure that optimized structures we obtained are stable states, corresponding to local energy minima. All calculations were carried out with the Gaussian 09 package.[59]

1.3.3 Ab initio molecular dynamics. For efficient computations, we considered a model unit cell consisting of 83 atoms, in which 1,4-benzenedicarboxylate linkers of IRMOF-1 are replaced by 4,4′-biphenyldicarboxylate (Figure 1.3). (For comparison, an IRMOF-1 unit cell contains 424 atoms.[45]) We note that this model system resembles IRMOF-10 but its torsional angle between two biphenyl groups is initially set at 90º (Figure 1.4). This system was simulated via AIMD in the absence and presence of a guest IL ion pair for 3.5 ps and 4.2 ps, respectively, in the *NPT* ensemble at 1 *atm* and 300 K. The Vanderbilt Ultra-

Soft method was used to describe the interaction between the electrons and nuclei.[60,61] The Perdew–Burke–Ernzerhof (PBE) form of the generalized gradient approximation was employed for electron exchange and correlation.[62,63] The Grimme-D2 method was used to incorporate the van der Waals (vdW) interactions into the system with a cutoff of 12 Å.[64] All calculations were carried out with the Quantum Espresso 5.1 package.[65]

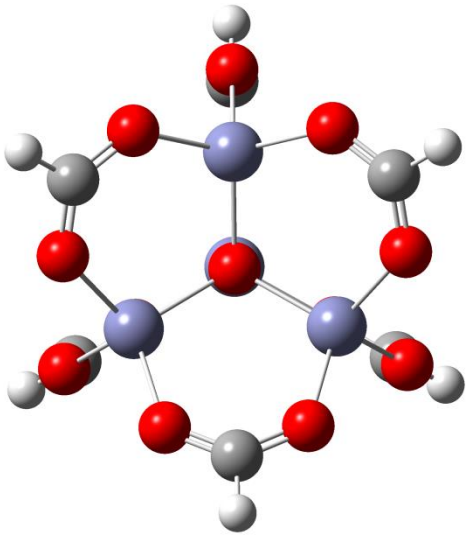

Figure 1.2. Molecular structure of $Zn_4O(HCO_2)_6$. Zinc, oxygen, carbon, and hydrogen atoms are shown in purple, red, dark gray and light gray, respectively.

1.4 Results and discussions

1.4.1 Classical MD simulations. MD results for IRMOF-1 structure in the presence of ILs are compiled in Table 1.1. The most noteworthy aspect there is that IRMOF-1 is not stable. For all ILs we studied, the IRMOF-1 structure was found to collapse completely at IL loadings as low as about 15 ion pairs in the simulation supercell consisting of 8 MOF unit cells. We do not exclude the possibility that some of the stable MOF systems in Table 1.1 could become exclude the possibility that some of the stable MOF systems in Table 1.1 could become unstable if simulations are performed considerably longer than 10 ns. This

finding calls into question the use of rigid or non-dissociable force field parameters for IRMOFs to study their interactions with ILs.

The radial distribution functions (RDFs) of anions around Zn in Figure 1.5 show pronounced peak structures at small *r*. This means that many of the anions are situated close to Zn_4O sites of MOF and interact with its zinc atoms, in agreement with previous results obtained with a rigid MOF description.[13,14] Interestingly, the RDF peaks in the dissociable MOF description are located at considerably smaller separations than those in the rigid model. This attributed to the displacement of Zn atoms from their equilibrium positions in the dissociable model (cf. Figure 1.6). These structural changes allow IL anions to access Zn atom sites better and more easily (because steric hindrance arising from other moieties of

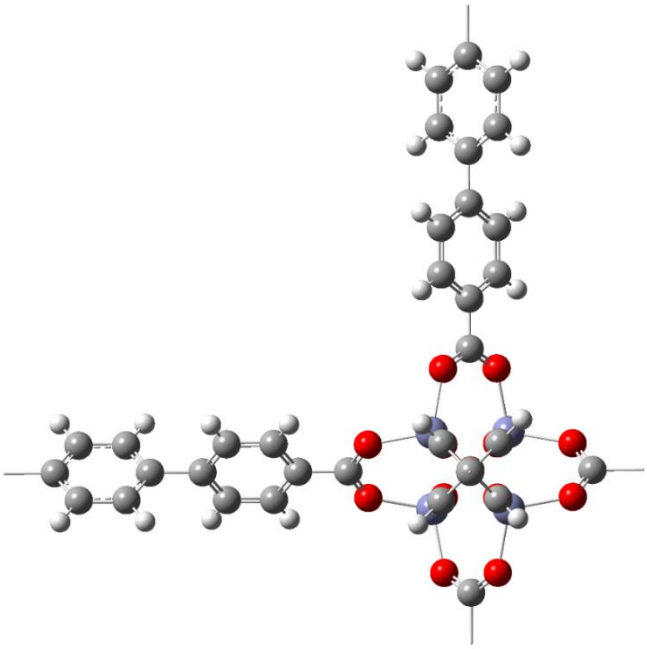

Figure 1.3. IRMOF model used in ab initio MD. 1,4-benzenedicarboxylate linkers of IRMOF-1 are substituted with 4,4′-biphenyldicarboxylate. The color representations are the same as in Figure 1.2.

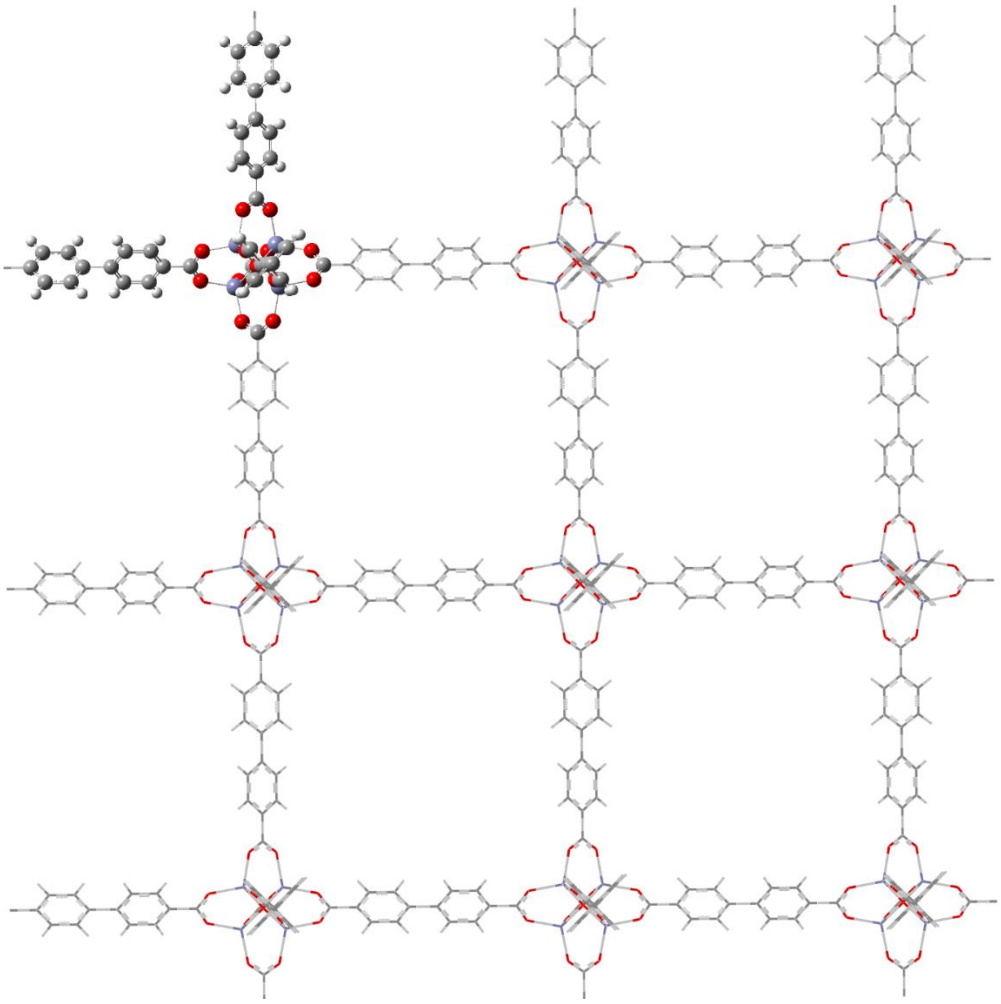

Figure 1.4. Periodic view of the model used in *ab initio* MD.

the MOF is reduced) than in the rigid model description. We also mention that IL ions show an inhomogeneous distribution, clustered near the MOF skeleton in a very non-uniform manner (see Figure 1.1). Some MOF unit cells are occupied by multiple ion pairs, while some other cells are totally unoccupied.

Another interesting result is that the critical IL density for structural instability of IRMOF-1 varies with the IL's anionic species. Specifically, for given cationic species BMI^+, the critical density tends to be lower with anions with an elongated structure. This

trend is ascribed to interactions of elongated anions with multiple Zn_4O sites. To illustrate this point, two frequently occurring configurations of Tf_2N^- ions near Zn_4O sites are exhibited in Figure 1.7. Due to its extended structure, Tf_2N^- can interact with Zn atoms of two different Zn_4O sites simultaneously via its O atoms with a partial negative charge. This strongly suggests that the effectiveness of Tf_2N^- in interacting with and thus disrupting the structure of metal centers is higher than that of smaller spherical anions such as PF_6^- and Br^-. We also notice in Table 1.1 that DCA^- is more effective in dissolving IRMOF-1 than Tf_2N^-. This is expected because the magnitude of the negative partial charge on two terminal nitrogen sites (-0.76e) of DCA^- is substantially higher than that on oxygen sites (-0.53e) of Tf_2N^-, and as a result, electrostatic interactions of the former with Zn atoms are stronger than those of the latter.

Our findings above indicate that interactions of IL anions with MOF play an important role in driving structural instability of IRMOF-1. Nonetheless, distributions of cations (Figure 1.8) suggest that they also contribute to MOF collapse by interacting with, in particular, O atoms of the linkers. This explains why IRMOF-1 is more stable with $BuPy^+Tf_2N^-$ than with $BMI^+Tf_2N^-$. Since the magnitude of atomic partial charges of $BuPy^+$ is generally smaller than that of BMI^+, the cation-linker electrostatic interactions are weaker for the former than for the latter.

In addition to the ILs listed in Table 1.1, we have studied IRMOF-1 stability in the presence of other ionic liquids consisting of tetrafluoroborate, acetate or cyclopentadienyl anions paired with either BMI^+ or $BuPy^+$ cations. With 17 ion pairs of these ILs present inside the simulation supercell, IRMOF-1 was found to be unstable in all cases.

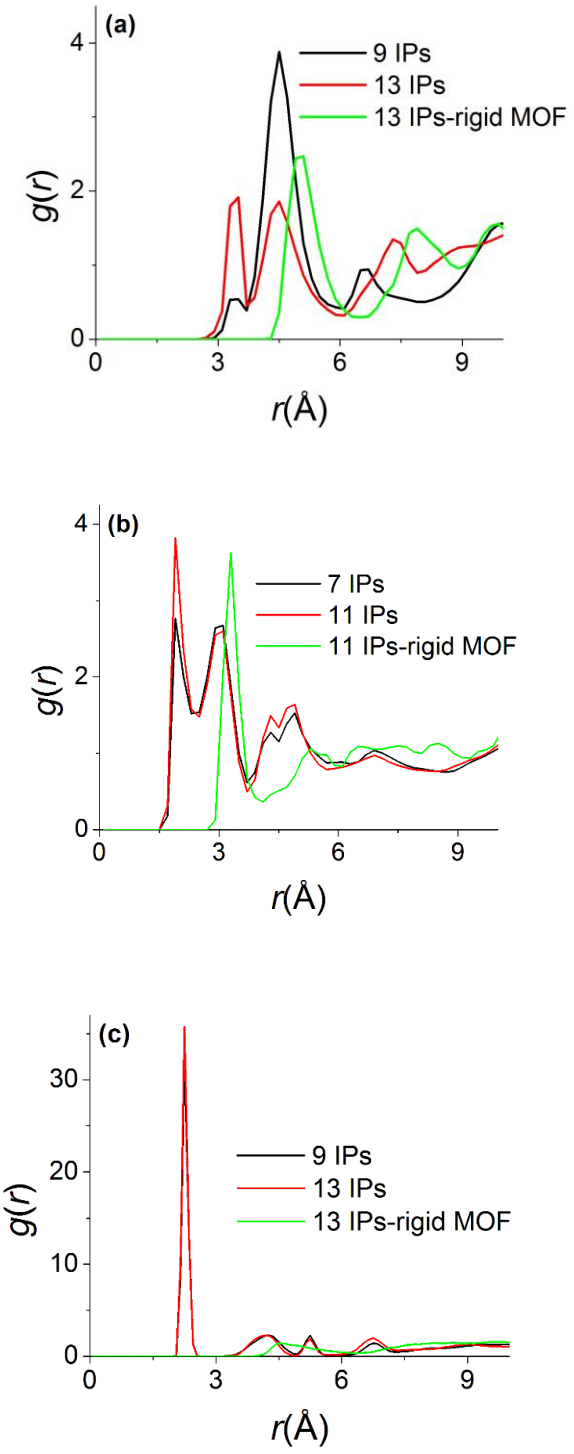

Figure 1.5. Radial distribution functions of anions of BMI^+-based ILs around Zn of IRMOF-1: (a) P of PF_6^-, (b) O of Tf_2N^- and (c) Br^-. For each IL, the stable MOF cases with the largest number of ion pairs (cf. Table 1.1) and four fewer ion pairs are compared with the rigid MOF case.

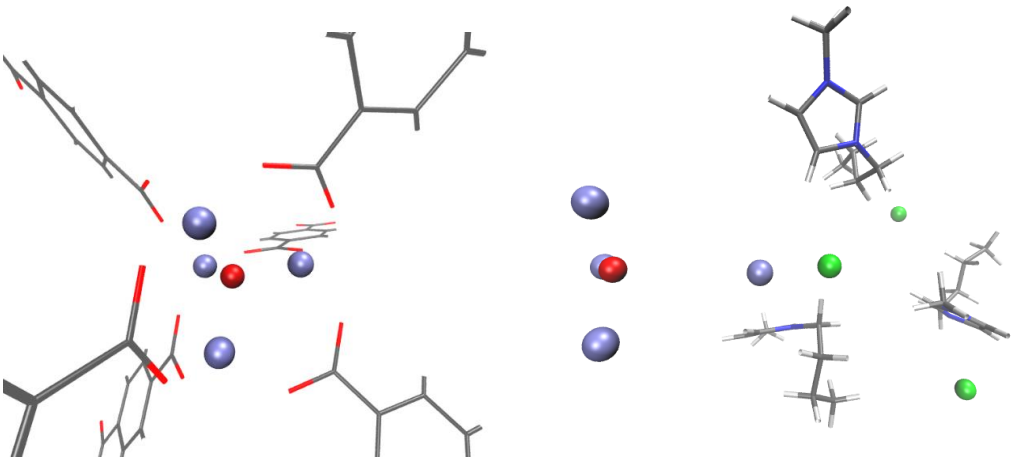

Figure 1.6. Molecular geometry of $Zn_4O(1,4\text{-benzenedicarboxylate})_6$: (a) crystal structure and (b) a snapshot taken from MD with 13 ion pairs of BMI^+Br^- present in the simulation supercell. For clarity, only three ion pairs closest to the Zn_4O site are shown and linkers are not displayed in (b). The interactions of Br^- (green) with Zn (purple) deform the metal site, Zn_4O, from its tetrahedral symmetry (panel (a)) by pulling a Zn atom towards the MOF cavity (panel (b)). Analysis shows that the distance between the displaced Zn and the central O (red) in (b) can reach 4.5 Å (the corresponding distance in the crystal structure in (a) is 1.93–1.95 Å). Three other zinc atoms that are not displaced become nearly co-planar with the central O as shown in (b). Despite its significant structural disruption, MOF was found to be stable in this case according to MD (see Table 1.1).

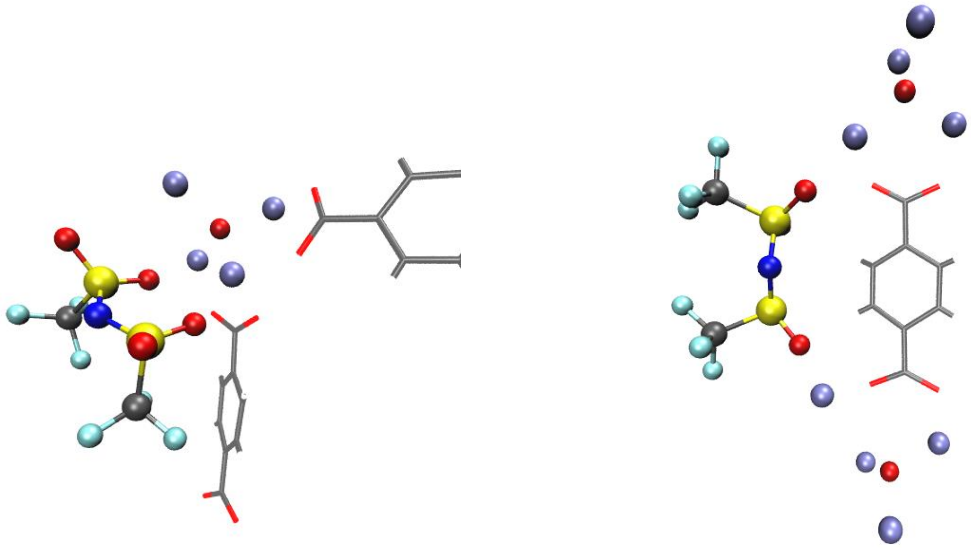

Figure 1.7. Two frequently-occurring configurations of TF_2N^- near Zn_4O groups: a single anion interacts with (a) one and (b) two Zn_4O groups. Color: S (yellow), O (red), C (dark gray), N (blue), F (light green), and Zn (purple).

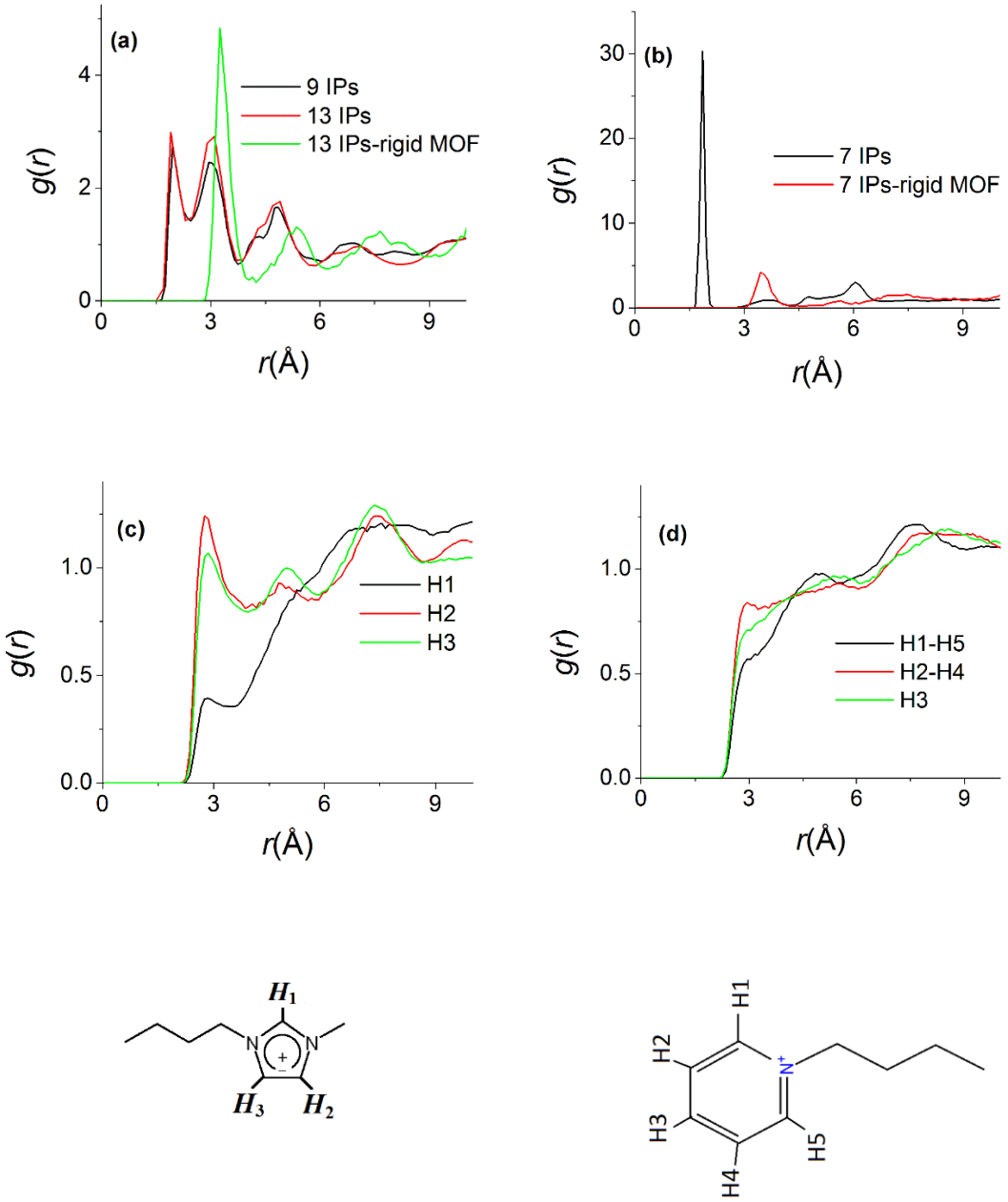

Figure 1.8. MD results for radial distribution functions of (a) O of Tf_2N^- ($BuPy^+Tf_2N^-$), (b) N of DCA^- (BMI^+DCA^-) around Zn of IRMOF-1, (c), and (d) ring hydrogen of BMI^+ ($BMI^+PF_6^-$) and $BuPy^+$ ($BuPy^+Tf_2N^-$) around O of IRMOF-1's linkers using dissociable MOF's model, respectively.

For insight into the dependence of the MOF stability results on IL potential models, we have considered another model for $BMI^+ PF_6^-$, viz., the force field parameterization proposed by Bhargave and Balarsubramanian.[66] Its main difference from the model description of refs 49-51 is the total ionic charge. Specifically, partial charges of the cations and anions are scaled by 0.8, so that their respective total charges are 0.8e and −0.8e in the model description of ref 66. The MD results obtained with these reduced ion charges are summarized in Table 1.1. We notice that the critical density for the collapse of IRMOF-1 structure increases to 37 ion pairs with reduced IL charges from 17 with full charges. This clearly demonstrates the importance of MOF-IL electrostatic interactions in governing MOF structural stability. Nevertheless, IRMOF-1 becomes unstable even in the case of reduced charges *with significantly weakened electrostatic interactions*, suggesting that IRMOF structural instability we have found in the presence of ILs is independent of the details of the IL potential models.

Turning to IRMOF-10,[5] whose 4,4′-biphenyldicarboxylate linkers afford bigger pores than 1,4-benzenedicarboxylate linkers of IRMOF-1, we considered two different loadings of $BMI^+PF_6^-$, 70 and 140 ion pairs, in its (2 × 2 × 2) supercell. We found that in both cases, IRMOF-10 is structurally unstable just like IRMOF-1. This seems to suggest that IRMOFs are generally unstable in the presence of ILs regardless of their pore size.

We briefly pause here for perspective. While MD provides key molecular-level information on structural stability of IRMOF systems in the presence of ILs, several important features, e.g., variations of partial charges of Zn and other moieties of MOF as they deform, are not included in the MOF model[35] used in our study. A similar polarizability effect associated with guest molecules (ILs in our case) is also not accounted

for. According to a prior study, the neglect of electronic polarizability can lead to a substantial underestimation of transport coefficients; e.g., the simulated diffusion coefficient of guest molecules like benzene was found to be an order of magnitude lower than experimental results.[35] Since our model description is classical, chemical reactivity, such as electron and proton transfers, is also not properly accounted for. Another potential difficulty is the combination of OPLS-AA-based parameters (ILs) with CVFF-based parameters (MOFs) invoked in our simulations.[39] While we do not believe any of these assumptions/approximations would have significant impact on our main result, i.e., structural instability of IRMOF in the presence of ILs, we have nonetheless attempted to address them using the DFT and *ab initio* MD methods. We turn to them next.

1.4.2 DFT calculations. DFT calculations were performed for $Zn_4O(HCO_2)_6$ (Figure 1.2) as a model fragment of IRMOF-1 in the absence and presence of 1,3-dimethylimidazolium (DMI^+) cations and Br^-, SCN^-, BF_4^-, and PF_6^- anions. As presented in Table 1.2 and Figure 1.9, calculated structural parameters of the MOF fragment in the absence of ILs are in reasonable agreement with previous theoretical and experimental results.[37, 67, 68]

DFT calculations predict that structure of the $Zn_4O(HCO_2)_6$ fragment does not deform significantly in the presence of a DMI^+ ion whose ring hydrogen atoms interact primarily with the linkers' oxygen atoms. While Zn-O bond lengths do change somewhat compared to an isolated fragment, the tetrahedral symmetry of four O atoms coordinating a Zn atom (Figure 1.2) remains largely intact (Figure 1.10).

When the $Zn_4O(HCO_2)_6$ fragment is exposed to an anion, however, the latter interacts directly with one of Zn atoms of the former and becomes coordinated with that Zn atom. This increases the coordination number of the Zn atom to five (or higher) from

four, resulting in a significant structural change of the Zn site. The optimized structure of the MOF fragment in the presence of one Br^- ion is displayed in Figure 1.11. Br^- forms a coordinate bond with one of Zn atoms with bond length of 2.333 Å. This Zn-Br^- interaction deforms the tetrahedral (T_d) structure of the Zn atom's coordination shell (Figure 1.2) in

Table 1.2. Calculated bond lengths (in Å) compared to previous experimental and theoretical results.*

Method	Zn-O_{cent}	Zn-O_{carb}	O_{carb}-C_{carb}
B3LYP-6-31G(d,p)[37]	1.953	1.948	1.271
X-ray[67]	1.933-1.945	1.937-1.969	1.244-1.267
X-ray[68]	1.936–1.950	1.930–1.950	1.234–1.270
B3LYP-6-31G(d,p), current study	1.962	1.952	1.261

* See Figure 1.9 for atom labels

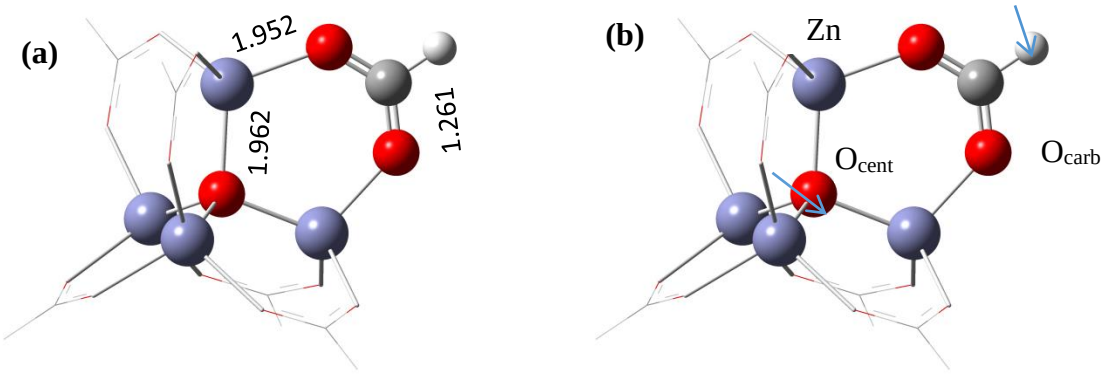

Figure 1.9. Optimized structure of the model $Zn_4O(HCO_2)_6$ fragment: (a) bond distances (in Å) and (b) atom labels (O, C and Zn atoms are colored in red, grey, and purple, respectively).

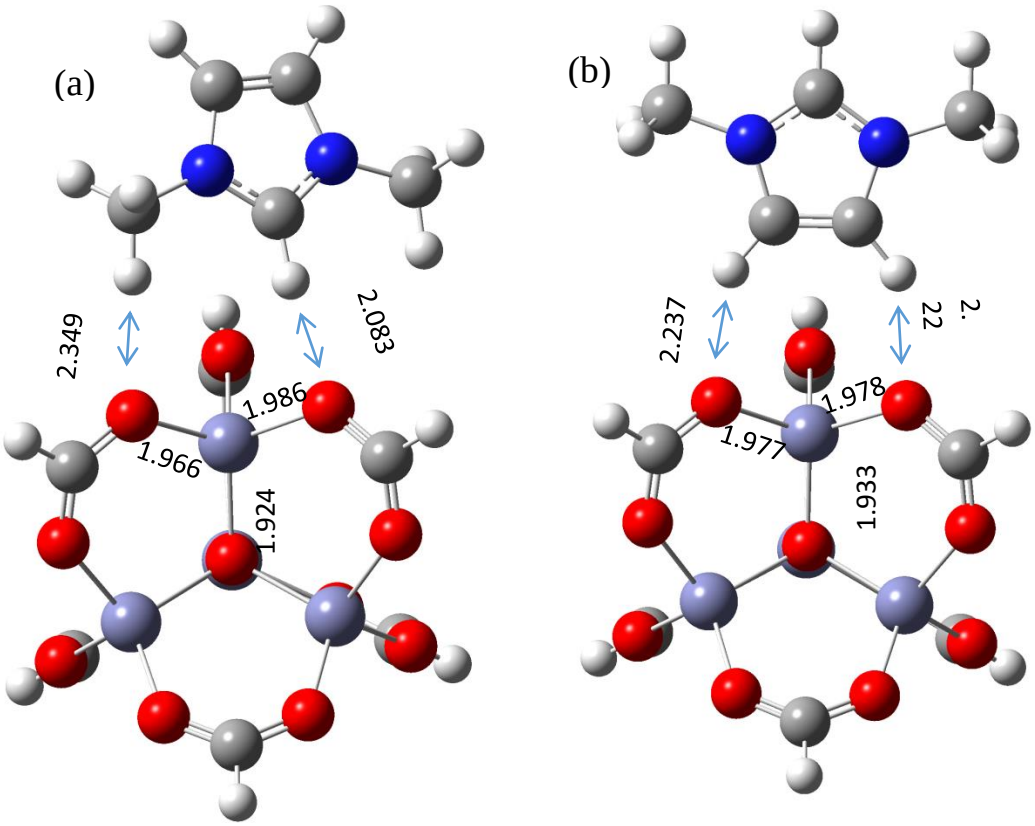

Figure 1.10. Two optimized structures of $Zn_4O(HCO_2)_6$ in the presence of one DMI^+ cation. Distances are measured in units of Å. Configuration (a) is 2.09 kcal/mol lower in energy than configuration (b).

the crystalline phase to almost a trigonal bipyramidal (T_b) structure with Br^- as an equatorial ligand as illustrated in Figure 1.11b. This confirms the MD result above that Zn mainly interacts with IL anions. In the case of BF_4^-, two of its F atoms can interact with the same Zn atom, resulting in the coordination number of six for Zn (Figure 1.12). Depending on electronegativity of the coordinating atom of the anions, the new ligand, i.e., anion, would prefer equatorial or axial positions of T_b structure (Figure 1.13). For instance, in the case of SCN^-, the highly electronegative nitrogen atom acts as an axial ligand.

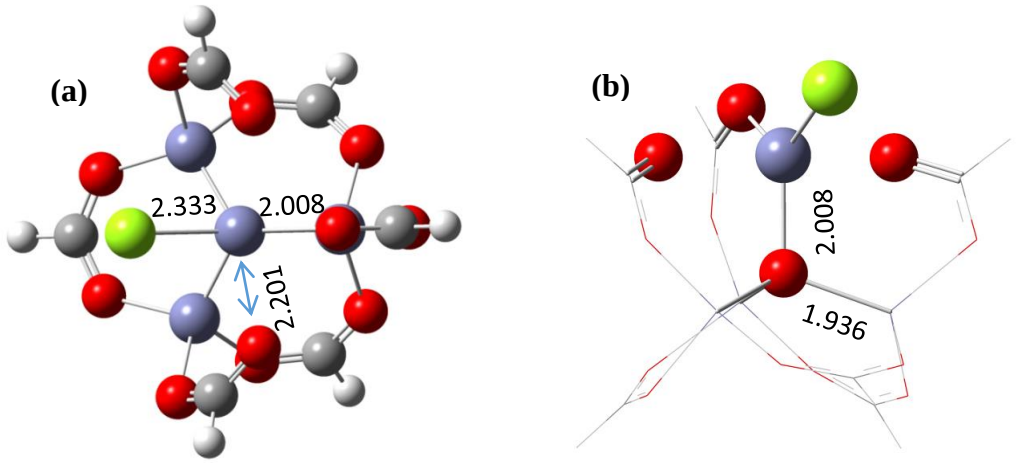

Figure 1.11. Optimized molecular structure of $Zn_4O(HCO_2)_6$ in the presence of one bromide anion. Two different views of the structure are shown in (a) and (b). In (b), Br^- interacting with Zn and its coordinated O atoms form a trigonal bipyramidal structure with the base consisting of two O atoms and Br^-. The Zn atom is nearly co-planar with the base. See Figures 1.2 and 1.6 for color representations of different atom types. Distances are measured in units of Å.

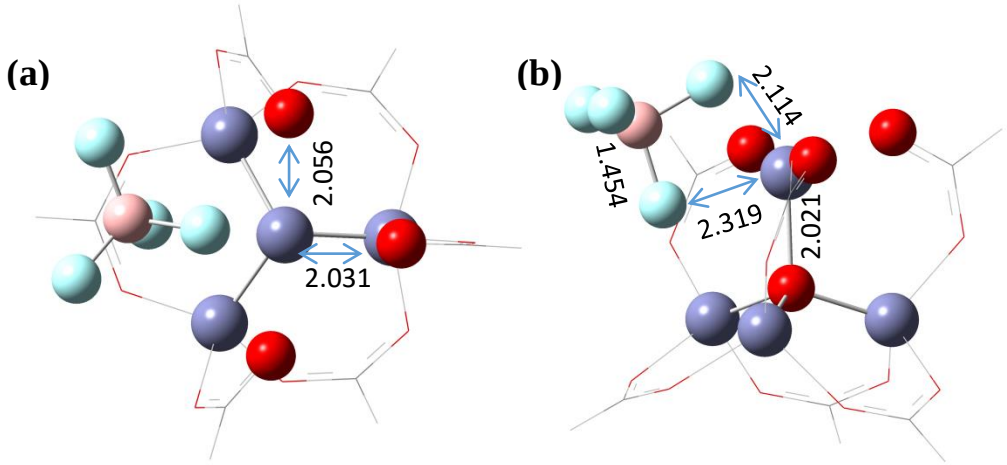

Figure 1.12. Optimized structure of $Zn_4O(HCO_2)_6$ in the presence of one BF_4^- anion. Distances are measured in units of Å. In (a), bond lengths between Zn and coordinating O atoms of formate linkers are shown. In (b), distances between Zn and coordinating F atoms as well as that between Zn and central oxygen O_{cent} are presented. The bond length between the anion's B and two F atoms that do not interact with Zn is 1.369 Å.

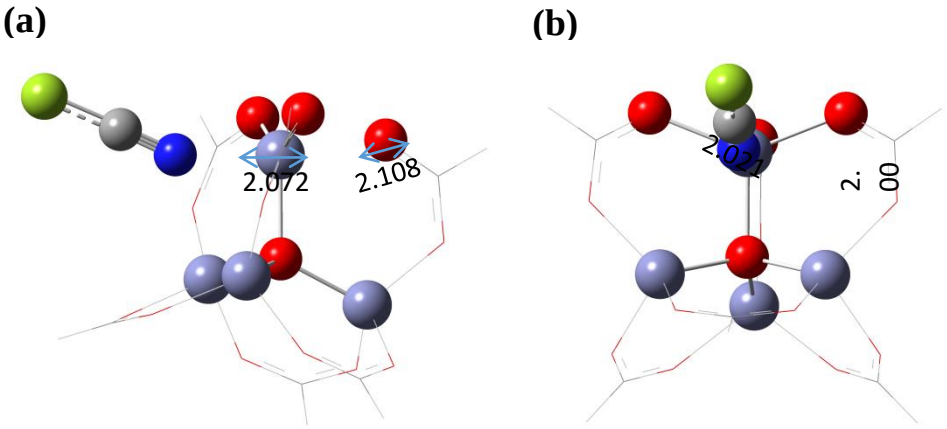

Figure 1.13. Optimized structure of $Zn_4O(HCO_2)_6$ interacting with one SCN^- anion. In (a) and (b), axial and equatorial bond lengths are shown, respectively. Units for distance: Å.

While addition of a DMI^+ cation to $Zn_4O(HCO_2)_6$-Br^- complex in Figure 1.11 does not introduce significant structural changes, addition of a second Br^-, which forms a coordinate bond with another Zn atom, does. Upon sequential introduction of first Br^-, first DMI^+, second Br^- and second DMI^+ ions to the $Zn_4O(HCO_2)_6$ fragment, the minimal RMSD (root mean square deviation) from its gas-phase structure generally increases as 0.597, 0.567, 0.830, and 0.839 Å according to DFT. This lends support to our MD results that interactions of anions with zinc oxide clusters (Zn_4O) are mainly responsible for deformation of IRMOF structure and that IRMOF is not stable in the presence of ILs.

***1.4.3 Ab initio molecular dynamics*.** Though DFT calculations provide atomistic insights into molecular geometry of IRMOF's metallic part in the presence of ILs, the influence of system dynamics and of MOF's structural connectivity on its deformation is not included. To understand these effects, we simulated the model IRMOF system in Figure 1.3 with the *ab initio* method in the absence and presence of a guest ion pair DMI^+Br^-.

The AIMD results for temporal variations of the unit-cell volume of the IRMOF system are shown in Figure 1.14. In the case of pure MOF with no guest ion pair, its volume fluctuates but does not appear to shift with time. The average volume of the model IRMOF remains unchanged at around 5105 $Å^3$ with lattice parameter a = 17.2 Å and unit-cell parameters $\alpha = \beta = \gamma \sim 90^o$. We parenthetically note that since the unit-cell of the actual IRMOF-10 is eight times larger than that of our model, our simulations yield 40840 $Å^3$ and 34.4 Å for the unit-cell volume and lattice parameter for IRMOF-10, respectively. These values compare well with the experimental results, 40285.52 $Å^3$ and 34.28 Å.[5]

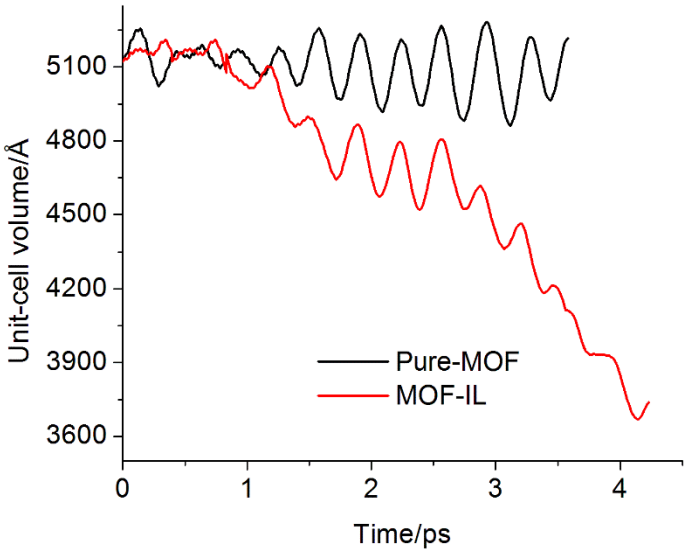

Figure 1.14. AIMD results for temporal changes of the unit-cell volume of the model IRMOF system (Figure 1.2) in the absence and presence of a guest DMI^+Br^- ion pair.

In the presence of an ion pair DMI^+Br^-, the model IRMOF system shows an oscillatory but steady decrease in volume. During the 4.2 ps simulation period, the volume decreases by nearly 30% from ~5100 $Å^3$ to ~3600 $Å^3$! Final values of its unit-cell

parameters at the end of the simulation are $\alpha \sim 111^{o}$, $\beta \sim 91^{o}$ and $\gamma \sim 83^{o}$, which differ markedly from their initial values $\alpha = \beta = \gamma = 90^{o}$. Thus IRMOF structure loses its original symmetry and rapidly turns into a rhombus shape in the presence of a guest ion pair. This is in striking contrast with pure IRMOF, which retains its crystal structure throughout the simulation. (Final configurations of AIMD simulations in the absence and presence of the ion pair are displayed, respectively, in Figures 1.15 and 1.16) Though our AIMD simulation was performed only for a short period of time, it strongly indicates the onset of collapse or major re-structuring of MOF framework in the presence of ILs, consonant with the classical MD results presented above.

For insights into the mechanism of IL-induced disruption on MOF structure, we monitored positions of the $DMI^{+}Br^{-}$ ion pair with respect to MOF. We found that anion Br^{-} gradually moves from its initial position (> 4 Å from Zn atoms) towards the metallic part of MOF to form a bond with one of the Zn atoms. The formation of this bond induces the elongation of the bonds between Zn and three O atoms of the linkers and deforms the metallic center from its tetrahedral shape. This finding is in line with the DFT (Figure 1.11) and classical MD results discussed above. It also indicates that despite their limitations imposed by various approximations, our classical MD results on MOF structural stability are robust.

1.5 Conclusions

In this article, we have investigated structural stability of IRMOF-1 and IRMOF-10 in the presence of ILs via classical and *ab initio* molecular dynamics simulations as well as DFT calculations. It was found that the original IRMOF structure is not stable in the

presence of ILs. Both simulation and DFT results suggest that interactions between IL anions and Zn atoms of MOF play a central role in engendering structural instability of IRMOF. Therefore, elongated anions, such as Tf_2N^- and DCA^-, which can interact with multiple Zn atoms, are very effective in destabilizing MOF structure, compared to spherical anions, e.g., Br^- and PF_6^-. Our analysis clearly indicates that IRMOF does not offer a good support system for ILs. It also exposes the limitations of non-dissociable force field models in describing MOF structure and dynamics in the presence of guest molecules/ions that interact strongly with MOF via Coulomb forces.

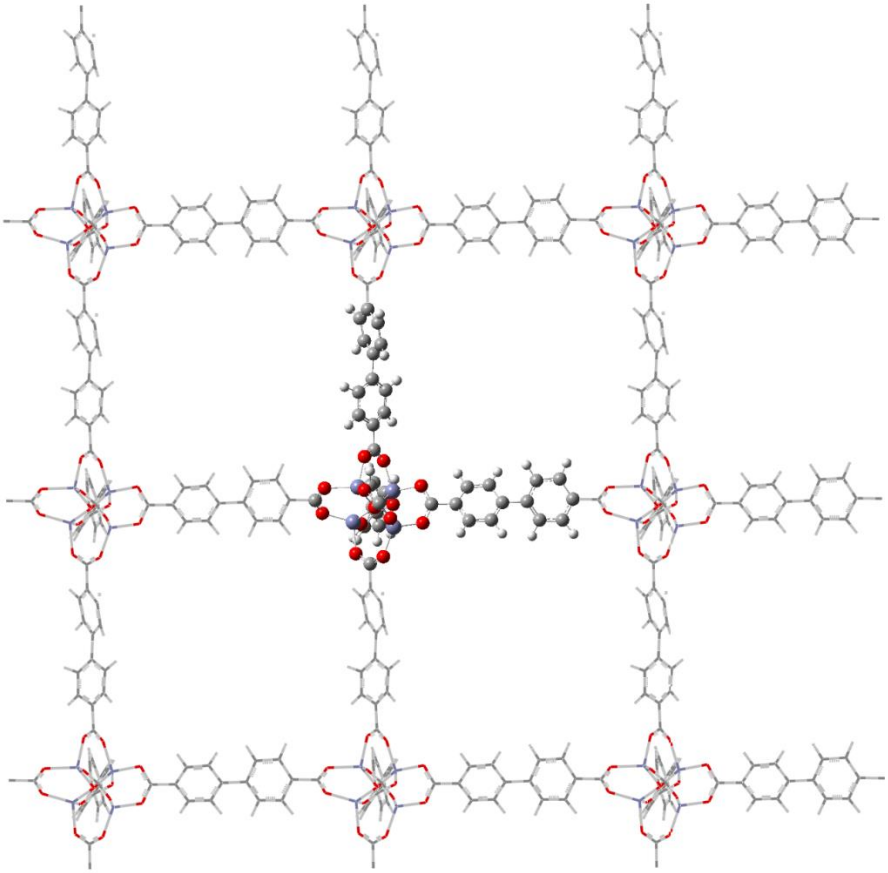

Figure 1.15. Final snapshot of the model used for *ab initio* MD in the absence of BMI^+Br^- .

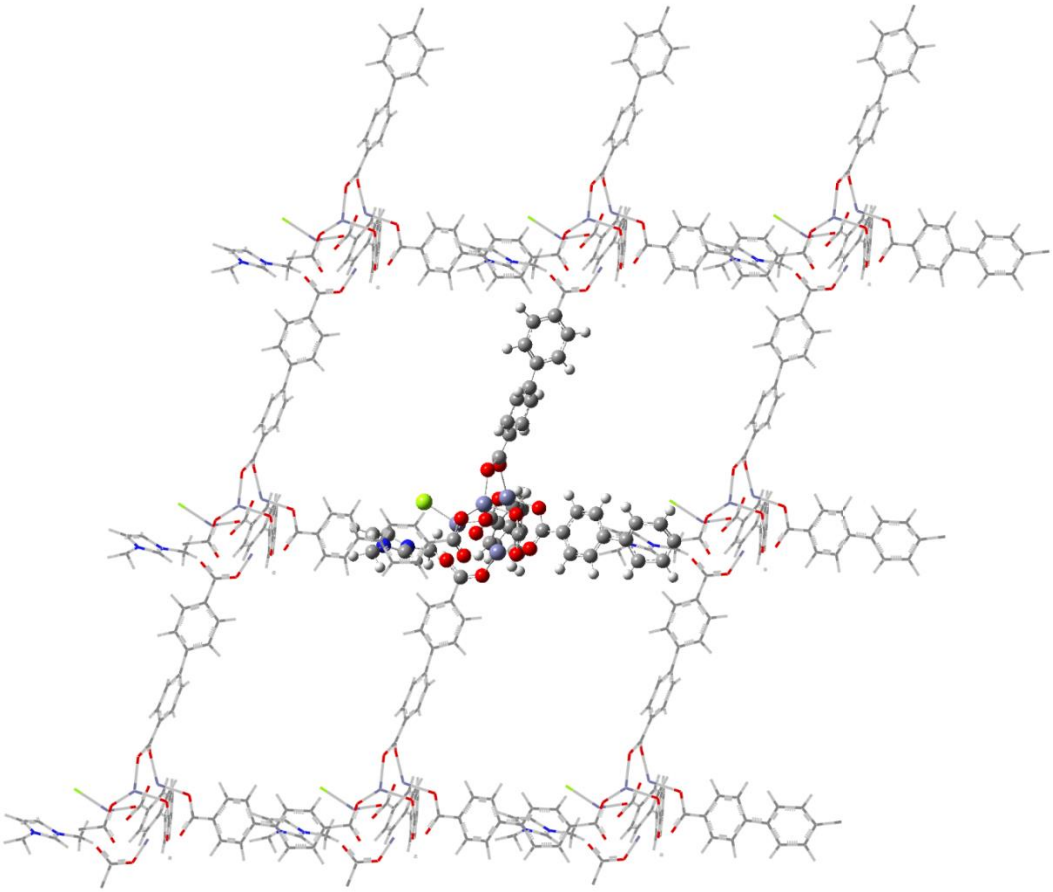

Figure 1.16. Final snapshot of the model used for *ab initio* MD in the presence of one $BMI^{+}Br^{-}$ ion pair.

1.6 Acknowledgments

This work was supported in part by NSF Grant No. CHE-1223988.

1.7 References

1) S. L. James, *Chem. Soc. Rev.*, 2003, **32**, 276- 288.
2) S. Kitagawa, R. Kitaura and S. Noro, *Angew. Chem., Int. Ed.*, 2004, **43**, 2334-2375.
3) J. L. C. Rowsell and O. M. Yaghi, *Microporous Mesoporous Mater.*, 2004, **73**, 3-14.

4) J.L.C. Rowsell and O.M. Yaghi, *Angew. Chem. Int. Ed.*, 2005, **44**, 4670- 4679.
5) M. Eddaoudi, J. Kim, N. Rosi, D. Vodak, J. Wachter, M. O'Keeffe and O. M. Yaghi, *Science*, 2002, **295**, 469- 472.
6) J. M. Hicks, C. Desgranges and J. Delhommelle, *J. Phys. Chem. C*, 2012, **116**, 22938-22946.
7) O. M. Yaghi, M. O'Keeffe, N. W. Ockwig, H. K. Chae, M. Eddaoudi and J. Kim, *Nature* 2003, **423**, 705- 714.
8) S. D. Zhu, Y. X. Wu, Q. M. Chen, Z. N. Yu, C. W. Wang, S. W. Jin, Y. G. Ding and G. Wu, *Green Chem.*, 2006, **8**, 325- 327.
9) N. V. Plechkova and K. R. Seddon, *Chem. Soc. Rev.*, 2008, **37**, 123- 150.
10) M. J. Muldoon, S. N. V. K. Aki, J. L. Anderson, J. K. Dixon and J. F. Brennecke, *J. Phys. Chem. B*, 2007, **111**, 9001- 9009.
11) L. J. Lozano, C. Godinez, A. P. de los Rios, F. J. Hernandez-Fernandez, S. Sanchez-Segado and F. J. Alguacil, *J. Membr. Sci.*, 2011, **376**, 1-14.
12) R. D. Noble and D. L. Gin, *J. Membr. Sci.*, 2011, **369**, 1-4.
13) Y. Chen, Z. Hu, K. M. Gupta and J. Jiang, *J. Phys. Chem. C*, 2011, **115**, 21736-21742.
14) K. M. Gupta, Y. Chen, Z. Hu and J. Jiang, *Phys. Chem. Chem. Phys.*, 2012, **14**, 5785- 5794.
15) E. R. Parnham and R. E. Morris, *Acc. Chem. Res.*, 2007, **40**, 1005–1013.
16) E. R. Cooper, C. D. Andrews, P. S. Wheatley, P. B. Webb, P. Wormald and R. E. Morris, Nature, 2004, **430**, 1012–1016.
17) K. Jin, X. Huang, L. Pan, J. Li, A. Appel and S. Wherland, *Chem. Commun.*, 2002, **23**, 2872–2873.
18) Z. J. Lin, D.S. Wragg, J. E. Warren and R. E. Morris, *J. Am. Chem. Soc.*, 2007, **129**, 10334-10335.
19) K. Pierre, A. Markus and T. Arne, *Angew. Chem. Int. Ed.*, 2008, **47**, 3450- 3453.
20) H. S. Liu, Y. Q. Lan and S. L. Li, *Cryst. Growth Des*., 2010, **10**, 5221-5226.
21) M. Wang, L. Long, R. Huang and L. Zheng, *Chem. Commun.*, 2011, **47**, 9834-9836.
22) L. Peng, J. L. Zhang, J. S. Li, B. X. Han, Z. M. Xue and G. Y. Yang, *Chem. Commun.*, 2012, **48**, 8688- 8690.
23) L. Xu, Y. Kwon, B.D. Castro and L. Cunha-Silva, *Cryst. Growth Des.*, 2013, **13**, 1260- 1266.
24) W. M. Reichert, J. D. Holbrey, K. B. Vigour, T. D. Morgan, G. A. Broker and R. D. Rogers, *Chem. Commun.*, 2006, **46**, 4767–4779.
25) J. Zhang, S. M. Chen and X. H. Bu, *Angew. Chem., Int. Ed*., 2008, **47**, 5434–5437.
26) L. Liu, Y. Li, H. B. Wei, M. Dong, J. G. Wang, A. M. Z. Slawin, J. P. Li, J. X. Dong and R. E. Morris, *Angew. Chem., Int. Ed.*, 2009, **48**, 2206–2209.
27) Z. Ma, J. H. Yu and S. Dai, *Adv. Mater.*, 2010, **22**, 261–285.
28) E. J. Cussen, J. B. Claridge, M. J. Rosseinsky and C. J. Kepert, *J. Am. Chem. Soc.* 2002, **124**, 9574-9581.
29) J. M. Taylor, K. W. Dawson and G. K. H. Shimizu, *J. Am. Chem. Soc.*, 2013, **135**, 1193–1196.

30) J. Yang, A. Grzech, F. M. Mulder and T. J. Dingemans, *Chem. Commun.*, 2011, **47**, 5244-5246.
31) N. C. Burtch, H. Jasuja and K. S. Walton, *Chem. Rev.*, 2014, **114**, 10575-10612.
32) S. S. Kaye, A. Daily, O. M. Yaghi and J. R. Long, *J. Am. Chem. Soc.*, 2007, **129**, 14176- 14177.
33) L. Huang, H. Wang, J. Chen, Z. Wang, J. Sun, D. Zhao and Y. Yan, *Microporous Mesoporous Mater.*, 2003, **58**, 105- 114.
34) S. S. Han, S. H. Choi and A. C. T. Van Duin, *Chem. Commun.*, 2010, **46**, 5713-5715.
35) J. A. Greathouse and M. D. Allendorf, *J. Phys. Chem. C*, 2008, **112**, 5795- 5802.
36) S. Amirjalayer, M. Tafipolsky and R. Schmid, *Angew. Chem., Int. Ed.*, 2007, **46**, 463- 466.
37) M. Tafipolsky, S. Amirjalayer and R. Schmid, *J. Comput. Chem.*, 2007, **28**, 1169-1176.
38) B. L. Huang, A. J. H. McGaughey and M. Kaviany, *Int. J. Heat and Mass Transfer*, 2007, **50**, 393-404.
39) D. Dubbeldam, K. S. Walton, D. E. Ellis and R. Q. Snurr, *Angew. Chem. Int. Ed.*, 2007, **46**, 4496–4499.
40) D. Farrusseng, C. Daniel, C. Gaudillère, U. Ravon, Y. Schuurman, C. Mirodatos, D. Dubbeldam, H. Frost and R. Q. Snurr, *Langmuir*, 2009, **25**, 7383–7388.
41) D. Raymand, A. C. T. Van Duin, D. Spångberg, W. A. Goddard III and K. Hermansson, *Surf. Sci.*, 2010, **604**, 741-876.
42) M. Wehring, J. Gascon, D. Dubbeldam, F. Kapteijn, R. Q. Snurr and F. Stallmach, *J. Phys. Chem. C*, 2010, **114**, 10527–10534.
43) D. C. Ford, D. Dubbeldam, R. Q. Snurr, V. Künzel, M. Wehring, F. Stallmach, J. Kärger and U. Müller, *J. Phys. Chem. Lett.*, 2012, **3**, 930–933.
44) S. Bureekaew, S. Amirjalayer, M. Tafipolsky, C. Spickermann, T. K. Roy and R. Schmid, *Physica Status Solidi (B) Basic Research*, 2013, **250**, 1128-1141.
45) H. Li, M. Eddaoudi, M. O'Keeffe and O. M. Yaghi, *Nature*, 1999, **402**, 276 -279.
46) J. C. Phillips, R. Braun, W. Wang, J. Gumbart, E. Tajkhorshid, E. Villa, C. Chipot, R. D. Skeel, L. Kale and K. Schulten, *J. Comput. Chem*., 2005, **26**, 1781–1802.
47) S. E. Feller, Y. H. Zhang, R. W. Pastor and B. R. Brooks, *J. Chem. Phys.*, 1995, **103**, 4613-4621.
48) T. Darden, D. York and L. Pedersen, L. *J. Chem. Phys.*, 1993, **98**, 10089-10092.
49) J. N. Canongia Lopes, J. Deschamps and A. A. H. Pádua, *J. Chem. Phys. B*, 2004, **108**, 2038-2047.
50) J. N. Canongia Lopes, J. Deschamps and A. A. H. Pádua, *J. Chem. Phys. B*, 2004, **108**, 11250.
51) J. N. Canongia Lopes and A. A. H. Pádua, *J. Phys. Chem. B*, 2004, **108**, 16893-16898.
52) J. N. Canongia Lopes and A. A. H. Pádua, *J. Phys. Chem. B*, 2006, **110**, 19586-19592.
53) Y. Shim and H. J. Kim, *ACS Nano*, 2009, **3**, 1683–1702.
54) Y. Shim and H. J. Kim, *ACS Nano*, 2010, **4**, 2345–2355.

55) J. A. Greathouse and M. D. Allendorf, *J. Am. Chem. Soc.*, 2006, **128**, 10678-10679.
56) A. D. Becke, *Phys. Rev. A*, 1988, **38**, 3098- 3100.
57) A. D. Becke, *J. Chem. Phys.*, 1993, **98**, 5648- 5652.
58) C. Lee, W. Yang and R. G. Parr, *Phys. Rev. B.*, 1988, **37**, 785-789.
59) M. J. Frisch, G. W. Trucks, H. B. Schlegel, G. E. Scuseria, M. A. Robb, J. R. Cheeseman, G. Scalmani, V. Barone, B. Mennucci, G. A. Petersson, H. Nakatsuji, M. Caricato, X. Li, H. P. Hratchian, A. F. Izmaylov, J. Bloino, G. Zheng, J. L. Sonnenberg, M. Hada, M. Ehara, K. Toyota, R. Fukuda, J. Hasegawa, M. Ishida, T. Nakajima, Y. Honda, O. Kitao, H. Nakai, T. Vreven, J. A. Montgomery, Jr., J. E. Peralta, F. Ogliaro, M. Bearpark, J. J. Heyd, E. Brothers, K. N. Kudin, V. N. Staroverov, R. Kobayashi, J. Normand, K. Raghavachari, A. Rendell, J. C. Burant, S. S. Iyengar, J. Tomasi, M. Cossi, N. Rega, J. M. Millam, M. Klene, J. E. Knox, J. B. Cross, V. Bakken, C. Adamo, J. Jaramillo, R. Gomperts, R. E. Stratmann, O. Yazyev, A. J. Austin, R. Cammi, C. Pomelli, J. W. Ochterski, R. L. Martin, K. Morokuma, V. G. Zakrzewski, G. A. Voth, P. Salvador, J. J. Dannenberg, S. Dapprich, A. D. Daniels, Ö. Farkas, J. B. Foresman, J. V. Ortiz, J. Cioslowski, and D. J. Fox, Gaussian, Inc., Wallingford CT, 2009.
60) D. Vanderbilt, *Phys. Rev. B*, 1990, **41**, 7892-7895.
61) G. Kresse and J. Hafner, *J. Phys.: Condens. Matter*, 1994, **6**, 8245.
62) J. P. Perdew, K. Burke and M. Ernzerhof, *Phys. Rev. Lett.*, 1996, **77**, 3865- 3868.
63) J. P. Perdew, K. Burke and M. Ernzerhof, *Phys. Rev. Lett.*, 1997, **78**, 1396-1396.
64) S. J. Grimme, *Comput. Chem.*, 2006, **27**, 1787-1799.
65) P. Giannozzi, S. Baroni, N. Bonini, M. Calandra, R. Car, C. Cavazzoni, D. Ceresoli, G. L. Chiarotti, M. Cococcioni, I. Dabo, A. Dal Corso, S. Fabris, G. Fratesi, S. de Gironcoli, R. Gebauer, U. Gerstmann, C. Gougoussis, A. Kokalj, M. Lazzeri, L. Martin-Samos, N. Marzari, F. Mauri, R. Mazzarello, S. Paolini, A. Pasquarello, L. Paulatto, C. Sbraccia, S. Scandolo, G. Sclauzero, A. P. Seitsonen, A. Smogunov, P. Umari and R. M. Wentzcovitch, *J. Phys.: Condens. Matter*, 2009, **21**, 395502 –395521.
66) B. L. Bhargava and S. Balasubramanian, *J. Chem. Phys.*, 2007, **127**, 114510.
67) W. Clegg, D. R. Harbron, C. D. Homan, P. A. Hunt, I. R. Little and B. P. Straughan, *Inorg. Chim. Acta.*, 1991, **186**, 51-60.
68) M. C. Yin, C. W. Wang, C. C. Al, L. J. Yuan and J. T. Sun, *Wuhan. Univ. J. Nat. Sci.* 2004, **9**, 939-942.

Chapter 2: *Interactions of a lithium bis(trifluoromethane sulfonyl)imide ($Li^+Tf_2N^-$) ion pair with oligoether*

2.1 Abstract

Interactions of a lithium bis(trifluoromethane sulfonyl)imide ($Li^+Tf_2N^-$) ion pair with oligoethers are investigated via the density functional theory (DFT). As a model for polymer electrolytes polyethyleneoxide (PEO) and perfluoropolyether (PFPE), $CR_3(OCR_2CR_2)_{n=1-5}OCR_3$ (R = H or F) are considered. Topographical analysis of the molecular electrostatic potential (MESP) is performed to determine preferential binding sites of Li^+. Our study shows that the MESP value near oxygen sites of the polymer backbone is more negative for PEO than for PFPE. This result indicates that substitution of hydrogen by fluorine in polyethers leads to reduction in Li^+–polymer interactions, in concert with the experimental ionic conductivity results. S-O stretching vibrations of Tf_2N^- are calculated for the lithium salt in the presence and absence of the electrolytes. The blue and red shifts predicted for S-O stretching are further explained by natural bond orbital analysis and molecular electron density topography. The S-O stretching vibrations can be used as a useful tool to understand the ion pair interactions and thus ion transport phenomena in the polymer electrolytes.

Keywords: lithium bis(trifluoromethane sulfonyl)imide, lithium-ion batteries, nonflammable electrolytes, PEO, PFPE, ionic conductivity, DFT

2.2 Introduction

The stringent demand for portable power sources characterized by high energy and/or high power densities, good cyclability, reliability, and safety continues to generate a great deal of research interest from both academia and industry world-wide.[1-3] State-of-the-art

lithium-ion (Li-ion) batteries are not only in widespread use in consumer electronics but also playing a key role in the development of technology in aerospace, medicine, and other elite markets.[4-8] Unfortunately, the thermal instability of the alkyl carbonates which are the most common electrolytes for the Li-ion batteries tends to restrict the utility of such batteries at elevated temperatures.[9-12] The high volatility and flammability of the conventional organic electrolytes pose a serious safety issue for their use in the consumer and transportation markets. To address such issues, a significant effort has been focused on the synthesis and utilization of nonflammable electrolytes, such as ionic liquids, gel-polymer matrices, and small molecule additives.[13-19]

Polymer electrolytes show a varying degree of ionic conduction above their glass transition temperature (T_g) where polymer segments undergo fairly large-amplitude motions.[20-22] Polyethyleneoxide (PEO; T_g = −50 to −57 ◦C) is one of the most widely studied host polymer for solvent-free electrolytes.[23-25] It is a nonflammable electrolyte that can dissolve a high concentration of various lithium salts, such as $Li^+CF_3SO_3^-$ and $Li^+(CF_3SO_2)_2N^-$ (=$Li^+Tf_2N^-$), to form solid polymer electrolytes (SPE).[20,23,26-33] Unfortunately, there are two major issues with ion transport of PEO/lithium salts: (1) its ionic conductivity is lower than that of the conventional organic electrolytes and (2) transference number of Li^+ ions is between 0.1 and 0.5, indicating that only a small fraction of the overall current is carried by the lithium ions.[34-38] There has been a significant effort to improve the electrolyte performance in the transference number. For example, DeSimone et al. studied a class of nonflammable electrolytes based on functionalized perfluoropolyethers (PFPEs).[39] These new electrolytes exhibit a remarkably high transference number close to unity, but their ionic conductivity is considerably lower than

that of PEO. To improve on the ionic conductivity, a series of blends of PFPE, PEO, and $Li^+Tf_2N^-$ were considered.[40] Compared to pure PFPE, these systems show a marked improvement in ionic conductivity by approximately two orders of magnitude but at the expense of the transference number.

The ionic/molecular interactions are the key factors that govern transport phenomena in electrolytes by directly modulating their structures.[41-44] Thus detailed information on local structures of the polymer matrix is important to understand the ionic conductivity and transference number. In this context, characterization of the ion-polymer and ion-ion interactions via computational analysis for PEO oligomers with coordinating salts offers useful insights at the atomistic/molecular level.[32,45-48] For instance, the coordination of metal ions (e.g., Li^+) to ether oxygen atoms of polyethers and subsequent changes in the polymer backbone's conformation has been very useful to understanding the transport properties of the electrolytes.[49] Furthermore, interaction of the cation with polyether oxygen atoms leads to weakening of cation-anion interactions,[50] which facilitates decoupling of cations and anions and thus increases the ionic conductivity.

Molecular electrostatics potential (MESP) arising from bare nuclear charges and electronic charge distributions of the system provides helpful insight into the cation-polymer complex formation. MESP brings about the effective localization of the electron-rich regions of the molecular system. The strength of such cation-anion interactions to form a neutral ion pair can also be quantified from the charge enclosed within a given MESP iso-surface. The MESP topography method has been applied to molecular interactions of different ion pairs in the solid polymer electrolytes.[51-52] In this article, we systematically investigate and compare the binding patterns of the PEO and PFPE with $Li^+Tf_2N^-$ using the

MESP topography as a tool to obtain molecular-level understanding of experimental results for ionic conductivity and lithium transference number. We also examine how the Li^+-polymer and Li^+-anion interactions manifest in the vibrational spectra using *ab initio* quantum chemical calculations. Natural bond orbital (NBO) analysis and molecular electron density (MED) topography coupled with different electron density maps are employed to gain insight into the reorganization of electron density as a consequence of these molecular interactions.

The outline of this paper is as follows: A brief description of computational methods employed is first given. DFT results for structure and vibrational frequencies are analyzed and related to Li^+-oligomer and Li^+-anion interactions next. Brief contact with conductivity measurements is also made. Concluding remarks are offered at the end.

2.3 Computational Method

To model PEO systems and their fluorinated counterpart for DFT calculations, $CR_3(OCR_2CR_2)_{n=1\text{-}5}OCR_3$ (R = H or F) was used. PEO is terminated with a methyl group at either end, so that when fluorinated, it can model PFPE reasonably well. Such methyl-terminated structures have been widely used in computational investigations of PEO/Li systems. In a previous study, molecular structures of pure diglyme (i.e., bis(2-methoxyethyl)ether) in gauche conformation were found to be similar in the presence and absence of a coordinated lithium ion.[53] This suggests that for lithium ion complexation, all-trans conformations are of minor importance and the gauche conformation provides the best candidate. Since no large conformation changes are needed for the latter to bind Li^+ with its ether oxygen atoms, this will minimize the energy cost for structural reorganization

of polymers. Therefore we will consider only gauche conformations for $CR_3(OCR_2CR_2)_{n=1-3,5}OCR_3$ in our study. For *n*=1 and 2, we studied 1:1:1 and 2:1:1 (ratio of the polymer, cation and anion numbers) SPE complexes. For *n*=3 and 5, we considered only 1:1:1 complexes. All structures were optimized via DFT using the B3LYP hybrid functional in all-electron 6-31G(d,p) basis set.[54,55] All the calculations were carried out with the GAUSSIAN03 program.[56]

To shed light on the effective localization of electron–rich regions in the molecular system, MESP was calculated by summing over all nuclei of the systems using the following equation

$$V(\mathbf{r}) = e\sum_{A=1}^{N}\frac{Z_A}{|\mathbf{r}-\mathbf{R}_A|} - e\int\frac{\rho(\mathbf{r}')d^3\mathbf{r}'}{|\mathbf{r}-\mathbf{r}'|}$$

where Z_A and $\mathbf{R}_A$ are the charge and position of nucleus A, $\rho(\mathbf{r})$ is the electron density and *e* is elementary charge. $V(\boldsymbol{r})$ consists of the bare nuclear potential and the electronic contributions. The topography of MESP is mapped by examining the eigenvalues of the Hessian matrix at the point where the gradient $V(\mathbf{r})$ vanishes. The MESP critical points (CPs) can be characterized by its rank and signature (excess of positive eigenvalues over negative ones). The minima and maxima are represented by (3, +3) and (3, -3), while (3, 1) and (3, +1) denote two different types of saddle points. The MESP CPs were visualized by using the package UNIVIS 2000.[57]

By checking the eigenvalues of the Hessian matrix, the stationary point geometries were confirmed to be true local minima on the potential energy surface. Binding energies have been calculated by subtracting the sum of the energies of the individual polymer and

the salt from the total energies of the polymer-salt complexes. Normal vibrations were assigned by visualizing the displacement of atoms around their equilibrium positions using the program UNIVIS2000.[57] Finally, natural bond orbital analysis and molecular electron density topography are performed.

2.4 Results and Discussions

We begin with the DFT results for $CR_3(OCR_2CR_2)OCR_3$ in the absence of a lithium salt. Geometry optimization of gauche conformation shows that substitution of hydrogen by fluorine atoms results in a considerable change in the structural parameters (Figure 2.1). The most noteworthy aspect is that the C-O and C-C inter-atomic distances are shortened and elongated, respectively, with the replacement of H with F (see *a* and *b* in Figure 2.1). To understand these changes in the inter-atomic distances, we examined the C-O-C and C-C-O angles. Our results show that while C-C-O angle, δ, remains nearly unchanged, C-O-C angle, θ, increases with the substitution with fluorine; the θ values are 112.7° and 119.7° for R = H and F, respectively. This indicates that with the H-to-F substitution, the hybridization character of oxygen orbitals changes from sp^3 to sp^2. This explains the change in the C-O bond distance, which tends to become shorter as the contribution of *p* orbitals to the hybridization becomes reduced.

The frontier orbitals (HOMO and LUMO) of molecules are the prime determinants of their chemical reactivity. A maximum overlap of the HOMO and LUMO of reacting species is desired for reactions and in the non-reactive case, enhanced interactions. For electrolytes PEO and PFPE, the oxygen atoms of polyether donate lone pair electrons to Li^+. Therefore, the HOMO level of the polymers is of interest. DFT predicts that the

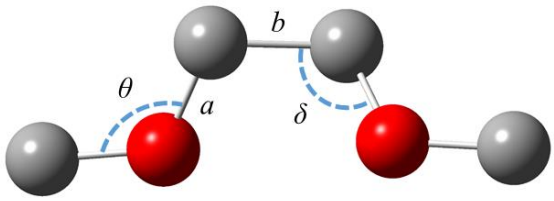

Figure 2.1. Optimized structure of $CR_3(OCR_2CR_2)OCR_3$ in the absence of lithium salts. The results for bond lengths (in Å) and angles (in degrees) are: a = 1.41 and 1.38, b = 1.52 and 1.55, θ = 112.7 and 119.7, and δ = 109.3 and 108.0 for R = H and F, respectively. Oxygen and carbon atoms are shown in red and dark gray, respectively. Hydrogen and fluorine atoms are not shown for clarity.

HOMO level of PFPE is more stable than that of PEO by 356.85 kJ/mol. This result indicates that the lone-pair electrons of PFPE are less accessible for the coordination of Li^+ than those of PEO. To explore the effective localization of the electron-rich regions of the molecular systems, and thus to find possible Li^+ binding sites of PEO and PFPE, the MESP topography was examined. MESP iso-surfaces (V = 13.13 kJ/mol/*e*) of gauche conformers of $CR_3(OCR_2CR_2)_{n=1\text{-}3,5}OCR_3$ (R=H or F) are shown in Figure 2.2. It is noteworthy that the localization of the electron density around oxygen atoms is more pronounced for PEO than for PFPE. The delocalization of electron density in PFPE is attributed to the electron withdrawing effect of fluorine atoms. The minimum values of MESP (m-MESP) near oxygen sites of PEO and PFPE are compiled in Table 2.1. The most prominent feature is that m-MESP near oxygen of PEO is considerably more negative than those of PFPE. We thus expect that Li^+ binds more strongly to oxygen atoms of PEO than those of PFPE, consonant with the observation above based on orbital hybridization.

To investigate the interactions of model polymers with Li^+, we placed lithium salt, i.e., a $Li^+Tf_2N^-$ ion pair, near oxygen sites of the oligoethers according to the results of m-MESP. The optimized structures of the models are shown in Figures 2.3 and 2.4. The

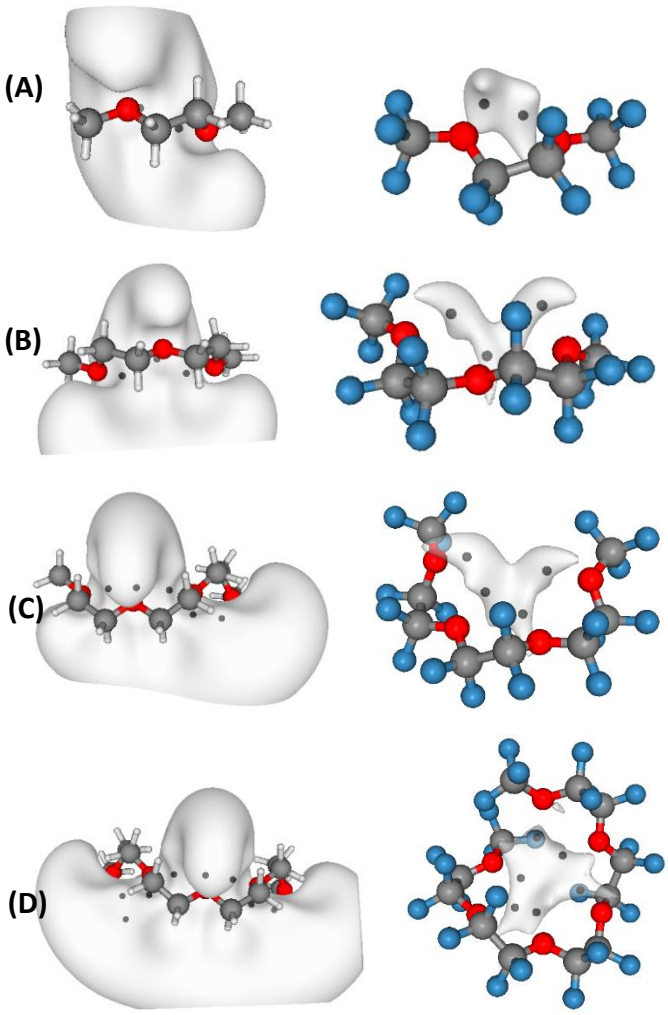

Figure 2.2. MESP iso-surfaces (V = 13.13 kJ/mol/*e*) of $CR_3(OCR_2CR_2)_nOCR_3$ (R=H or F) with (A) *n*=1, (B) *n*=2, (C) *n*= 3, and (D) *n* =5. Oxygen, carbon, hydrogen, and fluorine atoms are shown in red and dark gray, light gray, and light blue respectively.

Table 2.1. MESP minimum (in kJ/mol/*e*) near oxygen in different chain length of PEO and PFPE structures[a]

monoPEO	diPEO	triPEO	pentaPEO	monoPFPE	diPFPE	triPFPE	pentaPFPE
-221.5	-233.0	-241.6	-232.1	-36.5	-30.2	-36.3	-40.8
-221.5	-242.3	-222.5	-244.8	-36.5	-31.3	-34.0	-31.4
	-233.0	-225.3	-226.5		-21.3	-28.1	-29.3
		-231.8	-231.0			-25.4	-28.4
		-228.0	-228.1				-28.1
			-233.1				-24.1
			-244.9				
			-235.7				

[a]$CR_3(OCR_2CR_2)_{n=1\text{-}5}OCR_3$ where R = H is for PEO and R=F for PFPE; mono (*n*=1), di (*n*=2), tri (*n*=3), and penta(*n*=5).

interaction of Li^+ with oxygen atoms of the oligoethers engenders elongation of the oligoethers' C-O bonds compared to those in the absence of the lithium salt. DFT predicts that in the presence of one monoglyme ($CH_3(OCH_2CH_2)OCH_3$) unit (viz., 1:1:1 SPE complex), the lithium cation interacts with two oxygen atoms of the monoglyme with ΔE = -151.88 kJ/mol (Figure 2.3A), where ΔE is the energy difference between the SPE complex and the free PEO plus an isolated ion pair. Thus an energy is released upon complexation. The Li^+–O_{PEO} distance is found to be 1.993 Å. In the presence of two monoglyme units (2:1:1 complex), Li^+ interacts with three oxygen atoms of the oligomer units with ΔE = -197.90 kJ/mol (Figure 2.3B). The average Li^+–O_{PEO} distance in this case is 2.120 Å, about 0.13 Å longer than the case of a single monoglyme. For the 1:1:1 complex with one diglyme ($CH_3(OCH_2CH_2)_2OCH_3$) unit, the lithium cation couples to all three oxygen atoms of the diglyme with the average Li^+–O_{PEO} distance 2.131 Å and ΔE = -171.96 kJ/mol (Figure 2.3D). When two diglyme units are available (i.e., 2:1:1 complex), Li^+ still interacts with only three of six oxygen atoms of the oligomer backbones (Figure 2.3E). The resulting ΔE value and average Li^+–O_{PEO} distance are -207.94 kJ/mol and 2.124 Å. Analogous to diglyme, complexation of Li^+ with triglyme ($CH_3(OCH_2CH_2)_3OCH_3$) and pentaglyme ($CH_3(OCH_2CH_2)_5OCH_3$) occurs via coupling to three oxygen atoms of the oligomer chains with average Li^+–O_{PEO} distances of 2.111 and 2.089 Å, respectively (Figures 2.3C and 2.3F). To avoid any confusion, we mention that in real SPE, Li^+ ions, when fully dissociated from anions, will interact with more than 3 oxygen atoms of oligomers.

Turning to Li^+-anion interactions, we first note that Li^+ interacts with two oxygen atoms of the Tf_2N^- anion with Li^+–O* atomic distances of 1.810 Å in the isolated ion pair

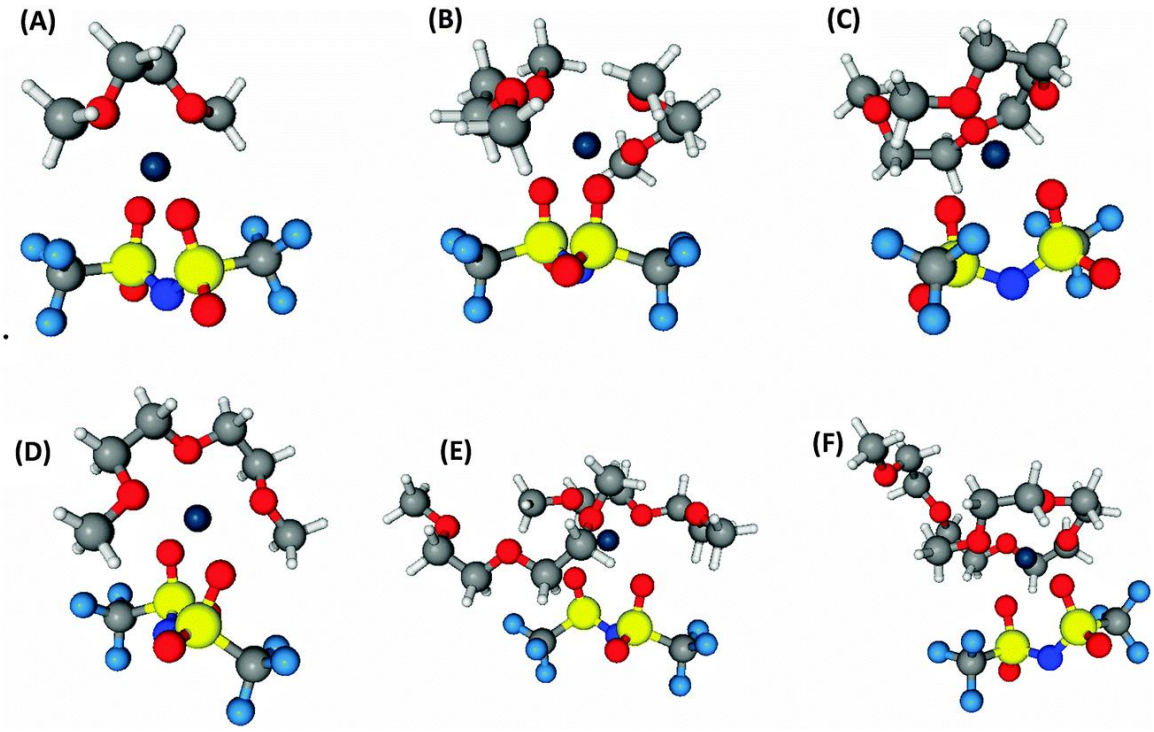

Figure 2.3. Optimized molecular structure of $Li^+Tf_2N^-$ in the presence of (A) one monoglyme unit, (B) two monoglyme units, (C) one triglyme unit, (D) one diglyme unit, (E) two diglyme units, and (F) one pentaglyme unit of PEO. Lithium, sulfur, nitrogen atoms are shown in black, yellow, and dark blue, respectively. The other color representations are the same as in Figure 2.2.

case (Figure 2.5). Here and hereafter, O* denotes oxygen atoms of Tf_2N^-, which interact directly with Li^+. Upon the formation of an SPE complex, Li^+-oligomer interactions pull the Li^+ ion away from the anion towards the oligomer. This leads to elongation of Li^+–O* distance, which in turn results in the contraction of S-O* bonds of the anion (Table 2.2). The overall cation-oligomer interaction strength depends on both the strength of the interaction of individual oligoether oxygen with Li^+ and the number of oxygen atoms interacting with Li^+. Both factors contribute to Li^+–O* and S-O* distances. Thus changes in these inter-atomic distances can serve as a reasonable measure of the strength of Li^+-anion and thus Li^+-oligomer interactions; viz., the stronger the Li^+-oligomer interactions and therefore the weaker Li^+-anion interactions, the longer (and thus weaker) and shorter

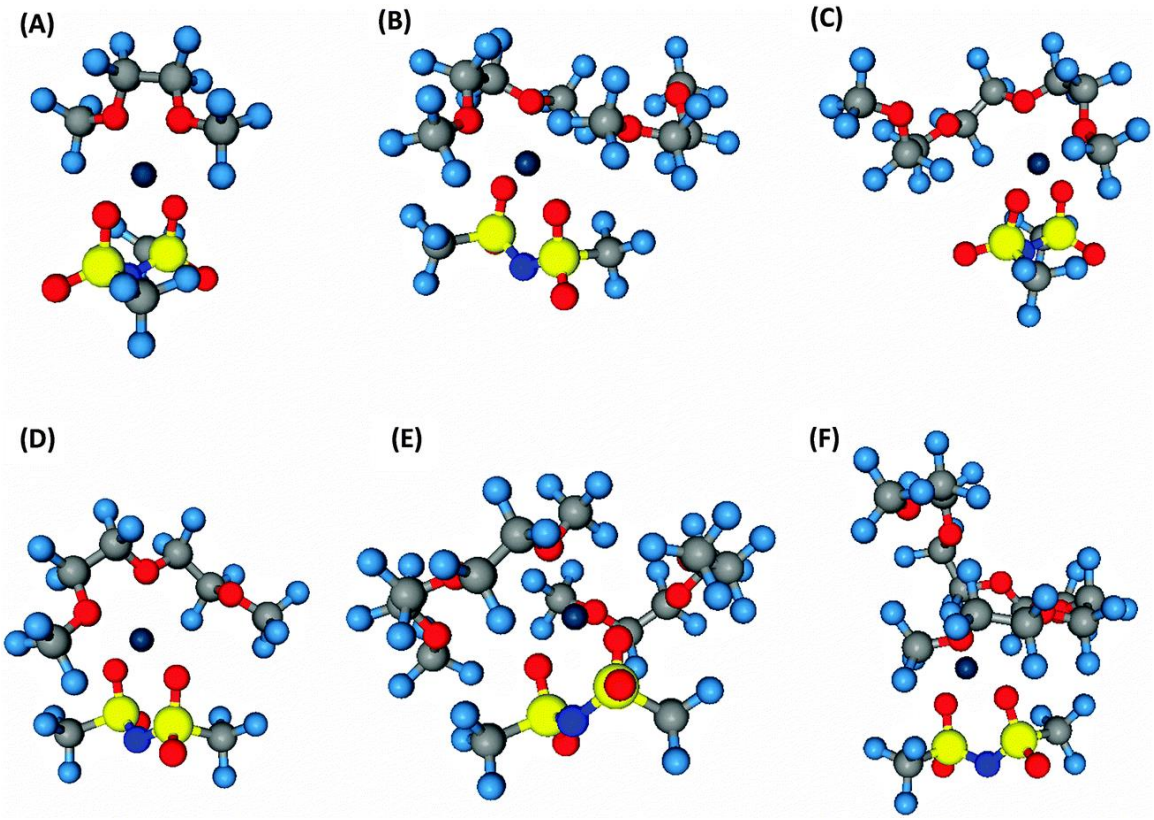

Figure 2.4. Optimized molecular structure of $Li^+Tf_2N^-$ in the presence of (A) one monoglyme unit, (B) two monoglyme units, (C) one triglyme unit, (D) one diglyme unit, (E) two diglyme units, and (F) one pentaglyme unit of PFPE. The color representations are the same as in Figure 2.3.

(and thus stronger) the Li^+–O* and S-O* bonds, respectively. It is worth noting that the Li^+–O* and S- O*distances are, respectively, longer and shorter in the 2:1:1 SPE complex with two diglyme units than in the 1:1:1 complex with one diglyme unit. Thus Li^+-anion interactions are weakened in the former compared to the latter even though Li^+ interacts with three O atoms of PEO in both cases. This suggests that increase in the extent of solvation of the $Li^+Tf_2N^-$ ion pair in PEO reduces the ion pair interactions and facilitates its dissociation. In this context, among six different SPE complexes of PEO and Li^+ we studied here (Figure 2.3), the presence of two diglyme units appears to provide the best environment for dissociation of the ion pair, according to the results in Table 2.2.

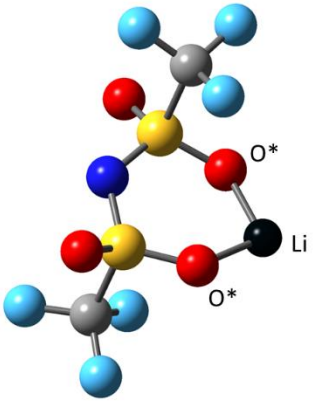

Figure 2.5. Optimized molecular structure of $Li^+Tf_2N^-$ in gas phase. The color representations are the same as in Figure 2.3.

Table 2.2. Selected bond lengths (in Å) for different $CH_3(OCH_2CH_2)_{n=1\text{-}5}OCH_3\text{-}Li^+Tf_2N^-$ complexes[a,b]

	monoPEO	2monoPEO	diPEO	2diPEO	triPEO	pentaPEO
CO	1.430	1.430	1.430	1.433	1.430	1.433
	1.426	1.421	1.421	1.420	1.422	1.417
	1.426	1.422	1.423	1.428	1.426	1.413
	1.430	1.427	1.423	1.429	1.429	1.418
		1.421	1.421	1.415	1.425	1.432
		1.428	1.430	1.418	1.432	1.427
		1.420		1.428	1.420	1.427
		1.414		1.431	1.414	1.425
				1.420		1.431
				1.417		1.433
				1.415		1.416
				1.412		1.418
SO*	1.494	1.490	1.491	1.489	1.486	1.492
	1.493	1.488	1.492	1.490	1.492	1.487
SO	1.455	1.463	1.461	1.459	1.459	1.463
	1.455	1.456	1.465	1.466	1.457	1.455
SN	1.610	1.612	1.617	1.618	1.607	1.609
	1.610	1.604	1.605	1.606	1.614	1.611
$Li^+–O_{PEO}$	1.991	2.098	2.128	2.149	2.035	2.095
	1.994	2.141	2.094	2.165	2.153	2.157
		2.048	2.170	2.057	2.146	2.014
$Li^+–O_{Anion}$	1.889	1.977	1.951	2.033	1.969	1.987
	1.892	2.012	1.982	2.073	1.979	1.994

[a]Free anion: SN = 1.620; SO= 1.468, 1.469, 1.468, 1.469.
[b]$Li^+Tf_2N^-$ ion pair in vacuum: SN = 1.606; SO* = 1.504; SO =1.452; Li^+–O=1.810.
[c]Average CO bond distance of pure PEO = 1.413

We now proceed to PFPE systems and consider the effect of the replacement of H by F in oligomers on SPE complexes. The conformers of PFPE we studied (Figure 2.4) are similar to those of PEO discussed above (Figure 2.3). Two aspects are noteworthy. First, Li^+ interacts with two oxygen and one fluorine atoms of PFPE in contrast to three oxygen atoms in the case of PEO. Second, Li^+–O_{PFPE} distances are longer than those of Li^+–O_{PEO} (Tables 2.2 and 2.3). The latter indicates that cation-polymer interactions are weakened in the presence of PFPE compared to the PEO case. This is in good agreement with the analysis of the MESP topography above. The weakened cation-oligomer interactions result in (relatively) strong cation-anion interactions in PFPE, compared to those in PEO. This is manifested in S-O* bond lengths and Li^+–O* distances, which are, respectively, elongated and shortened in PFPE with respect to the PEO case. This means that the dissociation of Li^+-Tf_2N^- ion pairs will be less energetically favorable and thus less probable in PFPE-type electrolytes than in PEO. As a result, there will be fewer free ions available for ion conduction in the former than in the latter. This provides a theoretical explanation for low ionic conductivity observed experimentally in PFPE electrolytes, compared to PEO.[39,40] However, we think that Li^+–$O_{polymer}$ interactions are a "double-edged sword" in that while they facilitate the lithium salt dissociation by weakening Li^+-anion interactions as discussed above, their enhancement would hinder Li^+ transport by strongly binding Li^+ ions to polymers. This aspect of Li^+–$O_{polymer}$ interactions explains why the lithium transference number is considerably lower in PEO than in PFPE.[39,40]

For additional insight into interactions of Li^+ ions with anions and oligoethers, we have analyzed vibrational spectra of $Li^+Tf_2N^-$-oligomer complexes. Though approximate, theoretically calculated harmonic vibrational frequencies are useful to understanding

Table 2.3. Selected bond lengths (in Å) for different $CF_3(OCF_2CF_2)_{n=1-5}OCF_3$-$Li^+Tf_2N^-$ complexes[a,b,c]

	monoPFPE	2monoPFPE	diPFPE	2diPFPE	triPFPE	pentaPFPE
CO	1.407	1.400	1.399	1.402	1.410	1.389
	1.395	1.393	1.368	1.391	1.390	1.374
	1.396	1.393	1.500	1.379	1.399	1.382
	1.407	1.401	1.399	1.390	1.401	1.386
		1.375	1.408	1.376	1.399	1.379
		1.390	1.391	1.386	1.368	1.388
		1.381		1.388	1.381	1.368
		1.386		1.377	1.392	1.393
				1.389		1.378
				1.379		1.390
				1.387		1.380
				1.408		1.386
SO*	1.501	1.497	1.501	1.499	1.501	1.497
	1.499	1.498	1.499	1.498	1.500	1.497
SO	1.454	1.455	1.455	1.455	1.456	1.454
	1.457	1.454	1.459	1.461	1.460	1.454
SN	1.601	1.605	1.602	1.601	1.601	1.605
	1.611	1.607	1.613	1.613	1.616	1.607
Li^+–O_{PFPE}	2.117	2.230	2.259	2.325	2.210	2.922
	2.105	2.213	2.170	2.249	2.221	
Li^+–F_{PFPE}	-	2.340	2.395	2.642	2.363	2.040
Li^+–O_{Anion}	1.835	1.876	1.853	1.860	1.852	1.852
	1.837	1.862	1.852	1.874	1.853	1.856

[a]For bond distances for the free anion and ion pair in vacuum, see footnotes of Table 2.2
[b]Average CO bond distance of pure PFEF = 1.383

structural changes induced by molecular interactions, in particular, between metal ions and oligomers as they are manifested as spectral changes. Selected stretching vibrations of PEO and PFPE in the absence and presence of $Li^+Tf_2N^-$ are presented in Tables 2.4 and 2.5, respectively. The vibrations in the frequency range of 1155-1185 cm^{-1} (1125-1175 cm^{-1}) are assigned to C-$O_{polymer}$ stretching vibrations of PEO (PFPE) in the absence of Li^+. For clarity, we note that these normal stretching vibrational modes have CH_2 bending components, such as wagging, twisting, and scissoring, due to coupling of local vibrational modes. In the presence of Li^+, the C-$O_{polymer}$ vibrations, especially those involving $O_{polymer}$

atoms that interact directly with Li^+, become red shifted with respect to those in pure PEO/PFPE. These red shifts correlate reasonably well with the Li^+-oligoether interaction strength.

Table 2.4. Selected vibrational frequencies for isolated PEOs and $CH_3(OCH_2CH_2)_{n=1-5}OCH_3$-$Li^+Tf_2N^-$ complexes

	Mono PEO	Li-monoPEO	Li-2monoPEO	diPEO	Li-diPEO	Li-2diPEO	triPEO	Li-triPEO	pentaPEO	Li-pentaPEO
CO str	1181 (17)	1152 (68)	1171 (51)	1175 (68)	1172 (74)	1179 (33)	1183 (76)	1173 (66)	1183 (99)	1182 (67)
	1159 (252)	1118 (256)	1157 (58)	1158 (259)	1140 (243)	1171 (23)	1171 (130)	1168 (57)	1175 (99)	1179 (91)
										1172 (56)
						1149 (202)	1157 (319)	1159 (54)	1162 (240)	1167 (56)
			1136 (228)			1148 (187)		1149 (70)	1156 (282)	1163 (94)
			1124 (204)			1133 (103)		1139 (124)		1152 (213)
			1122 (52)			1116 (298)				
						1106 (54)				
SO str		1321 (481)	1303 (414)		1283 (510)	1302 (413)		1321 (463)		1283 (308)
		1302 (299)	1286 (420)		1269 (391)	1280 (1280)		1298 (310)		1261 (225)
SO* str		1086 (96)	1098 (206)		1095 (392)	1095 (177)		1093 (93)		1099 (201)
		1072 (280)	1077 (206)		1068 (27)	1065 (191)		1076 (237)		1073 (210)
SN str		1011 (519)	1017 (476)		1010 (488)	1005 (490)		1011 (470)		1009 (240)

Free anion: SO str = 1324 (444), 1300 (71); SN str = 999 (582).
$Li^+Tf_2N^-$ ion pair in vacuum: SO str = 1324 (396), 1305 (354); SO* str = 1069 (161), 1062 (536); SN str = 1011 (429).

In the case of S-O* stretching vibrations, a blue shift is obtained in SPE, compared to an isolated $Li^+Tf_2N^-$ ion pair. Additionally, S-O* stretching vibrations are higher in frequencies in PEO than in PFPE. As mentioned above, the Li^+-oligomer interactions weaken the Li^+-anion interactions and as result strengthen S-O* bonds. For better understanding of this aspect, we carried out NBO (Natural Bond Orbital) analysis to examine changes in the strength of anion bonds, caused by the Li^+-oligomer and Li^+-anion interactions. The electron density in the antibonding orbital of the S-O* and S-O bonds of

Table 2.5. Selected vibrational frequencies for isolated PFPEs and $CF_3(OCF_2CF_2)_{n=1-5}OCF_3$- $Li^+Tf_2N^-$ (units: cm^{-1})

	monoPFPE	Li-mono PFPE	Li-2monoPFPE	diPFPE	Li-diPFPE	Li-2diPFPE	triPFPE	Li-triPFPE	pentaPFPE	Li-pentaPFPE
CO str	1172 (160)	1134 (356)	1170 (174)	1171 (750)	1159 (413)	1173 (204)	1170 (317)	1170 (363)	1175 (335)	1178 (214)
					1132 (442)	1161 (204)	1162 (1214)	1171 (599)	1171 (599)	1171 (245)
	1154 (1165)	1092 (1219)	1151 (882)		1116 (61)	1155 (591)	1125 (726)	1166 (99)	1166 (99)	1163 (349)
			1138 (706)	1137 (1021)	1090 (493)	1151 (589)		1161 (736)	1161 (736)	1162 (746)
			1100 (808)			1120 (518)		1141 (1080)	1141 (1080)	1151 (756)
						1109 (855)				1130 (553)
						1105 (52)				1110(143)
SO str		1309 (1149)	1320 (875)		1311 (359)	1307 (857)		1307 (209)		1323 (402)
		1295 (565)	1301 (360)		1289 (1015)	1295 (350)		1292 (92)		1303 (339)
SO* str		1083 (354)	1081 (172)		1086 (878)	1082 (289)		1080 (822)		1082 (230)
		1064 (330)	1071 (322)		1058 (218)	1058 (237)		1055 (215)		1070 (285)
SN str		1016 (315)	1016 (327)		1012 (301)	1013 (314)		1011 (336)		1016 (362)

the anion in various SPE complexes are summarized in Tables 2.6 and 2.7. Compared to an isolated anion, the Li^+-anion interactions yield an increase in the electron density in the localized antibonding orbital of the S-O* bonds of the anion, due to charge transfer mainly from O* to the alkali metal. This results in weakening of the S-O* bonds, concomitantly with the elongation of their bond lengths and a red shift of their stretching vibrations compared to the corresponding vibration in the infrared spectrum of the free anion. In addition, the resulting anion electron density redistribution leads to transfer of electron density to its non-interacting S-O bonds in these SPEs. This increases the strength of these S-O bonds, accompanied by bond contraction and hence an upshift of their vibrational frequencies.

Table 2.6. Electron density (in au) of anti-bonding orbitals of selected bonds in the anions

Bond	Li-monoPEO	Li-2monoPEO	Li-diPEO	Li-2diPEO	Li-triPEO	Li-pentaPEO
SO*	0.1971	0.1909	0.1909	0.1902	0.1967	0.1905
	0.1966	0.1871	0.1874	0.1852	0.1897	0.1897
SO	0.1380	0.1455	0.1490	0.1482	0.1397	0.1447
	0.1386	0.1610	0.1654	0.1684	0.1435	0.1578

Free Anion: SO = 0.15875, 0.17503, 0.15875, 0.17503

$Li^+Tf_2N^-$ in pair in vacuum: SO* = 0.20594, 0.20592; SO = 0.13433, 0.13431

Table 2.7. Electron density (in au) of anti-bonding orbitals of selected bonds in the anions

Bond	Li-monoPFPE	Li-2monoPFPE	Li-diPFPE	Li-2diPFPE	Li-triPFPE	Li-pentaPFPE
SO*	0.2021	0.2003	0.2001	0.2010	0.1932	0.1985
	0.1971	0.1967	0.1954	0.1959	0.1997	0.1975
SO	0.1325	0.1362	0.1373	0.1359	0.1390	0.1436
	0.1518	0.1423	0.1570	0.1566	0.1597	0.1413

One of the potential advantages of S-O* stretching vibrations, though limited to anions with sulfonyl groups, over $C\text{-}O_{polymer}$ vibrations from experimental perspective is that the former are relatively more intense and are not strongly coupled with other local vibration modes. As such, S-O* vibrations would be hard to miss in the experimental spectra, thereby offering a good empirical measure for Li^+-oligomer and Li^+-anion interaction strengths. For instance, the S-O* stretching frequencies of SPE complexes in which Li^+ interacts with three oxygen atoms of PEO (i.e, complexes with di-, tri- and penta-glymes as well as the 2:1:1 complex with two mono-glyme units) are generally shifted towards higher frequencies compared to those of the 1:1:1 complex with a single mono-glyme unit in which Li^+ interacts with just two oxygen atoms. This indicates that the strength of Li^+-PEO interactions increases as more oxygen atoms of PEO become coordinated with Li^+. Between PFPE- and PEO-based electrolytes, the S-O* stretching

frequencies in PFPE are red shifted with respect to those in PEO. This provides another evidence that Li^+-oligoether interactions are weaker in the former than in the latter.

Finally we consider the MED critical point (cf. section 2) topography for our model SPE complexes. As demonstrated in previous work on ion pair interactions, the strength of the short-range intermolecular interactions can be well correlated to the electron density at the bond critical point (BCP) of their interaction path ("bond path").[58-60] (BCP is a saddle point of type (3,-1), viz., its value is a maximum in two directions and a minimum in the third direction in three-dimensional space.) Therefore, they can provide additional insight into the bond strengths and the direction of vibration frequency shifts, caused by the changes in the anion-cation interactions. The DFT results are presented in Tables 2.8 and 2.9. The BCP values for interionic/intermolecular Li^+–O bond paths for both anion and oligoether oxygen atoms are in the range of 0.02-0.035 au, which are about one order of magnitude smaller than the typical BCP values of chemical bonds. Nonetheless, the presence of BCPs between Li^+ and PEO and (Li^+ and PFPE) indicates that their Li^+–O interactions resemble bonded interactions. The absence of a BCP in interactions of Li^+ with some O atoms of PFPE suggests that they are non-bonded interactions and thus are not as strong as their bonded interaction counterparts. Another noteworthy feature is that the magnitude of BCP for Li^+–$O_{polymer}$ for PEO is considerably larger than that for PFPE. This confirms our findings based on the Li^+–O distances and the S-O* stretching frequencies above that Li^+–$O_{polymer}$ interactions in SPE complexes are stronger with PEO than with PFPE. Similarly, the BCP results for Li^+–O_{Anion} confirm that Li^+-anion interactions become weakened in the presence of PEO, compared to PFPE.

Table 2.8. Electron density (in au) at the BCP of Li^+–O interaction paths in $CH_3(OCH_2CH_2)_{n=1\text{-}5}OCH_3$-Li-$Tf_2N$

Bond	Li- monoPEO	Li-2monoPEO	Li-diPEO	Li-2diPEO	Li-triPEO	Li-pentaPEO
Li^+–O_{PEO}	0.02449	0.01795	0.01731	0.01679	0.02168	0.01627
	0.02436	0.01699	0.01560	0.01155	0.01653	0.01861
		0.02023	0.01882	0.01483	0.01632	0.02226
Li^+–O_{Anion}	0.02997	0.02114	0.02310	0.01816	0.02328	0.02231
	0.02973	0.02318	0.02535	0.02001	0.02363	0.02256

Table 2.9. Electron density (in au) at the BCP of Li^+–O interaction paths in $CF_3(OCF_2CF_2)_{n=1\text{-}5}OCF_3$-Li-$Tf_2N$

Bond	Li- monoPFPE	Li-2monoPFPE	Li-diPFPE	Li-2diPFPE	Li-triPFPE	Li-pentaPFPE
Li^+–O_{PEO}	0.01612	0.01188	0.01208	0.009082	0.01273	
	0.01676	0.01267	0.01323		0.01278	
Li^+–O_{Anion}	0.03508	0.03238	0.03372	0.03200	0.03377	0.03312
	0.03498	0.03119	0.03346	0.03284	0.03389	0.03335

2.5 Conclusions

In this study, we have investigated molecular interactions between oligoethers $CR_3(OCR_2CR_2)_{n=1\text{-}5}OCR_3$ (where R = H or F) and a $Li^+Tf_2N^-$ ion pair via DFT calculations. Our results indicate that replacement of H with F in oligoethers results in change of hybridization of their oxygen atoms from sp^3 to sp^2. This stabilizes the C-O bonds of the oligoethers and lowers the HOMO energy, which in turn reduces interactions of the oligoethers with Li^+ ion. Further, we analyzed the molecular electrostatic potential and natural bond orbital of the oligoethers in the presence and absence of the lithium salt. These analyses along with the S-O stretching vibrations of the anion show fluorination of PEO leads to a strong reduction of Li^+-affinity of the polymer. This finding provides a theoretical explanation for low ionic conductivity observed experimentally for PFPE electrolytes, compared to PEO. It also explains why the lithium transference number is much higher in PFPE than in PEO. Thus our study here offers helpful insight into the Li^+-polymer complex

formation to design and synthesize new solid electrolyte polymers with improved ionic conductivity and transference number to meet the ever increasing demand of high performance and safe energy storage devices. Therefore, it would be worthwhile in the future to extend this study to investigate actual kinetics of Li^+ transport at the first principles level.

2.6 Acknowledgments

This work is supported in part by the Samsung GRO Program.

2.7 References

1) B. Scrosati, *Nature*, 1995, **373**, 557- 558.
2) S. P. Beaton, G. A. Bishop, Y. Ziang, L. L. Ashbaugh, D. R. Lawson and D. H. Stedman. *Science*, 1995, **268**, 991-993.
3) S. Manzettia and F. Mariasiu, *Renew. Sustain. Energy Rev.*, 2015, **51**, 1004-1012.
4) J. M. Tarascon and M. Armand, *Nature*, 2001, **414**, 359-367.
5) J. B. Goodenough and K. S. Park, *J. Am. Chem. Soc.* 2013, **135**, 1167-1176.
6) F. Y. Cheng, J. Liang, Z. L. Tao and J. Chen, *Adv. Mater.*, 2011, **23**, 1695–1715.
7) J. B. Goodenough, Y. Kim, *Chem. Mater.*, 2010, **22**, 587–603.
8) E. J. Plichta, M. Hendrickson, R. Thompson, G. Au, W. K. Behl, M. C. Smart, B. V. Ratnakumar, and S. Surampudi, *J. Power Sources*, 2001, **94**, 160- 162.
9) A. Hammami, N. Raymond and M. Armand, *Nature*, 2003, **424**, 635- 636.
10) B. K. Mandal, A. K. Padhi, Z. Shi, S. Chakraborty and R. Filler, *J. Power Sources*, 2006, **161**, 1341-1345.
11) T. Kawamuraa, A. Kimura, M. Egashira, S. Okada and J. Yamaki, *J. Power Sources*, 2002, **104**, 260–264
12) Q. Wang, P. Ping, X. Zhao, G. Chu, J. Sun and C. Chen, *J. Power Sources*, 2012, **208**, 210–224.
13) M. Armand, F. Endres, D. R. MacFarlane, H. Ohno and B. Scrosati, *Nat. Mater.*, 2009, **8**, 621–629.
14) L. Lombardo, S. Brutti, M. A Navarra, S. Panero and P. Reale, *J. Power Sources*, 2013, **227**, 8–14.
15) M. Egashira, H. Todo, N. Yoshimoto and M. Morita, *J. Power Sources*, 2008, **178**, 729–735.
16) J. Y. Song, Y. Y. Wang and C. C. Wan, *J. Power Sources*, 1999, **77**,183–197.
17) L. Wu, Z. Song, L. Liu, X. Guo, L. Kong, H. Zhan, Y. Zhou and Z. Li, *J. Power Sources*, 2009, **188**, 570–573.

18) G. Nagasubramanian and C. J. Orendorff, *J. Power Sources*, 2011, **196**, 8604–8609.
19) K. Naoi, E. Iwama, N. Ogihara, Y. Nakamura, H. Segawa and Y. Ino, *J. Electrochem. Soc.*, 2009 **156**, A272-A276.
20) M. Wakihara, *Mater. Sci. Eng. R*, 2001, **33**,109–134.
21) M.A. Ratner and D.F. Shriver, *Chem. Rev.*, 1988, **88**,109–124.
22) B. L. Papke, M. A. Ratner and D. F. Shriver, *J. Electrochem. Soc.*, 1982, **129**, 1694–1701
23) F. Croce, G. B. Appetecchi, L. Persi and B. Scrosati, *Nature*, 1998, **394**, 456–458.
24) J. W. Fergus, *J. Power Sources*, 2010, **195**, 4554–4569.
25) D. T. Hallinan and N. P. Balsara, *Annu. Rev. Mater. Res.* 2013, **43**, 503-525.
26) S. P. Gejji, P. R. Agrawal and N. R. Dhumal. *Theor. Chem. Acc.*, 2002, **107**, 351-356.
27) S. P. Gejji, K. Hermansson, J. Tegenfeldt and J. Lindgern. *J. Phys. Chem*, 1993, **97**, 11402- 11407.
28) G. N. Malcolm and J. S. Rowlinsnon. *Trans. Farady. Soc.*, 1957, **53**, 921-931.
29) J. F. Le Nest, S. Callens, A. Gandini and M. Armand, *Electrochimica Acta*, 1992, **37**, 1585–1588
30) A. Nishimoto, M. Watanabe, Y. Ikeda and S. Kohjiya, *Electrochimica Acta*, 1998, **43**, 1177–1184
31) L. Rey, P. Johansson, J. Lindgren, J. C. Lassegues, J. Grondin and L. Servant, *J. Phys. Chem A*, 1998, **102**, 3249-3258.
32) P. G. Bruce and F. M. Gray. Solid state electrochemistry. Cambridge University Press, New York, page 119, 1995.
33) J. R. Maecallum and C. A. Vincent. Polymer electrolyte reviews-I. El-sevier, London, 1987.
34) A. Ghosh, C. Wang and P. Kofinas, *J. Electrochem Soc*, 2010, **157**, A846–A849.
35) F. Capuano, F. Croce and Scrosati B, *J. Electrochem Soc*, 1991, **138**, 1918–1922.
36) G. B. Appetecchi, D. Zane and B. Scrosati, *J. Electrochem Soc*, 2004, **151**, A1369–A1374.
37) J. Evans, C. A. Vincent and P. G. Bruce PG, *Polymer (Guildf)*, 1987, **28**, 2324–2328.
38) M. Watanabe and A. Nishimoto, *Solid State Ionics*, 1995, **79**, 306–312.
39) D. H. C. Wong, J. L. Thelen, Y. Fu, D. Devaux, A. A. Pandya, V. S. Battaglia, N. P. Balsara and J. M. Desimone, *Proc. Natl. Acad. Sci. U.S.A.*, 2014, **111**, 3327-3331
40) D. H. C. Wong, A. Vitale, D. Devaux, A. Taylor, A. A. Pandya, D. T. Hallinan, J. L. Thelen, S. J. Mecham, S. F. Lux, A. M. Lapides, P. R. Resnick, T. J. Meyer, R. M. Kostecki, N. P. Balsara and J. M. DeSimone, *Chem. Mater.* 2015, **27**, 597–603.
41) A. Sutjianto and L. A. Curtiss. *J. Phys. Chem. A*, 1998, **102**, 968-974.
42) R. Frech and W. Huang. *Solid State Ionics*, 1994, **72**, 103-107.
43) C. C. Addison, D. W. Amos, and D. Sutton. *J. Chem. Soc.*, 1968, 2285.
44) S. P. Gejji, P. Johansson, J. Tegenfeldt, and J. Lindgren, *Comput. Polymer Science*, 1995, 5, 99-105.
45) N. R. Dhumal and S. P. Gejji, *Chem. Phys.*, 2006, **323**, 595-605.

46) S. Bhattacharja, S. W. Smoot and D. H. Whitmore, *Solid State Ionics*, 1986, **18-19**, 306-314.
47) S. Arumugam, J. Shi, D.P. Tunstall and C.A. Vincent, *J. Phys. Condens Matter*, 1993, **5**, 153-160.
48) N. Boden, S. A. Leng and I. M. Ward, *Solid State Ionics*, 1991, **45**, 261-270.
49) P. Johansson, S.P. Gejji, J. Tegenfeldt and J. Lindgren, *Solid State Ionics*, 1996, **86**, 297-302.
50) P. Johansson and P. Jacobsson. *J. Phys. Chem. A*, 2001, **105**, 8504-8509.
51) N. R. Dhumal and S. P. Gejji, *Theor. Chem. Acc.*, 2006, **115**, 308-321.
52) S. P. Gejji, P. R. Agarwal and N. R. Dhumal, *Theor Chem. Acta.* 2002, **107**, 351-356.
53) G. J. Kearley, P. Johansson, R. G. Delaplane and J. Lindgren, *Solid State Ionics*, 2002, **147**, 237- 246.
54) A. D. Becke, *J. Chem. Phys.*, 1993, 98, 5648–5652.
55) C. Lee, W. Yang and R. G. Parr, *Phys.Rev. B.*, 1988, **37**, 785-789.
56) Gaussian 03, Revision C.02, M. J. Frisch, G. W. Trucks, H. B. Schlegel, G. E. Scuseria, M. A. Robb, J. R. Cheeseman, J. A. Montgomery, Jr., T. Vreven, K. N. Kudin, J. C. Burant, J. M. Millam, S. S. Iyengar, J. Tomasi, V. Barone, B. Mennucci, M. Cossi, G. Scalmani, N. Rega, G. A. Petersson, H. Nakatsuji, M. Hada, M. Ehara, K. Toyota, R. Fukuda, J. Hasegawa, M. Ishida, T. Nakajima, Y. Honda, O. Kitao, H. Nakai, M. Klene, X. Li, J. E. Knox, H. P. Hratchian, J. B. Cross, V. Bakken, C. Adamo, J. Jaramillo, R. Gomperts, R. E. Stratmann, O. Yazyev, A. J. Austin, R. Cammi, C. Pomelli, J. W. Ochterski, P. Y. Ayala, K. Morokuma, G. A. Voth, P. Salvador, J. J. Dannenberg, V. G. Zakrzewski, S. Dapprich, A. D. Daniels, M. C. Strain, O. Farkas, D. K. Malick, A. D. Rabuck, K. Raghavachari, J. B. Foresman, J. V. Ortiz, Q. Cui, A. G. Baboul, S. Clifford, J. Cioslowski, B. B. Stefanov, G. Liu, A. Liashenko, P. Piskorz, I. Komaromi, R. L. Martin, D. J. Fox, T. Keith, M. A. Al-Laham, C. Y. Peng, A. Nanayakkara, M. Challacombe, P. M. W. Gill, B. Johnson, W. Chen, M. W. Wong, C. Gonzalez, and J. A. Pople, Gaussian, Inc., Wallingford CT, 2004.
57) A. C. Limaye, S. R. Gadre, *Curr. Sci. (India)* 2001, **80**, 1298.
58) N. R. Dhumal, J. Kiefer, H. J. Kim, J. Phys. Chem A. 2009, **113**, 10397-10404.
59) N. R. Dhumal, J. Kiefer, H. J. Kim, J. Phys. Chem A. 2011, **115**, 3551-3558.
60) N. R. Dhumal, K. Noack, J. Kiefer, H. J. Kim, J. Phys. Chem A. 2014, **118**, 2547-2557.

Chapter 3: *Activation of Au_{25} gold nanoparticles for catalytic reactions*

3.1 Abstract

The catalytic activity of $Au_{25}(SR)_{18}$ nanoclusters (–SR = thiolate ligands) for different reactions, including aldehyde hydrogenation, the Suzuki cross-coupling, and the Ullmann hetero-coupling reactions, are studied. This chapter shows the addition of transition-metal ions as a Lewis acid (M^{z+} = Cu^{+}, Cu^{2+}, Ni^{2+}, and Co^{2+}) and imidazolium-based ionic liquids (ILs) can significantly promote the catalytic activity of $Au_{25}(SR)_{18}$ nanoclusters. Using density functional theory calculations, generation of new species, $Au_{25-n}(SR)_{18-n}$, in the presence of the promoters (i.e, Lewis-acid and IL) is investigated. The pathways for the speciation of $Au_{24}(SR)_{17}$ from its parent $Au_{25}(SR)_{18}$ nanocluster as well as its structure are investigated via DFT method. The adsorption of M^{z+} or imidazolium-based cation onto a thiolate ligand "–SR–" of $Au_{25}(SR)_{18}$, followed by detachment of "Au-SR" units is found to be the most likely mechanism for the $Au_{25-n}(SR)_{18-n}$ generation. This in turn exposes the Au_{13}-core of $Au_{24}(SR)_{17}$ to reactants, providing active sites for the catalytic reactions. DFT calculations indicate that M^{z+} is also capable of adsorbing onto the Au_{13}-core surface, producing a possible active metal site of a different kind to catalyze the reactions. This study suggests, for the first time, that species with an open metal site like adducts $[nanoparticle\text{-}M]^{(z-1)+}$ or fragments $Au_{25-n}(SR)_{18-n}$ function as the catalysts rather than the intact $Au_{25}(SR)_{18}$. Further, it is shown that the activity and selectivity of the catalyst are largely influenced by the chemical nature of the protecting thiolate ligands. This study highlights that the aromatic ligands lead to not only a higher conversion in catalytic reaction but also markedly increase the yield of the hetero-coupling product of the Ullmann hetero-coupling reactions.

Keywords: Gold, Nanoclusters, Au_{25}, Catalysis, Reaction Mechanism

3.2 Introduction

Ever since the catalytic manufacture of lead chamber sulfuric acid by J. Roebuck in 1746, chemical catalysis has played a vital role in the industrial applications and development of the modern society.[1-5] Currently, almost all of the manufactured materials rely on catalytic reaction technology. However, design and development of environmentally more friendly processes in the chemical industry is a must due to the vast amount of industrial waste stream produced each year.[6-10] The "Green Chemistry", with principles formulated by the U.S. Environmental Protection Agency, is the design of novel chemical processes to minimize the use/generation of hazardous substances which ultimately enter to the waste stream.[11] In this regard, a key technology development effort is the research on catalytic technology for green manufacture and application of fuel and chemicals. For examples, green catalysts are used in biomass feedstocks,[12-14] organic synthesis,[15,16] olefin metathesis,[17,18] medicines development,[19] and biodegradable plastics.[20]

Catalysts can be divided into two main categories: heterogeneous and homogeneous. The major advantage of heterogeneous catalysts over the homogenous ones are simpler and cheaper separation and re-utilization of the catalysts after chemical reactions.[21-23] In this regard, a variety of transition metals in different forms have been examined for chemical syntheses, petroleum refinery, and environmental protection.[24-34] Unfortunately, heterogeneous catalysis often suffers from low specificity that leads to the formation of side products. This poses a serious challenge from the environmental and economic perspectives for their applications in chemical industries. Despite many transition metals, gold is found to be highly specific in many heterogeneous catalytic reactions, providing an exciting opportunity for their green use in large scales. [35,36]

The surface chemistry of the bulk materials is generally considered to be negligible due to their low surface-to-volume ratios. However, the chemical potential of materials increases as their size deceases. This often results in superior surface effects that dominates the overall material behavior. Therefore, materials in nanosize such as nanoparticles, nanowires, and nanolayers have gained overwhelming interest for their use in a wide range of fields, including organic light-emitting diodes (OLEDs), petroleum processing, energy conversion, and pollutant removal.[37-53] Nanosized gold materials at different oxidation states, e.g., Au(I), Au(III), and Au(0), have received considerable attention as a new promising class of catalytic systems for green chemical transformations.[54-56] However, the polydispersity issue of bare gold nanoparticles makes it challenging to study structure–reactivity relationships for the gold catalysis. This hinders systematic development of gold nanoparticles for their applications in chemical synthesis. In this regard, extensive efforts have been made for the synthesis of atomically well-defined gold nanoclusters protected by organic ligands. Such particles can provide reliable structural frameworks to pursue the fundamental understanding of heterogeneous catalysis over the gold systems.[57-61]

Recent successes in the preparation of monodispersed gold nanoclusters protected by thiolate ligands, $Au_n(SR)_m$ (–SR represents thiolate ligand, *n* and *m* varied from 15 to 99 and from 14 to 42), raise significant hope to shed light on the long puzzling area of gold catalysis. The atomic precision and monodispersity of the $Au_n(SR)_m$ nanoclusters provide an exciting opportunity to correlate structures of gold systems with their catalytic performance.[57,58,62] Although research on this topic is still in its early stages, the catalytic efficiency and selectivity of such nanoparticles, especially $Au_{25}(SR)_{18}$ nanoclusters (Figure 3.1), have been studied in several reactions including coupling, hydrogenation, oxidation,

etc.[63-68] The non-metallic behavior of the nanoclusters due to the energy quantization arising from their ultrasmall size exerts a strong influence on their catalytic properties.

As shown in Figure 3.1, the $Au_{25}(SR)_{18}$ nanoclusters is composed of six staple shell motifs $Au_2(SR)_3$ ("–SR–Au–SR–Au–SR–") that cover a 13-atom icosahedral core (Au_{13}). Crystal structure of this nanoparticle enables efficient quantum chemistry calculations to understand their catalytic properties. Previous theoretical studies on the $Au_{25}(SR)_{18}$ nanocluster show that the Au_3 sites on the staple motifs (Figure 3.1) are associated with the catalytic behavior of the nanocluster. For instance, density functional theory calculations predict that, in the Sonogashira cross-coupling reaction between phenylacetylene and iodobenzene, both aromatic molecules can be adsorbed on a Au_3 site of the $Au_{25}(SR)_{18}$ nanoclusters.[66]

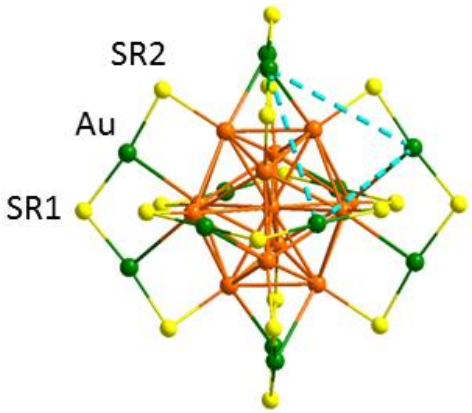

Figure 3.1. Crystal structure of $Au_{25}(SR)_{18}$ (= $Au_{25}(SR1)_6(SR2)_{12}$) nanoclusters indicates two types of thiolate ligands on the staple motif "-(SR2)-Au-(SR1)-Au-(SR2)-". Color code: Au on the staple shell (green); Au in the Au_{13} core (orange); sulfur (yellow). Carbon and hydrogen atoms are not shown for clarity. The triangle shown in a dashed cyan line represents an Au_3 site.

Experimental investigations show the thiolate protected gold nanoclusters require relatively high temperatures (T > 130 ^{o}C) to be activated and function as catalysts.[57,58,70-72] This makes it difficult for applications of the catalysts in a wide range of systems which require to be maintained at low temperatures. Thus it is highly valuable and desirable to activate the catalysts at lower temperature with the help of some promoters. Lewis-acids, in particular, transition-metal ions M^{z+}, such as Cu^{+}, Cu^{2+}, Ni^{2+}, and Co^{2+}, are known for their promotional effect on Au nanoparticle-catalyzed reactions. However, the mechanism for the promotion is poorly understood.[73-75] For example, the presence of Co^{2+} is shown to improve the hydrogenation rate and allylic alcohol chemoselectivity for the chemoselective hydrogenation of α,β-unsaturated carbonyl compounds, catalyzed by PVP-protected Au^{0} nanoparticles (PVP = polyvinylpyrrolidone).

Systematic development of catalytic systems to function at relatively *low temperatures* requires molecular understanding of activation mechanisms of the gold nanoclusters in the presence of chemical promoters. In this chapter, computational tools are applied to study the Lewis-acid-promoted hydrogenation of aldehyde to alcohol catalyzed by $Au_{25}(SR)_{18}$ (hereafter, SR = SC_2H_4Ph) in the presence of a base (NH_3) and H_2. Using DFT calculations, it is rationalized that $Au_{25}(SR)_{18}$ nanoclusters can undergo fragmentation in the presence of a Lewis-acid, resulting in the formation of $Au_{25-n}(SR)_{18-n}$ species with catalytic active sites for the aldehyde-to-alcohol hydrogenation. Possible configurations of $Au_{24}(SR)_{17}$ are examined using DFT and time-dependent DFT (TD-DFT) methods. Our calculations indicate that the catalytic active site located on the Au_{13}-core of $Au_{25-n}(SR)_{18-n}$ is capable of activating the covalent bond of H_2 heterolytically. To our

knowledge, this is the first study that proposes the catalytic activity of the nanoclusters are associated with exposed Au_{13}-core rather than the intact nanoclusters.

Further, potential activation of the god nanoclusters in the presence of imidazolium-based ionic liquids (ILs) is studied. DFT calculations indicate that the acidic proton at the position-2 of the imidazolium ions can play an important role in the detachment of -SR ligands and Au atoms from the nanocluster surface for generation of $Au_{25-n}(SR)_{18-n}$. This in turn exposes the Au_{13}-core of the nanoclusters for catalytic reactions.

Finally, electronic and catalytic properties of aromatic-thiolate-protected gold nanocluster are investigated. Results indicate the catalytic activity and selectivity of the $Au_{25}(SR)_{18}$ nanoclusters in reactions can be largely enhanced by the aromatic nature of the thiolate ligands.

3.3 Computational Method

3.3.1 A) Au_{25} Nanoclusters with Lewis-Acids for Aldehyde Hydrogenation. DFT optimization was performed using the B3PW91 hybrid density functional. The 6-31G** basis set was employed for H, C, N, O and S,[76-79] while the valence aug-cc-pVDZ basis set together with the appropriate Stuttgart-Dresden effective core potentials (ECPs) was used for transition metal ions, Cu^{+}, Cu^{2+}, Ni^{2+}, and Co^{2+}.[80-82] For gold atoms, the LANL2DZ basis set was used.[83] The B3PW91 functional with the LANL2DZ basis set has been shown to predict accurately the structure of Au nanoclusters.[84-87] The reaction energy is determined as the energy difference $\Delta E = \Sigma E_{pro} - \Sigma E_{rea}$, where ΣE_{pro} and ΣE_{rea} are total energies of the products and reactants, respectively. The integral equation formalism polarizable continuum model (IEFPCM) was applied to study the solvation effect on

reaction energetics.[88] TD-DFT calculations of optical absorption spectra were also performed and compared with experimental UV-Vis results. All calculations were carried out with the Gaussian09 package.[79] The crystal structure of $Au_{25}(SR)_{18}$ was employed as a starting point for DFT calculations for nanoclusters.[89]

3.3.2 B) Au_{25} Nanoclusters with ILs for the Suzuki Cross Coupling Reaction. DFT calculations were performed to investigate oxidative addition of $Au_{25}(SCH_3)_{18}$ to a halide. All ground state geometry optimizations were carried out with the B3PW91 hybrid density functional and 6-31G(d,p) (H, C, N, O, S) and LANL2DZ (Au and I) basis sets.[76-79,83] We have also used MIDI! basis set for I to examine the effect of basis sets on the iodine-incorporated structures.[90] The integral equation formalism polarizable continuum model (IEFPCM) was applied to study how solvation may influence the stabilization of a complex formed by a removed thiolate ligand and DMI (1,3-Dimethylimidazolium), EtOH, or DMF.[88] All calculations were carried out with the Gaussian 09 package.[79]

Solvation structure of BMIM·BF_4 in ethanol was studied via MD. Four different IL concentrations, 0.083, 0.057, 0.029, 0.014 M, were considered. The number of ethanol molecules in the simulation system was 500 in all cases. At each IL concentration, energy optimization, annealing from 800 K to 363 K and equilibration for 2 ns were first conducted, followed by a 10 ns production run in the *NPT* ensemble at 1 *atm* and 363 K. All simulations were performed using the NAMD package.[91] The Langevin dynamics and Nose-Hoover Langevin piston methods were used to keep the temperature and pressure constant, respectively.[92] The particle mesh Ewald (PME) algorithm was used to calculate the long-range electrostatic interactions.[93] The van der Waals forces were truncated using

a cutoff of 12 Å. The all-atom potential model based on OPLS-AA parameters was employed to compute intermolecular forces.[94,95]

3.3.3 C) Au_{25} Nanoclusters Protected with Aromatic and Aliphatic Ligands. DFT optimization and TD-DFT calculations of optical absorption spectra of nanoclusters were carried out using Gaussian09 package and TPSS functional.[79] The basis sets 6-31G** were employed for H, C, and S.[76-79] For gold atom, the LANL2DZ basis set was used.[83] To investigate the proposed reaction mechanisms, Quantum Espresso package was used.[96] The Projector Augmented-Wave (PAW) method was applied to describe the interaction between the electrons and nuclei.[97] The Perdew–Burke–Ernzerhof (PBE) form of the generalized gradient approximation was employed for electron exchange and correlation.[98] The gold cluster was placed at the center of a cubic box of 25.0 Å × 25.0 Å × 25.0 Å. The kinetic energy cutoff was chosen to be 450 eV and integration in the reciprocal space was carried out at the Γ k-point of the Brillouin zone.

3.4 Results and Discussions

3.4.1 A) Au_{25} Nanoclusters with Lewis-Acids for Aldehyde Hydrogenation

Extensive studies on bare gold clusters with no ligands attached have revealed that low-coordinated naked gold atoms on the surface are the main active sites for catalytic reactions. According to recent studies, however, their catalytic activity diminishes when they are protected by ligands, such as thiolate –SR groups.[99,100] This raises an important question as to the nature of the active sites for reactions catalyzed by thiolate protected gold nanoclusters, which is the main focus of this section.

As a case study, the catalytic activity of $Au_{25}(SR)_{18}$ nanoclusters is investigated for hydrogenation reaction of aldehydes for synthesis of alcohol. The small size and crystal structure of the $Au_{25}(SR)_{18}$ nanoclusters enable efficient and accurate electronic structure calculations.[89] This allows quantitative comparison of theoretical predictions with experiments without introducing any simple approximate model descriptions to study reaction mechanisms, such as the adsorption of reactant molecules onto the nanocluster surface. Thus, small and atomically-precise nanoclusters provide an excellent molecular system to investigate catalytic mechanisms and to understand relationships between the structure and catalytic properties of catalysts in, e.g., aldehydes hydrogenation.

We first investigate possible active sites on $Au_{25}(SCH_3)_{18}$, as a model of the $Au_{25}(SCH_2CH_2Ph)_{18}$ nanocluster, for the adsorption of reactants, i.e., benzaldehyde and H_2 as a reducing agent. DFT predicts that gold atoms of the nanoclusters do not interact strongly with the reactants, in agreement with previous theoretical studies on related reaction systems.[72,99,100] This result shows the inert nature of the protected $Au_{25}(SCH_3)_{18}$ cluster toward the adsorption of the reactants and subsequent hydrogenation of aldehydes. In this context, it is hypothesized that the gold nanoclusters are subject to some structural changes induced by high reaction temperature or the presence of chemical promoters. To provide low-coordinated naked gold atoms on the surface of the nanocluster, a mechanism based on the removal of thiolate groups would be prudent to consider. To test this, our experimental collaborators in Prof. Jin's research group, performed the Lewis-acid-promoted hydrogenation of aldehyde to alcohol catalyzed by $Au_{25}(SR)_{18}/CeO_2$ (hereafter, SR = SC_2H_4Ph) in the presence of a base (pyridine or $NH_3 \cdot H_2O$) under mild conditions (18 bar H_2 at 323K).[63]

The experimental results, provided by Prof. Jin's research group, are given in Table 3.1.[63] Frist, we note that $Au_{25}(SR)_{18}/CeO_2$ catalyst gives a very low conversion at 323 K in the absence of Lewis-acid (13.4%, Table 3.1, entry 1), although it reaches to ~93% if the temperature is raised up to 353K. Second, the conversion improves markedly to 90.1% if Co^{2+} is added to the reaction medium (Table 3.1, entry 2). The degree of promotion of the catalytic activity of $Au_{25}(SR)_{18}/CeO_2$ by other transition metal ions is found to be in the order $Co^{2+} > Ni^{2+} \approx Cr^{3+} > Cu^{+} > Cu^{2+}$. It is worthwhile to note that no conversion was detected if the nanoclusters are absent and only Lewis-acid and CeO_2 oxide are present (Table 3.1, entries 12-15). This confirms that catalytic activity arises from the gold nanoclusters. Using UV-vis spectroscopy in conjunction with MALDI and ESI mass spectrometry, Prof. Jin's research group found that $Au_{25}(SR)_{18}$ nanoclusters undergo fragmentation in the presence of the Lewis-acids, resulting in the formation of $Au_{25-n}(SR)_{18-n}$ (n = 1–4) species (Figures 3.2 and 3.3).[63]

The mass spectrometry results as well as the data in Table 3.1 suggest that the catalytic activity is associated with the newly generated $Au_{25-n}(SR)_{18-n}$ species such as $Au_{24}(SR)_{17}$. This means that Lewis-acids may be not only directly involved in the hydrogenation reaction, but also responsible for the generation of $Au_{24}(SR)_{17}$ species with active sites for catalysis. As a consequence, a better adsorption of Lewis-acids onto the nanoclusters and/or a faster generation of $Au_{24}(SR)_{17}$ would lead to a higher promotion of the hydrogenation reaction (e.g., $Co^{2+} > Cu^{2+}$). In what follows, it is considered in detail the structure of $Au_{24}(SR)_{17}$, its production pathways from the parent $Au_{25}(SR)_{18}$ nanoclusters in the presence of a Lewis-acid and a base, and potential mechanisms for ensuing hydrogenation reactions.

Table 3.1. Influence of different Lewis acids ($M^{z+}X_z$) on the chemoselective hydrogenation of 4-nitrobenzaldehyde (**1**) to 4-nitrobenzyl alcohol (**2**) catalyzed by $Au_{25}(SR)_{18}/CeO_2$.[a, 63]

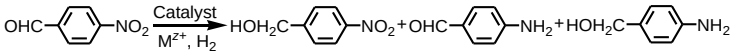

1 **2** **3** **4**

Entry	Catalyst	M^{z+}	Conv. [%][b]	Selectivity [%][b]		
				2	**3**	**4**
1	$Au_{25}(SR)_{18}$	-	13.4	~100	-	-
2	$Au_{25}(SR)_{18}$	$Co(OAc)_2$	90.1	~100	-	-
3	$Au_{25}(SR)_{18}$	$Cr(NO_3)_3$	75.8	~100	-	-
4	$Au_{25}(SR)_{18}$	$NiCl_2$	78.2	~100	-	-
5	$Au_{25}(SR)_{18}$	$Cu(OAc)_1$	61.1	~100	-	-
6	$Au_{25}(SR)_{18}$	$Cu(OAc)_2$	50.0	~100	-	-
7	$Au_{25}(SR)_{18}$	$Cu(NO_3)_2$	50.8	~100	-	-
8	$Au_{25}(SR)_{18}$	$CoCl_2$	90.8	~100	-	-
9	$Au_{25}(SR)_{18}$[c]	$Co(OAc)_2$	82.5	>99.5		-
10	$[Au_{25}Co]$[d]	-	87.3	~100	-	-
11	$[Au_{25}Co]$[e]	-	88.4	~100	-	-
12	none	$Co(OAc)_2$	n.r.	-	-	-
13	none	$Cr(NO_3)_3$	n.r.	-	-	-
14	none	$NiCl_2$	n.r.	-	-	-
15	none	$Cu(OAc)_2$	n.r.	-	-	-
16	$Au_{25}(SR)_{18}$[f]	$Co(OAc)_2$	~100	~100	-	-

[a]Reaction conditions: 100 mg $Au_{25}(SR)_{18}/CeO_2$ catalyst (~1 wt% $Au_{25}(SR)_{18}$ loading) in 1 mL water, $M^{z+}/Au_{25}(SR)_{18}$ = 2:1 (mol/mol), 0.1 mmol 4-nitrobenzaldehyde, 5 μL pyridine, 18 bar H_2 at 323K, 10 hrs. [b]The conversion (conv.) of 4-nitrobenzaldehyde and selectivity were determined by ^{1}H NMR spectrum. n.r. = no reaction. [c]Reaction conditions: 4 g $Au_{25}(SR)_{18}/CeO_2$ catalyst (~ 40 mg $Au_{25}(SR)_{18}$ loading) in 30 mL water, 1.05 mmol $Co(OAc)_2$, 5 mmol 4-nitrobenzaldehyde, 300 μL pyridine, 18 bar H_2 at 323K, 10 hrs. [d]2nd and [e] 3rd reuses of the catalyst recovered from entry 2. [c,d]No M^{z+} was added to the reaction system. [f]For entry 16, NH_3 is used instead of pyridine.

3.4.1.1 Structure of $Au_{24}(SR)_{17}$ species. There are three non-equivalent Au-SR pairs on the $Au_{25}(SR)_{18}$ nanoclusters[89] (denoted as Au_{25} NC in Figure 3.4A) that can be removed upon exposure to Lewis-acids: two different pairings of Au of a "–SR–Au–SR–" staple

motif with –SR (i.e., α and β fragments), and one for Au of the Au_{13}-core (γ pairing). Since the removal of a γ unit from the Au_{13}-core is likely to induce strong disruptions of Au_{25} NC's structure and characteristics (e.g., cluster re-arrangement and major electronic property changes), we consider here only the removal of fragments α and β that results in the formation of new species Au_{24} NC-1 (Figure 3.4B) and Au_{24} NC-2 (Figure 3.4C), respectively. DFT predicts that the optimized $Au_{24}(SCH_3)_{17}^-$ structure of Au_{24} NC-1 is more stable than that of Au_{24} NC-2 by 21.2 kcal/mol. This is in good agreement with previous studies[89,101,102] and also with our Au–S bond length results (Table 3.2).

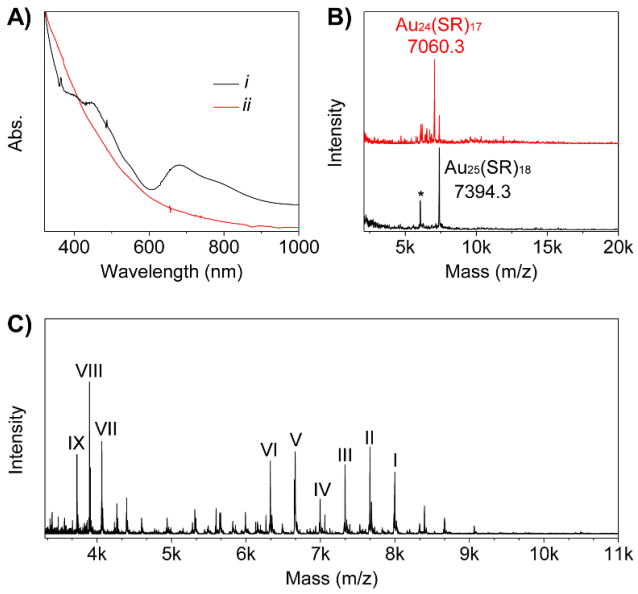

Figure 3.2. (A) UV-vis and (B) MALDI mass spectra of $Au_{25}(SR)_{18}$ nanoclusters at room temperature stirring for 10h in a mixed dichloromethane/methanol solution: *i*) in the presence of only ammonia (black line), and *ii*) in the presence of $Co(OAc)_2$ (Co^{2+}:$Au_{25}(SR)_{18}$ = 2:1, mol/mol) and ammonia (red line). The peak marked with an asterisk (*) is the fragment $Au_{21}(SR)_{14}$ caused by MALDI, rather than an impurity. (C) Positive mode ESI mass spectrum of $Au_{25}(SR)_{18}$ nanoclusters in the presence of $Co(OAc)_2$ (Co^{2+}:$Au_{25}(SR)_{18}$ = 2:1, mol/mol) and pyridine.[63]

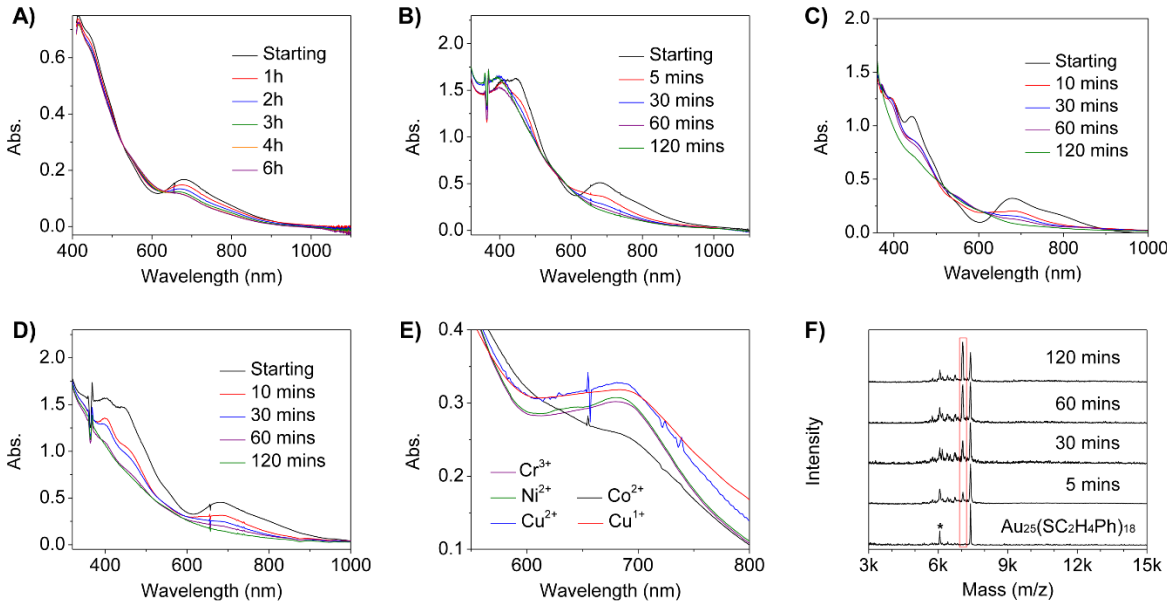

Figure 3.3. UV-vis spectra tracing of a methanol solution of $Au_{25}(SR)_{18}$ nanoclusters in the presence of (A) only $Co(OAc)_2$, (B) $Co(OAc)_2$ and ammonia, (C) $NiCl_2$ and ammonia, and (D) $Cu(OAc)_2$ and ammonia. (E) UV-vis spectra of $Au_{25}(SR)_{18}$ with $M^{z+}X_z$ at 10 mins (and at 5 mins in the case of $Co(OAc)_2$). (F) MALDI mass spectra of the $Au_{25}(SR)_{18}$ nanoclusters in the presence of $Cu(OAc)_2$ and ammonia. In all cases, M^{z+}:$Au_{25}(SR)_{18}$ = 2:1 (mol/mol). In (F), the peak marked with an asterisk (*) is a fragment caused by MALDI, rather than an impurity.[63]

The calculated optical absorption spectra of Au_{25} NC, Au_{24} NC-1, and Au_{24} NC-2 are shown in Figure 3.4. We considered only the two lowest absorption bands. The maximum intensity lines of these absorption bands of Au_{25} NC are located at 1.72 eV (720 nm) and 2.74 eV (452 nm), consonant with measurements (1.80 and 2.75 eV).[89] Perhaps the most salient aspect of our results is that that the lowest absorption band nearly disappears for Au_{24} NC-1, while it remains as a shoulder in the case of Au_{24} NC-2 (Figure 3.4). The calculated spectrum of Au_{24} NC-1 agrees well with the experimental UV-vis results in Figure 3.3A-C. It is also possible that the absence of specific band structures in the UV−vis spectra is due to the presence of different complexes. However, in view of TD-DFT as well

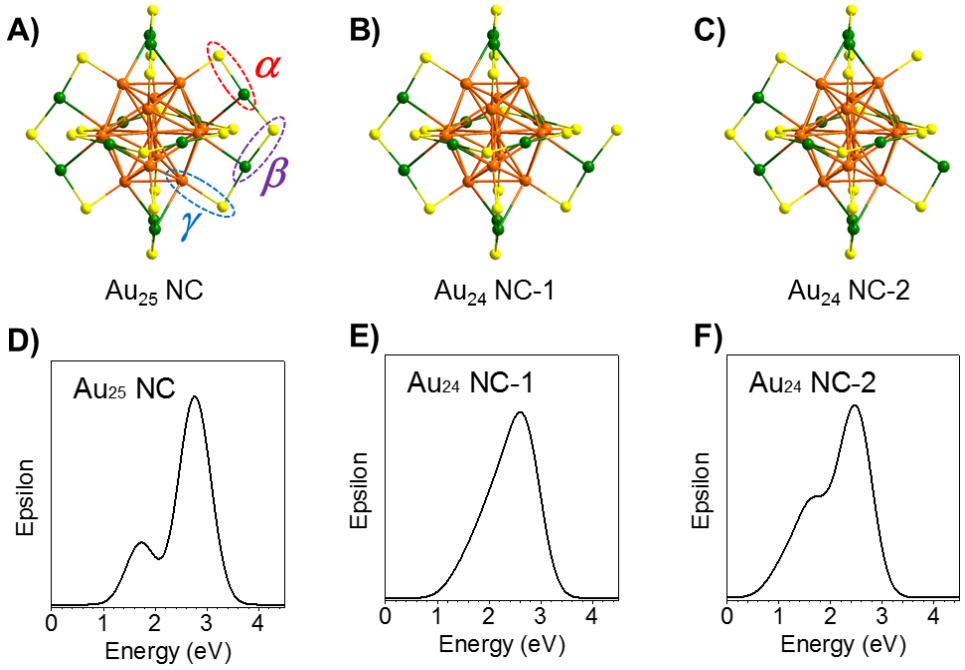

Figure 3.4. (A) Framework of $Au_{25}(SR)_{18}$ nanoclusters (Au_{25} NC) based on the results of Ref 10 and three different "–Au–SR–" fragments (denoted as Au-S: α, β, γ) for possible removal. Detachment of fragments α and β results in $Au_{24}(SR)_{17}$ with configurations (B) Au_{24} NC-1 and (C) Au_{24} NC-2, respectively. Theoretical absorption spectra of $Au_{25}(SCH_3)_{18}^-$ (Au25 NC) and $Au_{24}(SCH_3)_{17}^-$ in configurations Au24 NC-1 and Au24 NC-2 are presented in (D), (E) and (F), respectively. Color code: green, Au on the staple shell; orange, Au atoms in the Au_{13} core; yellow, sulfur atoms. Other atoms are not shown for clarity.

Table 3.2. Average Au-S bond lengths in the $[Au_{25}(SR)_{18}]^-$ nanoclusters.

Entry	Au-S Bond	Average length (Å	Range (Å)	Difference
1	α	2.315	2.303 to 2.33	-
2	β	2.308	2.300 to 2.31	-3.0%
3	γ	2.371	2.362 to 2.38	24.2%

Bond length difference is calculated using the Au-S:α as the reference.

as the DFT results for the relative stability above, we believe the structure of the $Au_{24}SR_{17}$ species generated in the solution of Lewis-acids is mainly characterized by Au_{24} NC-1 in Figure 3.4B.

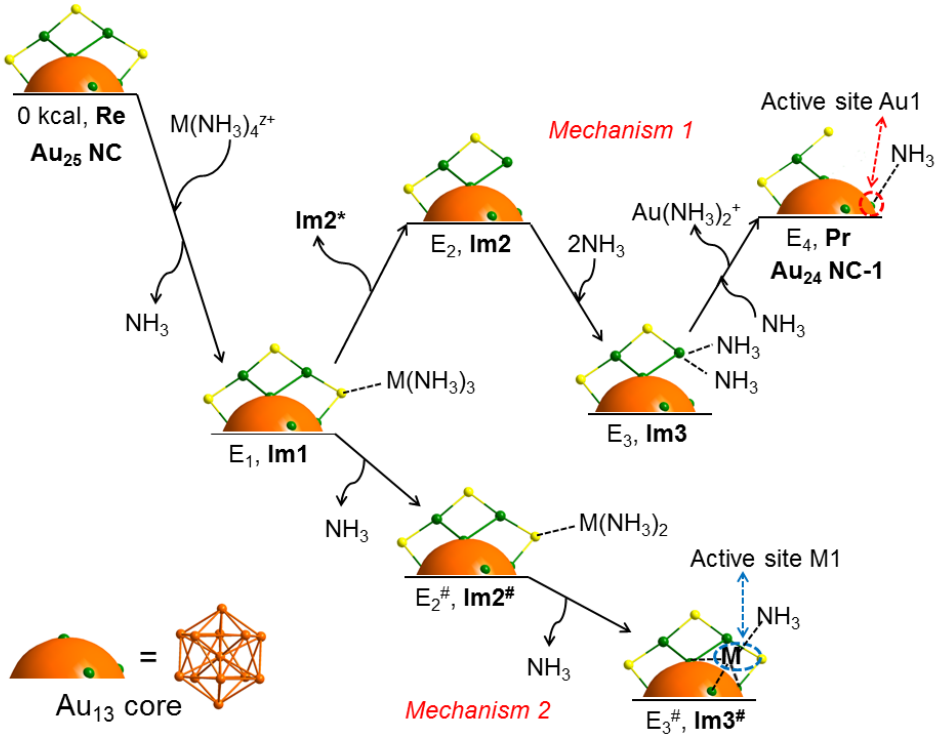

Figure 3.5. Proposed mechanisms for speciation of $Au_{24}(SR)_{17}$ (*Mechanism 1*) and formation of adduct $[\text{nanoparticle-M}]^{(z-1)+}$ (*Mechanism 2*) in the presence of M^{z+} salt and ammonia. A gold atom (Au1) from the Au_{13}-core becomes exposed to the solvent in *Mechanism 1* (upper pathway), while the transition metal ion at M1 becomes an active site in *Mechanism 2* (lower pathway). The calculated energies for different steps are given in Table 3.3. Color code: Au, green; S, yellow. The orange section represents the Au_{13} core and Im2* denotes $[M(NH_3)_3SCH_3]^{(z-1)+}$.

3.4.1.2 Mechanism of $Au_{24}(SR)_{17}$ generation. To rationalize the removal mechanism of a "–Au–SR–" pair unit from the $Au_{25}(SCH_3)_{18}^-$ nanoclusters, we investigated possible adsorption sites of a Lewis-acid (M^{z+} ion) on $Au_{25}(SCH_3)_{18}^-$ using the DFT method. We considered Cu^+, Cu^{2+}, Ni^{2+}, and Co^{2+} for M^{z+} in the calculations. In *Mechanism 1* (upper

pathway in Figure 3.5), the sulfur atom of unit *α* (Figure 3.4) forms a bond with M^{z+} (Re → Im1). This adsorption process is energetically exothermic in the gas phase by 66.9, 197.6, 188.0, and 183.6 kcal/mol with M^{+}–S bond length 2.29, 2.30, 2.36 and 2.45 Å for Cu^{+}, Cu^{2+}, Ni^{2+}, and Co^{2+}, respectively (Table 3.3). In aqueous solution, the exothermicity

Table 3.3. DFT results for energies (kcal/mol) for elementary steps of *Mechanism 1 and 2* in Figure 3.4. Solution-phase energetics estimated using the IEFPCM and Born solvation free energies are given in parentheses. All energy values are relative to the reactant state Re.

	Cu^{+}	Cu^{2+}	Ni^{2+}	Co^{2+}
$E_1 = \Delta E$(**Re → Im1**)	-66.9	-197.6	-188.0	-183.6
ΔE(**Im1 → Im2**)	+60.2	+69.9	+55.2	+42.5
ΔE(**Im2 → Im3**)	-20.8 (~ -14)	-20.8 (~ -14)	-20.8 (~ -14)	-20.8 (~ -14)
ΔE(**Im3 → Pr**)	+64.1 (~ 0)	+64.1 (~ 0)	+64.1 (~ 0)	+64.1 (~ 0)
E_2	-6.7 (~ +25)	-127.7 (~ +15)	-132.8 (~ +14)	-141.1 (~ +18)
E_3	-27.5 (~ +11)	-148.5 (~ +1)	-153.6 (~ 0)	-161.9 (~ +4)
E_4	+36.6 (~ +11)	-84.4 (~ +1)	-89.5 (~ 0)	-97.8 (~ +4)
$E_2^{\#}$	-59.3	-	-	-
$E_3^{\#}$	-65.5	-	-	-

Table 3.4. Stabilization energy (in kcal/mol) of different species in solution with respect to the gas phase. For the charged nanocluster NP^{-1}, the Born solvation free energy, $\frac{1}{2}(1-1/\varepsilon)e^2/a$, was employed with the cluster diameter $2a \approx 25$ Å and solvent dielectric constant $\varepsilon = 80$ (e = elementary charge).

$[Cu(NH_3)_4]^{+}$	-52.4	$[Ni(NH_3)_3SCH_3]^{2+}$	-69.5
$[Cu(NH_3)_4]^{2+}$	-198.4	$[Co(NH_3)_3SCH_3]^{2+}$	-68.0
$[Ni(NH_3)_4]^{2+}$	-207.2	$[Au(NH_3)_2]^{+}$	-55.5
$[Co(NH_3)_4]^{2+}$	-217.2	NP^{-1}	-13.0
$[Cu(NH_3)_3SCH_3]$	-28.6	NP^{-2}	-52.0
$[Cu(NH_3)_3SCH_3]^{2+}$	-65.5	NH_4^{+}	-72.6
$PhCHOH^{+}$	-50.5	$PhCH_2OH$	-4.4
		NH_3	-3.7

is expected to decrease due to the solvation stabilization of the charged reactants. For insight into solvation effects, the IEFPCM results for solution-phase energetics are given in Tables 3.3 and 3.4. For clarity, we mention that the coordination number (*CN*) was assumed to be 4 for the isolated metal complex, i.e., $M(NH_3)_4^{z+}$, and one of the four NH_3 moieties was assumed to be displaced from the coordination shell as the complex attaches itself to the cluster. As a result, the Lewis-acid (M^{z+} ion) adsorbed on the cluster surface is coordinated to three NH_3 molecules. Though we do not exclude possibilities of *CN* higher or lower than 4 for the isolated metal complex, our results for *CN* = 4 clearly show that a considerable amount of energy is released with the formation of a M^{z+}–S bond. This excess energy can facilitate the removal of the entire M^{z+}–S moiety (Im2*), i.e., thiolate group plus metal complex, from the gold nanocluster and thus the formation of $Au_{25}(SCH_3)_{17}$ (Im1 → Im2). The removal of M^{z+}–S is an endothermic process with ΔE = +60.2, +69.9, +55.2, and +42.5 kcal/mol for Cu^+, Cu^{2+}, Ni^{2+}, and Co^{2+}, respectively. We parenthetically note that ΔE for Im1 → Im2 in the gas phase decreases in the order $Cu^{2+} > Cu^+ > Ni^{2+} > Co^{2+}$, in concert with the experimental trend of the conversion rate of hydrogenation (Table 3.1). One potential explanation is that the thiolate group removal is a key step of the hydrogenation reaction. The resulting nanoclusters $Au_{25}(SCH_3)_{17}$ have a gold atom that is bonded to only one thiolate group. Two ammonia (NH_3) molecules can coordinate to this gold atom exothermically with the Au-N distance of 2.39 Å and energy release of 20.8 kcal/mol (Im2 → Im3). The coordinating NH_3 molecules eventually detach the gold atom from the nanocluster, resulting in the formation of $Au(NH_3)_2^+$ and $Au_{24}(SCH_3)_{17}^-$ (Im3 → Pr, Figure 3.5). While the final step is endothermic by +64.1 kcal/mol in the gas phase, endothermicity becomes negligible in aqueous solutions because of significant solvation

stabilization of the charged products. The overall reaction of the inorganic complex with the gold nanoclusters based on *Mechanism 1* can be written as:

$$[Au_{25}(SCH_3)_{18}]^- + M(NH_3)_4^{z+} + NH_3 \rightarrow [Au_{24}(SCH_3)_{17}]^- + [M(NH_3)_3(SCH_3)]^{(z-1)+} + Au(NH_3)_2^+$$

with ΔE= +36.6, -84.4, -89.5, and -97.8 kcal/mol (gas-phase) and ~11, ~1, ~0 and ~4 kcal/mol (solution-phase) for Cu^+, Cu^{2+}, Ni^{2+}, and Co^{2+}, respectively.

Mechanism 1 proposed here explains our experimental finding that the presence of base $NH_3 \cdot H_2O$ accelerates the disappearance of the absorption band at ~670 nm (Figure 3.3A *vs.* 3.3B). NH_3 is usually a better lone-pair donor than CH_3OH to coordinate and form a complex with Au. Similarly, it can also explain another experimental finding above, i.e., NH_3 leads to a higher conversion than pyridine (see Hydrogenation mechanism below), in that NH_3 is a better lone-pair donor than pyridine to coordinate to gold.

We briefly pause here for perspective. While our DFT results indicate that Au_{24} NC-1 (Figure 3.4B) is the dominant configuration of $Au_{24}SR_{17}$ species generated in the solution of Lewis acids, the effect of the CeO_2 support was not accounted for in the calculations. CeO_2 can play a crucial role to, for example, rearrange the structure of the nanoparticles and change the active sites. Therefore, even if the direct generation of Au_{24} NC-2 from its parent Au_{25} NC via removal of a β unit may be suppressed (see Figure 3.4 above), it can be produced from Au_{24} NC-1 via, e.g., ligand exchange on the support. The formation of Au_{24} NC-2 yields an active gold site (Au2) on a staple motif rather than on the core (Figure 3.6).

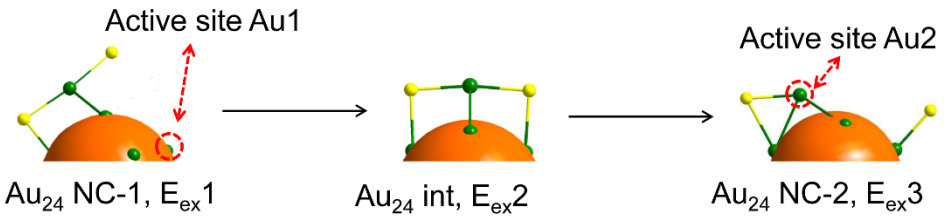

Figure 3.6. Ligand exchange mechanism to from Au_{24} NC-1 with a cationic active site (Au2) from Au_{24} NC-2. Relative to $E_{ex}1$, $E_{ex}2$ = 0.9 and $E_{ex}3$ = 20.3 kcal/mol.

3.4.1.3 Mechanism of the adduct [nanoparticle-M]$^{(z-1)+}$ formation. In *Mechanism 2*, i.e., lower pathway in Figure 3.5, a considerable energy release via M^{z+}–S bond formation (Re → Im1) can result in the removal of coordinating ammonia molecules (Im1 → Im2$^{\#}$ → Im3$^{\#}$) rather than the interacting thiolate group. ΔE for Im1 → Im2$^{\#}$ and Im2$^{\#}$→ Im3$^{\#}$ steps are +7.6 and -6.2 kcal/mol, respectively, for M^{z+} = Cu^{+}. As illustrated in Figure 3.5, M^{z+} becomes adsorbed on the Au_{13}-core surface by coordinating to three core Au atoms (Im3$^{\#}$). This in turn can induce a considerable elongation (0.05 Å) of nearby Au-S bonds, exposing their thiolate groups even more to the Lewis-acids in the solvent. Therefore, it is also possible that Im3$^{\#}$ follows the pathway of *Mechanism 1* discussed above, i.e., Im3$^{\#}$ → Im2 → Im3 → Pr, by losing one of the "–Au–SR–" pair units.

The net charge of Au_{25} NC in the present study was -1. Since the charge state of nanoclusters can modulate their solvation energy and spin multiplicity, it could exert a considerable influence on reaction kinetics and thermodynamics of the Au-SR removal (*Mechanism 1*) and/or adduct formation (*Mechanism 2*). For example, we expect that the solvation effect on overall reaction thermodynamics of the adduct formation would vary significantly with the charge state because the reactant and product nanocluster states, i.e., Au_{25} NC and Im3$^{\#}$ of *Mechanism 2*, are characterized by different electric charges. By

contrast, in the case of *Mechanism 1*, the corresponding change of the solvation effect with the charge state would not be as significant because Au_{25} NC and Au_{24} NC-1 have the same charge. It would thus be both interesting and worthwhile to study in the future how the charge state of nanoclusters influences their catalytic activity in hydrogenation reactions.

3.4.1.4 Hydrogenation mechanism. Since essentially all surface gold atoms of $Au_{25}(SC_2H_4Ph)_{18}^-$ are protected by thiolate groups, the Au_{25} NC nanoclusters are inert toward adsorption of non-radical molecules on their surface. Our calculations indeed show that there are no strong interactions of $Au_{25}(SCH_3)_{18}^-$ with possible adsorbates (e.g., PhCHO, NH_3, and H_2), in accordance with recent theoretical studies.[99,100] However, the removal of an Au-SR fragment or the formation of an adduct exposes open metal atoms (a gold atom of the core Au_{13}, staple shell, or the Lewis acids) to the solvent (Figures 3.5 and 3-6). DFT predicts that these sites, i.e., Au1, Au2, and M1 in Figures 3.5 and 3.6, are active towards adsorption of reactants. In view of these results, we propose hydrogenation mechanisms (Figure 3.7), in which bond activation of H_2 on these metal sites is the first step.

Upon removal of the capping NH_3 from the metal site (Au1 or M1), the H–H bond of a H_2 molecule becomes activated with the aid of a base (Figure 3.7). Specifically, the base (NH_3) abstracts a proton from H_2 to form NH_4^+ with H^- on the active metal site ($Re^{*Au1} \rightarrow Im1^{*Au1}$, $Re^{*M} \rightarrow Im1^{*M}$, $Re^{*Au2} \rightarrow Im1^{*Au2}$). The removal of capping NH_3 and adsorption of a H_2---NH3 unit are endothermic and exothermic, respectively. Overall, this two-step process at the Au1 and M1 active sites is endothermic by +4.9 and +19.7 kcal/mol, respectively. For the case of Au2, this step is found to be exothermic by -3.5 kcal/mol. In a polar solvent like water, however, the product state would become considerably stabilized

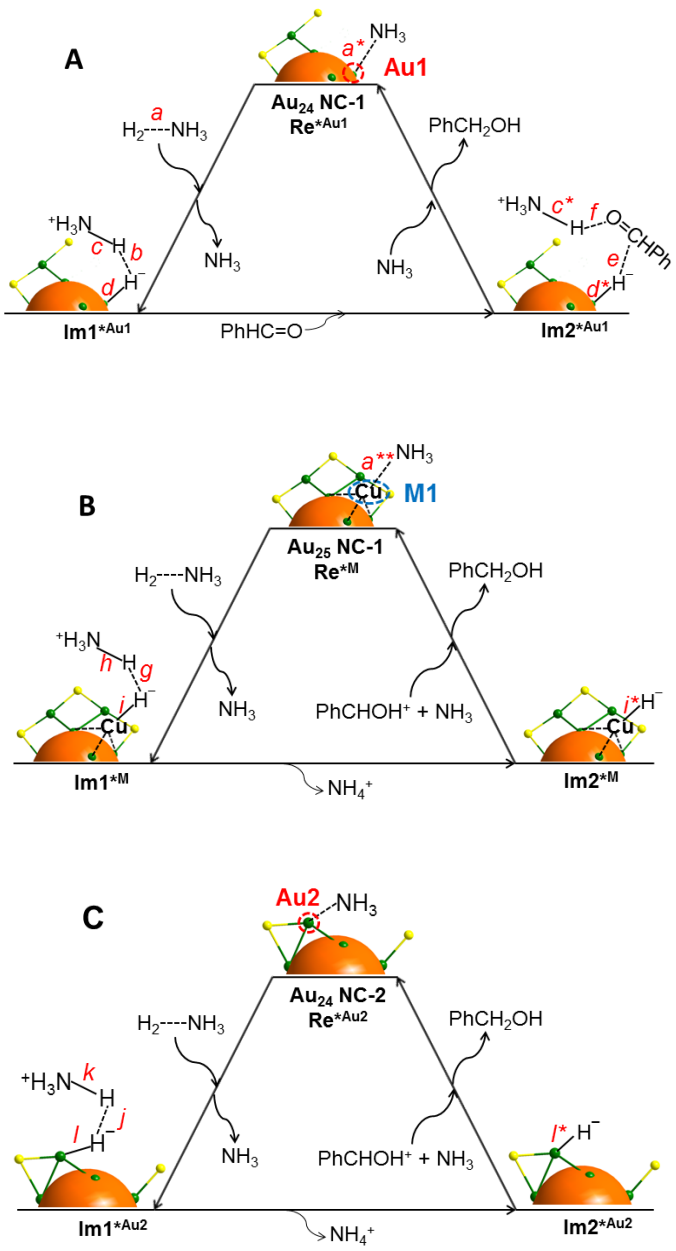

Figure 3.7. Proposed mechanism for hydrogenation of benzaldehyde in the presence of H_2 and NH_3 on **(A)** site Au1, **(B)** site M1, and **(C)** site Au2. The values of inter-atomic distances are: *a** = 2.26, *a* = 2.56, *b* = 1.82, *c* = 1.05, *d* = 1.64, *c** = 1.03, *d** = 1.63, *e* = 2.85, *f* = 1.87, *a*** = 2.03, *g* = 0.80, *h*= 2.04, *i* = 1.74, *i** = 1.53, *j* = 1.73, *k* = 1.04, *l*= 1.61, and *l** = 1.59 Å. (For comparison, the equilibrium bond length of an isolated H_2 molecule is 0.74 Å.) The same color code is used as in Figure 3.5.

compared to the reactant because of the highly charge-separated nature of the $NH_4^+ \ldots H^-$ moiety. DFT calculations indicate that the presence of a base, such as NH_3, is crucial for the activation of H_2. Without a base, the interaction of H_2 with M1 and Au2 is mainly physical and that with Au1 is rather weak, so that H_2 tends to stay away from Au1. Thus a base is needed for chemical adsorption of H_2 and ensuing H–H bond activation on Au1 and M1. This participation of a base in the H_2 activation as well as in the removal of a gold atom discussed above (*Mechanism 1*) provides a theoretical explanation for experimental findings that no hydrogenation reaction occurred in the absence of a base and that a stronger base (NH_3 vs. pyridine, Table 3.1, entry 16) yields a higher conversion efficiency. Of note, the lone-pair on nitrogen is in sp^3 and sp^2 orbitals in the cases of NH_3 and pyridine, respectively. In the case of the Au1 active site, PhCHO becomes physically adsorbed on the surface of the nanoclusters via interactions of its O and C (-CHO group) with NH_4^+ and H^-, respectively, in an exothermic step with ΔE = -5.3 kcal/mol ($Im1*^{Au1} \rightarrow Im2*^{Au1}$, Figure 3.7A). Finally, H^+ (of NH_4^+) and H^- will transfer to PhCHO and produce $PhCH_2OH$ exorthemically with energy release of 15.4 kcal/mol ($Im2*^{Au1} \rightarrow Re*^{Au1}$, Figure 3.7A).

In the case of hydrogenation catalyzed by the M1 and Au2 sites (Figure 3.7B and 3.7C), the ammonium ion formed ($Im1*^{M}$ and $Im1*^{Au2}$) may become solvated in the reaction media and act as a donor for protonation of aldehyde ($Im1*^{M} \rightarrow Im2*^{M}$ and $Im1*^{Au2} \rightarrow Im2*^{Au2}$). For M1 and Au2, respectively, this step is found to be endothermic by +26.0 and +46.8 kcal/mol in water, while it is +111.6 and +158.4 kcal/mol in the gas phase. Since the products, NH_4^+, $Au_{25}SR_{18}CuH^-$, and $Au_{24}SR_{17}H^{2-}$ are charged, they are strongly stabilized in water, compared to the gas phase (see Table 3.4). This means that solvation can facilitate (or even induce) the elongation of the H—H bond (*g* in Figure 3.7B)

to produce charged species (NH_4^+ and H^-). This is followed by the reduction of protonated benzaldehyde to benzyl alcohol ($Im2^{*M} \rightarrow Re^{*M}$ and $Im2^{*Au2} \rightarrow Re^{*Au2}$, Figure 3.7B and 3-7C). This final reduction step is exothermic with ΔE = -152.1 and -175.6 kcal/mol in the gas phase, while -89.3 and -86.8 kcal/mol in the solution phases, respectively, for the cases of M1 and Au2 sites.

We briefly pause here for perspective. DFT results indicate that the surface gold atoms on the Au_{13}-core or staple shell, or the Lewis acids bound on the Au_{13}-core can provide catalytic active sites for hydrogenation. Despite the significant effect of transition-metal ions (M^{z+}) as a promoter for the reactions catalyzed by the Au clusters, M^{z+} can be toxic even at low concentrations. Thus, it would be extremely worthwhile and desirable to develop new, less toxic promoters in the concept of "Green Chemistry".[11]

3.4.2 B) Au_{25} Nanoclusters with ILs for the Suzuki Cross Coupling Reaction

In recent years, ionic liquids (ILs) consisting of organic cations, e.g., 1-butyl-3-methylimidazolium, paired with various anions (Figure 3.8) have received much attention as green and designable solvents due to their unique properties, such as non-volatility, non-flammability, high chemical and thermal stability, low toxicity, high ion conductivity and wide electrochemical window.[103-105] ILs have been extensively used in many researches and industry fields, including synthesis, catalysis, separation, CO_2 capture, diesel fuel desulfurization, and biomass processing.[106-109] It is known that the hydrogen atom at the position-2 of imidazolium ions, hereafter referred to as H2, carries positive charge. It is acidic and thus tends to interact strongly with negatively charged sites of reactants via formation of a hydrogen bond. The acidic characteristic of the imidazolium based ionic

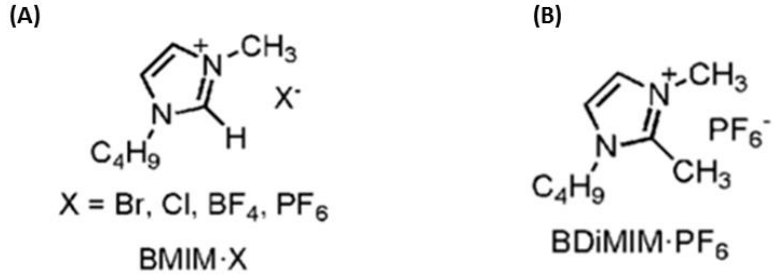

Figure 3.8. Imidazolium-based ILs. Top panel: 1-butyl-3-methylimidazolium (BMIM). Bottom panel: 1-butyl-2,3-dimethylimidazolium (BDiMIM).

liquids is believed to play an important role in, for example, CO_2 capture with the ethylmethylimidazolium acetate.[110,111] It also opens up the possibility of activating the thiolate-protected gold nanoclusters by removing of thiolate ligands, which has potential applications in heterogeneous catalysis (see results shown above for the use of Lewis acids). Herein we pursue this possibility further and consider the activation of $Au_{25}(SR)_{18}$ nanoclusters for catalytic reactions.

To investigate potential application of imidazolium based ionic liquids for activation of the thiolate-protected gold nanoclusters, the Suzuki cross-coupling reaction between *p*-iodoanisole and phenylboronic acid catalyzed by $Au_{25}(SR)_{18}$ nanoclusters is considered. To test this, our experimental collaborators in Prof. Jin's research group studied the reaction in the presence of some ionic liquids.[66] They have discovered that the addition of imidazolium-based ILs can markedly enhance the product conversion at mild temperatures (e.g., at 90 ^oC, Table 3.5).[66] Their experimental results indicate the $Au_{25}(SR)_{18}$ nanoclusters undergo structural changes after the treatment with BMIM·BF_4 (Figure 3.8).[66] These results suggest that the presence of the ILs may assist the formation

of active gold species from the parent nanoclusters, thereby providing open gold sites for catalytic reactions.

Using computational studies, the catalytic mechanisms, in particular, the roles played by ILs, are studied. While the mechanism of the Suzuki cross-coupling reactions catalyzed by gold nanoclusters is not fully understood yet, oxidative addition (in which the catalyst is oxidized by dissociation of a carbon-halogen bond on the catalyst) is believed to be the first key process that is often rate-limiting.[112-114] We therefore restrict our attention to oxidative addition of the Suzuki coupling reaction and analyze the roles played by imidazolium-based ILs via the DFT method. For efficient calculations, $Au_{25}(SCH_2CH_2Ph)_{18}$, iodoanisole, and BMIM are modeled as $Au_{25}(SCH_3)_{18}$, iodobenzene, and 1,3-dimethylimidazolium (DMI—$H2^+$), respectively.

We first investigated possible active sites on $Au_{25}(SCH_3)_{18}$ for oxidative addition. DFT results indicate that the protected Au_{25} cluster is inert toward the activation of the C–I bond. This strongly suggests that structural/electronic changes are necessary to activate the gold cluster towards the oxidative addition.

In ***Mechanism A***, we consider removal of fragments of Au_{25} cluster such as thiolate ligands and "-Au-SR" units via imidazolium cations. We first examine how a DMI—$H2^+$ cation interacts with and removes the fragments of the nanocluster, thereby producing low-coordinated gold atoms for iodobenzene adsorption. We should also note that Corma and coworkers reported the detection of H_2 formation during homo-coupling reaction on nanoclusters, indicating the possibility of gold oxidation.[115] In view of the protic nature of the solvents employed in the present work, it would be prudent to consider similar gold oxidation by H^+ for our system, especially at high temperatures, because the proton activity

Table 3.5. Catalytic performance of thiolate-capped Au_{25} cluster supported on titania as catalysts for Suzuki cross-coupling reaction of iodoanisole and phenylboronic acid.[a, 66]

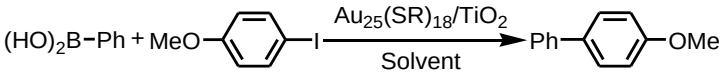

Entry	Solvent	Conversion [%][b]
1	EtOH:H_2O	<0.5
2	*o*-xylene + EtOH:H_2O	<0.5
3	$PhCH_3$ + EtOH:H_2O	<0.5
4	DMF + EtOH:H_2O	4
5	BMIM·Br + EtOH	89
6	BMIM·Cl + EtOH	90
7	BMIM·BF_4 + EtOH	94
8	BMIM·BF_4 + EtOH:H_2O	>99
9	BDiMIM·BF_4 + EtOH	<0.5

[a]Reaction conditions: 0.1 mmol iodoanisole, 0.12 mmol phenylboronic acid, 0.36 mmol K_2CO_3, 100 mg $Au_{25}(SR)_{18}/TiO_2$ (~1 wt.% cluster loading), solvents (1 mL EtOH or EtOH:H_2O (10:1, v/v), and 0.2 mL IL or other organic solvents), 90 °C, 18h. [b]The conversion of iodoanisole was determined by ^1H NMR.

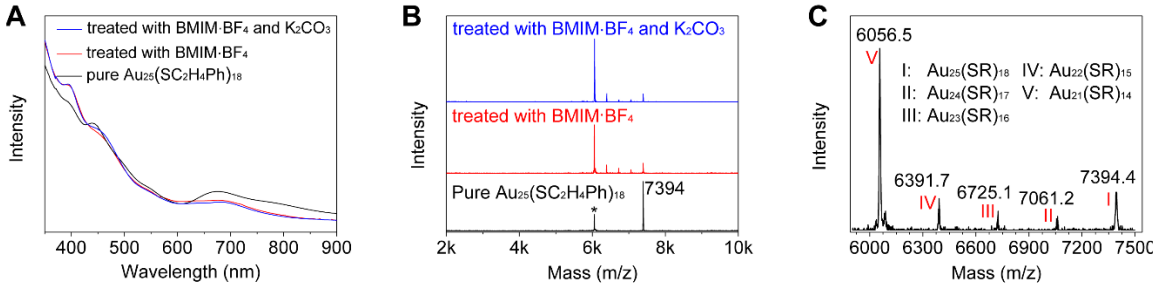

Figure 3.8. (A) UV-vis absorption spectra and (B) Positive mode MALDI mass spectra of the initial $[Au_{25}(SR)_{18}]^-$ (in dichloromethane) and samples after the treatment with BMIM•BF_4 or with BMIM•BF_4 and K_2CO_3. (C) Zoom-in of the MALDI mass spectrum of the sample after the treatment of $[Au_{25}(SR)_{18}]^-$ with BMIM•BF_4. The peak, in B, marked with an asterisk (*) is a fragment (i.e., the $Au_{21}(SR)_{14}$ species) caused by MALDI method, rather than an impurity. Of note, the laser intensity in the MALDI-MS of the three samples is the same.[66]

(chemical potential) increases with temperature. Thus in ***Mechanism B***, two different pathways for protonation of gold nanoclusters that can also produce active sites for iodobenzene adsorption are considered.

3.4.2.1 ***Mechanism A*** **for $Au_{24}(SR)_{17}$ generation.** As illustrated in Figure 3.1, there are two types of thiolate ligands on the staple motifs of $Au_{25}(SR)_{18}$ = $Au_{25}(SR1)_6(SR2)_{12}$, i.e., –SR ligands bridging two exterior Au atoms (SR1) and those bridging an exterior Au atom and Au_{13} icosahedral core (SR2). The average Au-S bond lengths in the $Au_{25}(SCH_2CH_2Ph)_{18}$ nanocluster are 2.372 and 2.308 Å for Au(core)-S(R2) and Au(staple)-S(R1), respectively (Table 3.2). The DFT results for optimized $Au_{25}(SR1)_5(SR2)_{12}$ and $Au_{25}(SR1)_6(SR2)_{11}$ (R = CH_3) in the gas phase indicate that the removal of –SR2 is energetically favored by 18.6 kcal/mol over that of –SR1, as expected from the Au-S bond length differences (Table 3.2).

With these results in mind, we consider ***Mechanism A*** in Figure 3.9. The first step (Reac → Int1) is adsorption of DMI—$H2^+$ onto –SR2 through the interaction between H2 of the former and S of the latter with interatomic distance of 2.47 Å. This in turn induces a considerable elongation (0.04 Å) of the Au(core)—SR2 bond. According to DFT calculations, the adsorption energy ΔE_{ad} (defined as E(NC/ad) – E(NC) – E(ad)) is -59.0 kcal/mol, where E(NC/ad), E(NC), and E(ad) are the energies of the adsorbed system, isolated gold nanocluster and isolated adsorbate, respectively (Table 3.6). The energy released from this exothermic step can assist the removal of the interacting –SR2/DMIM pair and thus the formation of $Au_{25}(SR1)_6(SR2)_{11}$ = $Au_{25}(SR)_{17}$ in the ensuing step (Int1 → Int2), which is 45.5 kcal/mol endothermic. In Figure 3.10, another pathway of thiolate

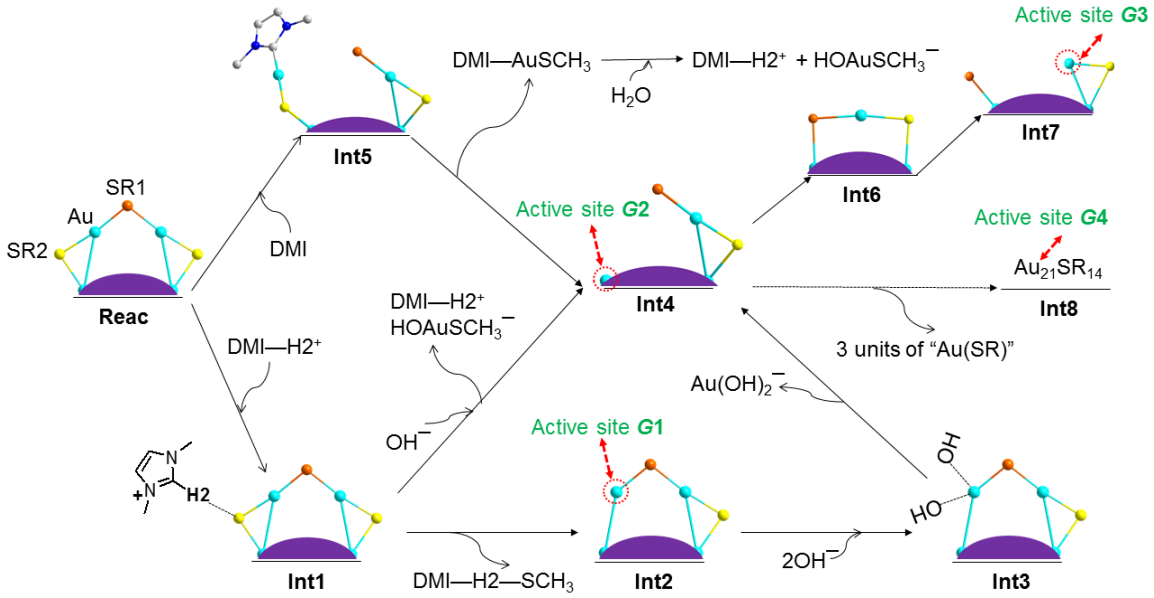

Figure 3.9. Proposed reaction *Mechanism A* for the formation of catalytic active sites on Au_{25} cluster promoted by imidazolium-based ionic liquids. Placement of the gold species in this schematic diagram is not based on their relative energies. The calculated energies for different steps are given in Table 3.6. Color code: Au, cyan; SR2, yellow; SR1, orange. The purple section represents the icosahedral Au_{13} core. The thiolate carbon tails are omitted for clarity.

Table 3.6. DFT results for ΔE (kcal/mol) for elementary steps of *Mechanism A* (Figure 3.9) in the gas and solution phase (PCM calculations, solvent = ethanol)

Steps	Gas phase	Solution phases
Reac → Int1	-59.0	+0.9
Int1 → Int2	+45.5	+34.3
Int2 → Int3	-178.3	-111.6
Int3 → Int4	-2.9	+12.1
Int1 → Int4	+6.0	-28.2
Reac → Int5	-22.1	-23.1
Int5 → Int4	+26.4	+15.5
Int4 → Int6	+0.9	+5.9
Int6 → Int7	+20.2	+13.4
Hydrolysis of DMI—Au—SCH_3	+103.0	+20.4

removal assisted by DMI—$H2^+$ is considered. Upon DMI—$H2^+$ adsorption, the thiolate group is first protonated (Int1 → Int1*), and then detached from the nanoparticle (Int1* → Int2). DFT predicts that this stepwise ligand removal is about 7 kcal/mol more endothermic than the single-step removal Int1→ Int2 in Figure 3.9. The higher endothermicity, in the stepwise process, is mainly because of the complete proton transfer from DMI—$H2^+$ to the thiolate group. The thiolate group removal yields a gold atom site, *G*1 (Figure 3.9), with only one ligand attached to it. Two hydroxide ($[OH]^-$) ions produced in the reaction media by K_2CO_3 (or IL anions) can coordinate to *G*1 with Au—O distance of 2.02 Å and energy release of 178.3 kcal/mol (Int2 → Int3). The coordinating $[OH]^-$ ions (or IL anions) eventually displace the Au atom from the nanocluster in an exothermic step with ΔE = -2.9 kcal/mol, where ΔE is the energy difference between the product and reactant states. This results in the formation of $[Au(OH)_2]^-$ and $[Au_{24}(SCH_3)_{17}]^-$ with a possible active metal site, *G*2, on the icosahedral Au_{13} core (Int3 → Int4).

Upon adsorption of DMI—$H2^+$ onto –SR2 (Int1), a hydroxide (or other anion) can attack the gold atom bonded to the –SR2 on the same staple motif. This step, which yields DMI—$H2^+$, $[HOAuSCH_3]^-$, and $[Au_{24}(SCH_3)_{17}]^-$ (Int1 → Int4, Figure 3.9), is found to be endothermic by 6.0 kcal/mol. Comparison with Int1 → Int2 suggests that the Int1 → Int4 step is more favorable from energetics point of view, in good agreement with the MALDI-MS results of the unsupported gold nanoclusters, i.e., $[Au_{24}(SR)_{17}]^-$ is detected but not $Au_{25}(SR)_{17}$. Furthermore, DFT shows that site *G*1, if produced, is not stable and thus is likely to react with the solvent media and ultimately detach from the nanocluster to form $[Au_{24}(SR)_{17}]^-$. Nonetheless, since the catalyst's support can stabilize the nanoclusters which are not stable thermodynamically in the solution phase, we do not rule out the

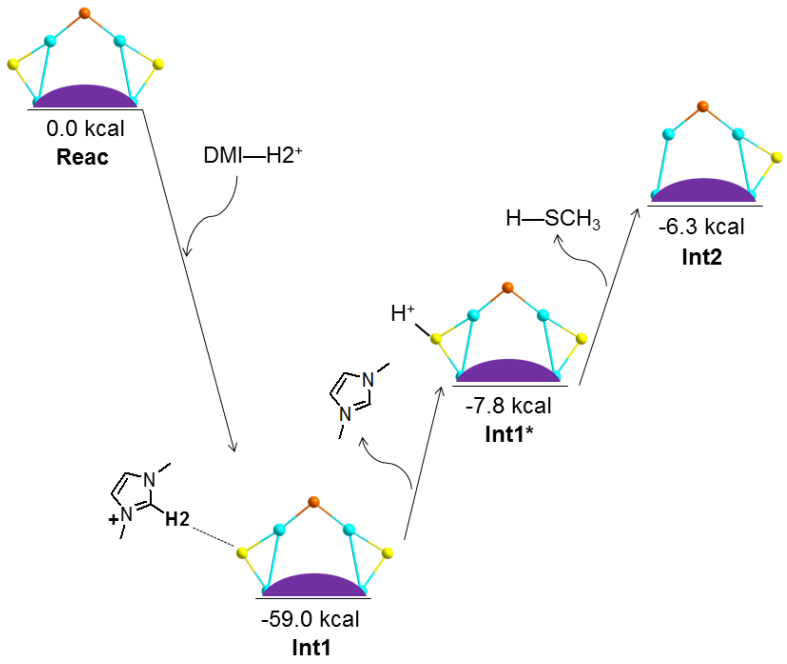

Figure 3.10. Proposed reaction based on thiolate group removal in the form of H—SCH_3. All energy values reported here are the DFT results in the gas phase, relative to the reactant state. Color code: Au, cyan; SR2, yellow; SR1, orange. The purple section represent Au_{13} kernel. The thiolate carbon tails are omitted for clarity.

possibility that *G*1 functions as a catalytically active site (see Table 3.7 below). Of note, the exposed gold atom in the core (Int2) that was bonded to the (removed) thiolate group becomes partially shielded by another staple motif situated nearby (cf. Figure 3.1). As such, it becomes less exposed and thus less active than the low-coordinated Au atom on the staple motif.

For completeness, we also considered the possibility of "-Au-SR" removal via N-heterocyclic carbene that can be formed from the imidazolium cation (Figure 3.11).[116,117] DFT results obtained with the all-electron 6-31G(d,p) basis set for sulfur indicate that 1,3-dimethylimidazol (DMI) does not show appreciable interactions with –SR groups or with Au atoms. However, when the corresponding valence basis set 6-31G(d,p) together with the appropriate Stuttgart-Dresden effective core potentials (ECPs) is employed for S,[118,119]

DMI can interact strongly with Au on the staple motif. This can lead to cleavage of the Au-SR1 bond with ΔE = -22.1 kcal/mol (Reac → Int5, Figure 3.9). The DMI—Au—SCH_3 moiety eventually detaches from the nanoparticle with ΔE = +26.4 kcal/mol (Int5 → Int4). The detached complex may undergo a hydrolysis to form DMI—$H2^+$ and $[HOAuSCH_3]^-$ with ΔE = +103.0 kcal/mol. In view of their strong basis-set dependence, however, care should be taken in the interpretation of the results for the carbene pathway presented here.

While $[Au_{24}(SR)_{17}]^-$ with *G2* (Int4) can catalyze cross-coupling reactions, it can also interact with DMI—$H2^+$ and form $[Au_{25-n}(SR)_{18-n}]^-$ through a sequential removal of "-Au-SR" units. Among different thiolate groups of Int4, the –SR1 group of the staple

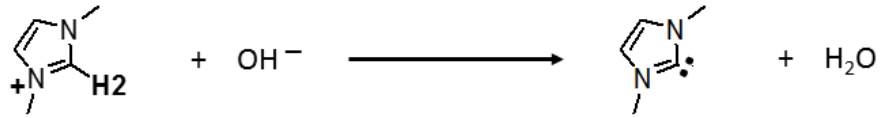

Figure 3.11. Formation of 1,3-dimethylimidazol (DMI) by treatment of the imidazolium ionic liquid DMI-$H2^+$ with a base (OH^-). DFT shows that ΔE for the reaction is -159.4 and -39.1 kcal/mol in the gas and solution phase (ethanol), respectively.

motif with a "-Au-SR2" unit removed probably provides the best site for DMI—$H2^+$ to interact with in the formation of $[Au_{23}(SR)_{16}]^-$. Because it is linked to only one Au, it is well exposed to the solvent media. Furthermore, the partial atomic charge for sulfur of the –SR1 group determined with the electro-static potential (ESP) method is -0.51, while that of the –SR2 groups is on average -0.34 (Figure 3.12). Thus the Coulomb interaction of the former with positively charged DMI—$H2^+$ will be stronger than that of the latter. The resulting $[Au_{23}(SR)_{16}]^-$ nanocluster can lose two more "-Au-SR" units from a nearby stable

motif in the same way and become $[Au_{21}(SR)_{14}]^-$ (Int4 → Int8**)** with an active site, *G*4 (Figure 3.13).

It is possible that $[Au_{24}(SR)_{17}]^-$ with *G2* can undergo a structural change via ligand exchange (Int4 → Int6 → Int7**)** as shown in Figure 3.9. In good agreement with the previous study discussed above, DFT predicts that the energy change Δ*E* of Int4 → Int6 and Int6→ Int7 steps is +0.9 and +20.2 kcal/mol, respectively. The formation of Int7 provides a metal site on a staple shell (*G*3), which can be active for the catalytic reaction.

While the gas-phase results provide useful insight into reactions' mechanisms, proper account of solvation effects is necessary for both qualitative and quantitative understanding of the catalytic activity in solution. Specifically, in a polar environment like ethanol, charged species become stabilized through electrostatic interactions with the solvent. As such, solvation can exert a strong influence on energetics of the Suzuki coupling reaction. We estimated the effect of solvent (ethanol) on Δ*E* for different steps shown in Figure 3.9 using PCM (polarizable continuum model) calculations. It should be mentioned that the small complexes were fully re-optimized using DFT/PCM calculations. Due to the high computational cost for the models containing the gold nanoclusters, only single point DFT/PCM calculation was conducted on the gas-phase optimized structures. Because of this approximation and due to the fact that the continuum approach tends to overestimate the solvation effect,[120] our results offer qualitative insights rather than accurately quantifying the actual exothermicity/endothermicity in the solution phase. As Table 3.6 indicates, solvation in a highly polar solvent can stabilize charged species like DMI—$H2^+$ and $[Au_{25-n}(SR)_{18-n}]^-$ significantly. For example, the Reac → Int1→ Int2 step becomes 35.2 kcal/mol endothermic in a polar solvent even though it is 13.5 kcal/mol

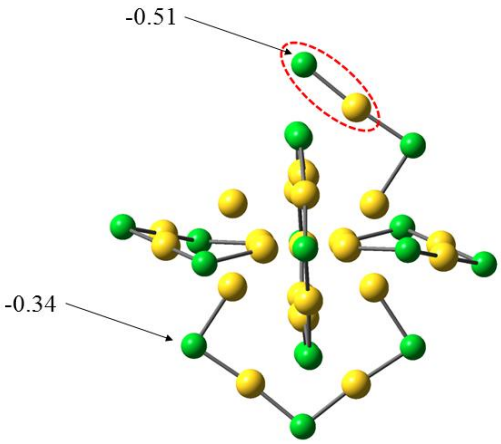

Figure 3.12. SR1-Au group of the same motif has less steric hindrance and more negative partial charge to interact with DMI-$H2^+$ better compared to the thiolate groups of other motifs to from $Au_{23}(SR)_{16}^-$. As shown, the partial atomic charge driven via the electro-static potential (ESP) method for sulfur of –SR1 group of the same motif is -0.51, while it is -0.34 on average for the –SR2 groups.

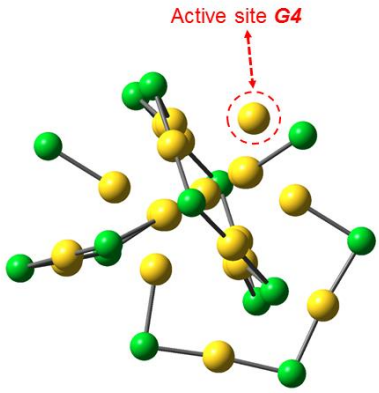

Figure 3.13. Molecular structure of $Au_{21}(SR)_{14}^-$ with a possible active site (*G*4) on the Au_{13}-core.

exothermic in the gas phase! A considerably lesser solvation effect is expected for steps where the charge species are not produced or consumed (e.g. Reac → Int5, Int4→ Int6, and Int6→ Int7). Consistent with the gas phase calculations and experimental results, DFT/PCM also indicates that the Int1 → Int2 step is less favorable than Int1 → Int4.

We also examined the ligand removal by regular solvents, in particular, ethanol and DMF. The adsorption energies are ΔE_{ad} = -4.9 and -1.9 kcal/mol for EtOH and DMF, respectively. Comparison with the DMI—$H2^+$ case (ΔE_{ad} = -59.0 kcal/mol) shows that the adsorption of DMI—$H2^+$ is strongly favored over that of EtOH or DMF. As for the interaction of the removed thiolate group ($[-SCH_3]^-$) with the solvents, we found that its bond energy is 19.3 kcal/mol with an EtOH molecule and 13.8 kcal/mol with a DMF molecule. This is much weaker than the interaction of the removed thiolate group with DMI—$H2^+$, which has a bond energy of 101.9 kcal/mol. The results for the adsorption and bond energies thus indicate that imidazolium cations are much more effective in removing thiolate ligands than polar solvent molecules. Even with the inclusion of the solvation effect, this conclusion appears to be valid.

To gain insight into ion pairing of BMIM and X (X= Cl, Br, BF_4) and its influence on BMIM reactivity towards thiolate ligands, we analyzed the distribution of anions X around H2 of BMIM using molecular dynamics (MD) simulations. The results for X= BF_4 (Figure 3.14) show that ion pairing via H2 is reduced substantially in EtOH, compared to pure IL. This suggests that solvation in polar solvents tends to break IL ion pairs and make H2 of BMIM available to interact with thiolate ligands of the nanoclusters; viz., solvation enhances BMIM's adsorption capability.

The low-coordinated Au atoms (*G*1, *G*2, *G*3, and *G*4) on the nanoclusters that are produced with the help of ionic liquids may act as active sites to adsorb iodobenzene. For insight into their catalytic activity, we examined adsorption energy, ΔE_{ad}, of iodobenzene on these sites. DFT with the LANL2DZ basis set for iodine (and gold) yields ΔE_{ad} of -3.5, -3.5, -7.5, and -9.1 kcal/mol for *G*1, *G*2, *G*3, and *G*4, respectively (Table 3.7). With the

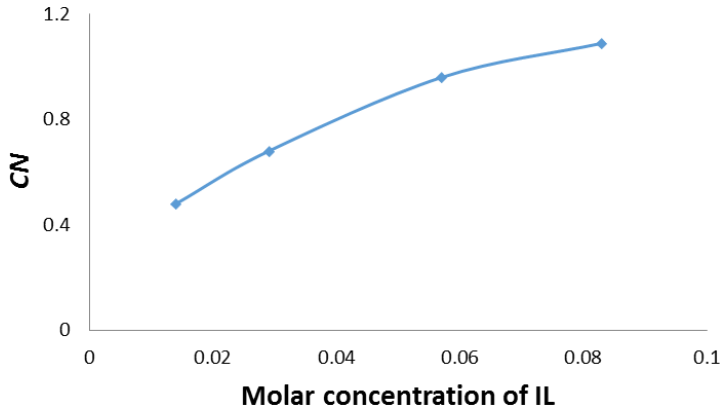

Figure 3.14. Average coordination number of H2 (BMIM) with respect to BF_4^- obtained from MD simulations. Coordination number (*CN*) is defined as number of BF_4^- found in the first solvation shell around H2 (BMIM).

MIDI! basis set employed for iodine, ΔE_{ad} becomes -10.8, -12.3, -18.5, and -19.1 kcal/mol, respectively. This increase in the magnitude of ΔE_{ad} is attributed to the polarization functions included in the MIDI! basis set, which allow iodine to be hypervalent (with carbon and gold). We note that with the exception of $[Au_{25}(SR)_{17}]^0$ which is neutral, nanoclusters carry a net charge of -1 (see Figure 3.9). However, in a protic solvent such as ethanol and water, it would be prudent to consider the oxidation of Au particles. Although the redox potential (E_0) for such a reaction is not high enough for spontaneous oxidation of bulk gold, previous studies indicate that the oxidation potential of metal nanoclusters is usually size-dependent and tends to decrease as they become smaller.[121-124] This decrease is attributed to change in Gibbs free energy, which is associated with a high surface-to-volume ratio and chemical potential of the particles. Such a change in the oxidation potential is shown for small metal clusters that can reduce organics.[125] Our analysis shows that the oxidation of the Au nanoclusters usually leads to a superior interaction between

Table 3.7. Adsorption energy (ΔE_{ad}, kcal/mol) of iodobenzene on different active sites shown in Figure 3.9 at different oxidation states. Units for Au—I: Å. The stronger interaction between iodine and the active gold sites can be tracked by the shorter Au—I bond length.

Active site	Cluster	ΔE_{ad}	Au—I
G1	$[Au_{25}(SR)_{17}]^0$	-3.5 (-10.8)	3.116 (2.859)
	$[Au_{25}(SR)_{17}]^+$	-5.7	2.992
G2	$[Au_{24}(SR)_{17}]^-$	-3.5 (-12.3)	3.025 (2.802)
	$[Au_{24}(SR)_{17}]^0$	-4.8	2.974
	$[Au_{24}(SR)_{17}]^+$	-6.6	2.946
G3	$[Au_{24}(SR)_{17}]^-$	-7.5 (-18.9)	2.920 (2.686)
	$[Au_{24}(SR)_{17}]^0$	-13.3	2.759
G4	$[Au_{21}(SR)_{14}]^-$	-9.1 (-19.1)	2.912 (2.754)
	$[Au_{21}(SR)_{14}]^0$	-11.8	2.854
	$[Au_{21}(SR)_{14}]^+$	-5.2	3.375

iodobenzene and the active sites (see Table 3.7). Among all active sites studied here, *G*3 and *G*4 on the neutral Au nanoclusters, $[Au_{24}(SR)_{17}]^0$ and $[Au_{21}(SR)_{14}]^0$, show the strongest interaction with iodobenzene.

We also studied how oxidation of the gold cluster may influence the interaction between the IL cations and nanoclusters. DFT predicts that the interaction of DMI—$H2^+$ with -SR2 group of $[Au_{25}(SR)_{18}]^0$ and $[Au_{25}(SR)_{18}]^+$ in the gas phase is -20.3 and +23.2 kcal/mol, respectively. These interactions are considerably weaker than that between DMI—$H2^+$ and -SR2 group of $[Au_{25}(SR)_{18}]^-$ (-59.0 kcal/mol, Reac → Int1, Table 3.3). We can qualitatively understand the results as follows: All other things being equal, the interaction of two opposite charges (DMI—$H2^+$ and $[Au_{25}(SR)_{18}]^-$) is stronger than that

of two like charges (DMI—$H2^+$ and $[Au_{25}(SR)_{18}]^+$) or of a neutral ($[Au_{25}(SR)_{18}]^0$) and a charge (DMI—$H2^+$). Our analysis indicates that oxidation of the Au nanoclusters may prevent further fragmentation of the nanoparticles induced by ILs.

3.4.2.2 *Mechanism B* for $Au_{24}(SR)_{17}$ generation. Finally, we consider the activation of Au nanoclusters via protonation (Figure 3.15). There are three different possible sites on the Au nanocluster that can adsorb protons generated in the media: sulfur atoms of two different thiolate groups (-SR1 and -SR2) and the surface gold atoms. According to the DFT calculations, protonation of –SR2 is more favorable by 12.4 and 17.0 kcal/mol than the protonation of -SR1 and surface gold atoms, respectively. Removal of protonated –SR1 and –SR2 was found to be endothermic by 7.7 and 1.5 kcal/mol, respectively. As such, protonated thiolate groups (-SR2) may eventually be dissociated from the nanocluster, yielding low coordinated gold atoms for the catalytic reaction (Figure 3.15A), similar to Int2 in Figure 3.9. Since the increase in temperature lowers proton adsorption selectivity, one should also consider protonation of gold atoms, especially at elevated temperatures (Reac* in Figure 3.15B). The adsorbed H^+ on the gold is capable of interacting with iodine of iodobenzene with energy release 3.2 kcal/mol (Reac* → Int11). With MIDI! basis set for I, the result becomes ΔE = -5.9 kcal/mol. Since any protic solvent molecules can be the source of proton, our theoretical analysis here predicts that a weak acid, such as acetic acid, is a better promoter than regular solvents. Specifically, the DFT result for interaction energy between CH_3COOH and a removed thiolate group ($[-SCH_3]^-$) is -25.0 kcal/mol. Although this interaction is considerably weaker than that of the removed thiolate group with DMI—$H2^+$ (-101.9 kcal/mol), it is stronger than the interaction of DMF, EtOH, or water with $[-SCH_3]^-$. Therefore, CH_3COOH would promote the cross

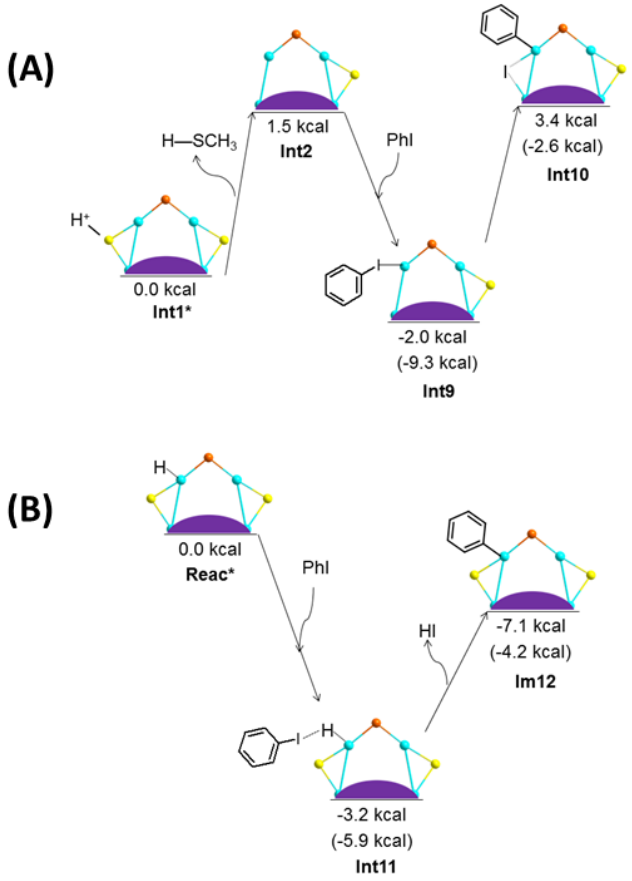

Figure 3.15. Proposed reaction *Mechanism B* based on protonation of (A) SR2 and (B) gold nanoclusters. Notations are the same as in Figures 3.9 and 3.11. In A, DFT with the LANL2DZ basis set for iodine (and gold) yields ΔE_{ad} of -3.50 kcal/mol for Int2 → Int9. With the MIDI! basis set employed for iodine, the magnitude of ΔE_{ad} increases to 10.8 kcal/mol. This increase is attributed to the polarization functions included in the MIDI! basis set, which allow iodine to be hypervalent (with carbon and gold). The adsorption of iodobenzene is followed by the dissociation of its C-I bond on the gold atom site (Int9 → Int10), which is 5.37 kcal/mol endothermic (6.7 kcal/mol with the MIDI! basis set). Iodine occupies the sulfur position of the removed SR2. In B, the adsorbed H^+ on the gold is capable of interacting with iodine of iodobenzene exothermically (Reac* → Int11). This step is followed by C-I bond dissociation, adsorption of phenyl on the gold, and then formation of HI (Int11 → Int12). Results obtained with the MIDI! basis set for iodine are given in parentheses.

coupling reaction better than the regular solvents, even though not as well as ILs. To test this, we asked Prof. Jin's research group to proceed: The $Au_{25}(SR)_{18}/TiO_2$ catalyst was stirred for 12h at room temperature in a solution of ethanol/acetic acid

($Au_{25}(SR)_{18}$:CH_3COOH = 1:100, mol/mol). Next, the $Au_{25}(SR)_{18}/TiO_2$ catalyst was separated by centrifugation and washed with ethanol for three times. The treated catalyst was then examined for the coupling reaction in a mixture solution of DMF/EtOH/water (same as entry 4 of Table 3.5). Their results show the reaction conversion reach 9%, more than twice the result in entry 4 of Table 3.5, in good agreement with our theoretical predictions. This indicates that our computational analysis via DFT/PCM, though qualitative, properly captures energetics of Suzuki cross coupling reactions in solution.

3.4.3 C) Au_{25} Nanoclusters Protected with Aromatic and Aliphatic Ligands.

Chemical nature of the protecting ligands can influence the properties of a nanocluster. For example, the redox potentials of $Au_{25}(SR)_{18}$ clusters are reported to be affected by the side chain of protected –SPhX ligands (where X = NO_2, Br, H, CH_3, and OCH_3).[126] Electron-withdrawing ligands are shown to energetically favor reduction and disfavor oxidation.[126] DFT calculations indicate an electron donating group like $–OCH_3$ at the para-position of $Au_{25}(SPhX)_{18}$ decreases HOMO-LUMO gap of the nanoclusters.[127] Optical properties of the $Au_{36}(SR)_{24}$ nanoclusters are also shown to be influenced by surface-protecting ligands (i.e., aliphatic thiolate, cyclopentanethiolate ($-SC_5H_9$) *vs.* aromatic thiolate, 4-*tert*-butylbenzenethiolate ($-SPh^tBu$)).[128] For example, UV-vis spectra of the $Au_{36}(SC_5H_9)_{24}$ and $Au_{36}(SPh^tBu)_{24}$ nanoclusters are found to have similar a general feature, but the spectrum of the $Au_{36}(SPh^tBu)_{24}$ is overall red-shifted in comparison to that of the $Au_{36}(SC_5H_9)_{24}$ nanocluster.[128]

To precisely correlate the electronic properties of the gold nanoclusters with their molecular structure, synthesis and crystallization of the nanoclusters with different

protecting thiolate ligands are necessary. As mentioned above, new properties can possibly be imparted by aromatic thiolate ligands to the $[Au_{25}(SR)_{18}]^-$ nanoclusters. Therefore, it is both highly desirable and valuable to study the nanoclusters capped by the aromatic thiolates. Furthermore, this may also unveil how to tune the catalytic properties of Au_{25} nanoclusters for specific reactions via ligand engineering.

We herein report the electronic and catalytic properties of an aromatic-thiolate-protected $[Au_{25}(SNap)_{18}]^-$ nanocluster (where, SNap = 1-naphthalenethiolate). The results show that the aromatic ligands can largely improve the stabilities of the Au_{25} nanoclusters. The nanocluster is further explored for catalytic application in the Ullmann hetero-coupling reaction between 4-methyl-iodobenzene and 4-nitro-iodobenzene. Our results indicate that aromatic ligands notably increase the conversion of substrate and the selectivity for the hetero-coupling product.

3.4.3.1 ***Electronic and structural properties.*** To gain insights into the electronic properties of the nanoclusters capped by aromatic ligands vs. aliphatic ones, we performed density functional theory (DFT) calculations of $Au_{25}(SCH_3)_{18}$ and $Au_{25}(SPh)_{18}$, which act as models of the aliphatic and aromatic ligands-protected clusters. The replacement of $-SCH_3$ ligands with -SPh leads to a slight decrease (0.03 eV) of the HOMO-LUMO gap of the gold nanoclusters. This is expected to induce a red-shift of the optical spectrum of the clusters protected by aromatic ligands (-SPh). To test this, the time-dependent density functional theory (TD-DFT) was applied to calculate the theoretical optical absorption spectra of the clusters. We considered only the first (lowest energy) absorption peak. The maximum-intensity lines of the absorption peak of the $Au_{25}(SCH_3)_{18}$ and the $Au_{25}(SPh)_{18}$ are located at 844 and 868 nm, respectively (Figure 3.16a, insets). The most salient aspect

of our results is that the first theoretical peak of the $Au_{25}(SPh)_{18}$ is red-shifted by ~24 nm compared to that of the $Au_{25}(SCH_3)_{18}$, which is in good agreement with the experimental result provided by our collaborators in Prof. Jin's research group (27 nm, Figure 3.16).[65] DFT calculations also show that HOMO and LUMO levels of $[Au_{25}(SCH_3)_{18}]^-$ are higher by 0.28 and 0.31 eV respectively than those of $[Au_{25}(SPh)_{18}]^-$. Therefore, from the electronic point of view, the $[Au_{25}(SCH_3)_{18}]^-$ is more accessible to react with an oxidizing agents like H_2O_2 and TBHP or loses electrons at the surface of the anode compared to the aromatic-thiolate-protected nanoclusters. This indicates the nanoclusters capped with aromatic ligands should have higher thermal and anti-oxidative properties.

Matrix-assisted laser desorption/ionization mass spectrometry (MALDI-MS) of the $Au_{25}(SCH_2CH_2Ph)_{18}$ nanocluster, performed by Prof. Jin's research group, shows two peaks, which are assigned to the intact nanocluster (*m/z*: 7394.3, theoretical *m/z*: 7394.2)

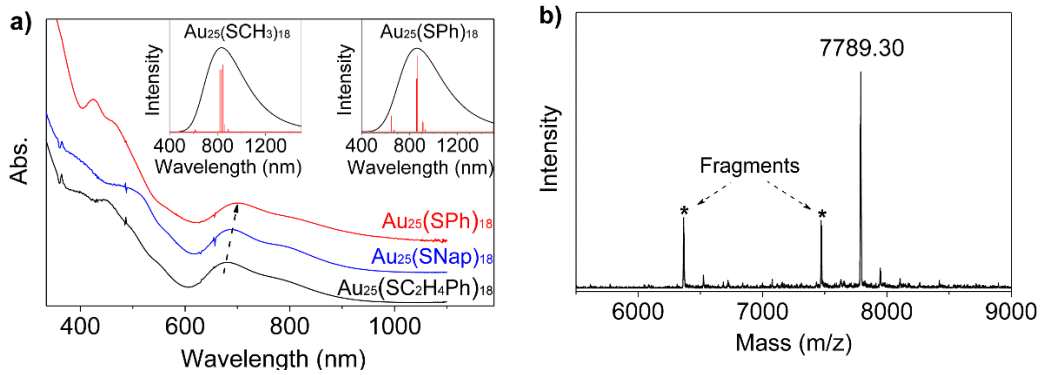

Figure 3.16. (a) Comparison of the optical spectra of the $Au_{25}(SCH_2CH_2Ph)_{18}$, $Au_{25}(SPh)_{18}$ and $Au_{25}(SNap)_{18}$ nanoclusters. The spectra are up-shifted for the ease of comparison. Inset: the calculated lowest-energy peaks of $Au_{25}(SCH_3)_{18}$ and $Au_{25}(SPh)_{18}$. (b) Positive-mode MADLI spectrum of $Au_{25}(SNap)_{18}$ nanoclusters. The asterisks (*) in (b) indicate the fragments (i.e., $Au_{21}(SNap)_{14}$ and $Au_{25}(SNap)_{16}$) caused by MALDI method.[65]

and its fragment $Au_{21}(SCH_2CH_2Ph)_{14}$ at *m/z* = 6057.2 (i.e., after loss of $Au_4(SCH_2CH_2Ph)_4$).[65] The main peak of MALDI-MS of the $Au_{25}(SNap)_{18}$ is found to be at *m/z* = 7789.30, which is assigned to the intact nanocluster (Figure 3.16b).[65] The MALDI-MS of the aromatic protected nanocluster shows two fragment ions at *m/z* = 6365.0 (assigned to $Au_{21}(SNap)_{14}$, i.e., losing a unit of $Au_4(SNap)_4$) and at *m/z* = 7471.4 (assigned to $Au_{25}(SNap)_{16}$, which indicates the loss of two protecting thiolate ligands).[65] We attempted to explain the fragmentation results using DFT calculations. A $-SCH_3$ group bridging an exterior Au atom and Au_{13} kernel of the $Au_{25}(SCH_3)_{18}$ model was replaced with -SNap, resulting in $Au_{25}(SCH_3)_{17}(SNap)_1$. DFT shows the replacement of $-SCH_3$ with -SNap leads to elongation of $Au_{(kernel)}$–S bond by 0.032 Å. Results also indicate that the formation of $Au_{25}(SCH_3)_{17}$ species via removal of -SNap group in forms of anion or radical is energetically favored by 27.6 and 12.3 kcal/mol over that of SCH_3, as expected from the change in the $Au_{(kernel)}$–S bond length. These findings are in line with the fact that naphthalene group of -SNap is more capable of stabilizing the electrons of sulfur atom through π-resonance than the alkyl group of $-SCH_3$. Therefore, losing -SNap groups during MALDI-MS is more probable than $-SCH_3$ as confirmed by our experimental results

We rationalize that the $Au_{25}(SNap)_{18}$ and $Au_{25}(SCH_2CH_2Ph)_{18}$ nanoclusters would exhibit different catalytic activities given their differences in electronic properties caused by the ligands. To test this, we choose a carbon–carbon coupling reaction. Our experimental collaborators in Prof. Jin's group reported the catalytic properties of the Au_{25} nanoclusters protected by different ligands ($-SC_6H_{13}$, $-SCH_2CH_2Ph$, -SPh, and -SNap) in the Ullmann hetero-coupling reaction.[65] Their results are compiled in Table 3.8.[65] The most salient aspect of their results is that the use of Au_{25} nanoclusters protected by the aromatic

ligands dramatically increases the selectivity towards the hetero-coupling product, indicating that the chemical nature of the protecting ligands exerts a major influence on the catalytic properties of the nanoclusters.

3.4.3.2 Catalysis mechanism. To explain the catalytic results, we carried out DFT calculations. All surface gold atoms of $Au_{25}(SR)_{18}$ are protected by thiolate groups; therefore, the nanoclusters are shown to be inert toward adsorption of non-radical molecules, as expected. According to our previous studies, we hypothesize that a thiolate is lost and two gold atoms of the staple motif are thus exposed to reactants (Figure 3.17). To account for the effects of protecting ligands on the catalytic activity of the nanoclusters, two remaining thiolate ligands on the same staple motif are set to be either –SNap or $–SCH_3$. The rest of thiolate ligands are –SH in order to reduce the computational costs (Figure 3.17). DFT calculations show that the interaction energy of 4-nitro-iodobenzene with the exposed gold atoms of $Au_{25}(SCH_3)_2(SH)_{15}$ and $Au_{25}(SNap)_2(SH)_{15}$ is -4.3 and -7.2 kcal/mol with Au–I bond length of 2.87 and 2.82 Å (Figure 3.18). These results indicate that replacement of aliphatic thiolate ligands with aromatic ones leads to a better activation of the C–I bond in the substrate, thereby increasing the reaction conversion. These finding are in good agreement with the experimental results. To shed light on the catalytic selectivity results, the nudged elastic band (NEB) approach was used to calculate transition states and activation energy of homo- and hetero-coupling reactions.[129] For efficient calculations, only the staple motif and four gold atoms of the Au_{13} kernel that are closely bound to the motif are taken into account (Figures 3.19-3.21). Of note, the later four gold atoms were kept fixed during the NEB calculations. Results indicate the activation energy for the homo- and hetero-coupling reactions with $-SCH_3$ ligands are comparable (Figure 3.22a). Interestingly,

Table 3.8. The catalytic performance of $Au_{25}(SR)_{18}/CeO_2$ catalysts for Ullmann hetero-coupling between 4-methyl-iodobenzene and 4-nitro-iodobenzene.[a, 65]

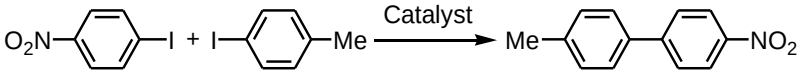

Entry	Catalyst	Conv. [%][b]	Selectivity [%][b]
1	$Au_{25}(SC_6H_{13})_{18}/CeO_2$	69	16
2	$Au_{25}(SCH_2CH_2Ph)_{18}/CeO_2$	72	19
3	$Au_{25}(SPh)_{18}/CeO_2$	80	50
4	$Au_{25}(SNap)_{18}/CeO_2$	91	82
5	CeO_2	n.r.	-
6	"Au-SNap" polymer/CeO_2	21	14
7[c]	$Au_{25}(SNap)_{18}/CeO_2$	79	47
8[d]	$Au_{25}(SNap)_{18}/CeO_2$	50	15

[a]Reaction conditions: 0.06 mmol 4-methyl iodobenzene, 0.05 mmol 4-nitroiodobenzene, 0.3 mmol k_2CO_3, 100 mg $Au_{25}(SR)_{18}/CeO_2$ (~ 1wt.% $Au_{25}(SR)_{18}$ loading), 1 mL DMF, 130 °C, 24 h. [b]The conversion based on 4-nitroiodobenzene and selectivity for the hetero-coupling product 4-methyl-4'-nitro-1,1'-biphenyl were determined by ^{1}H NMR. [c]2nd and [d]3rd reuses of the catalyst recovered from entry 4. n.r. represents no reaction.

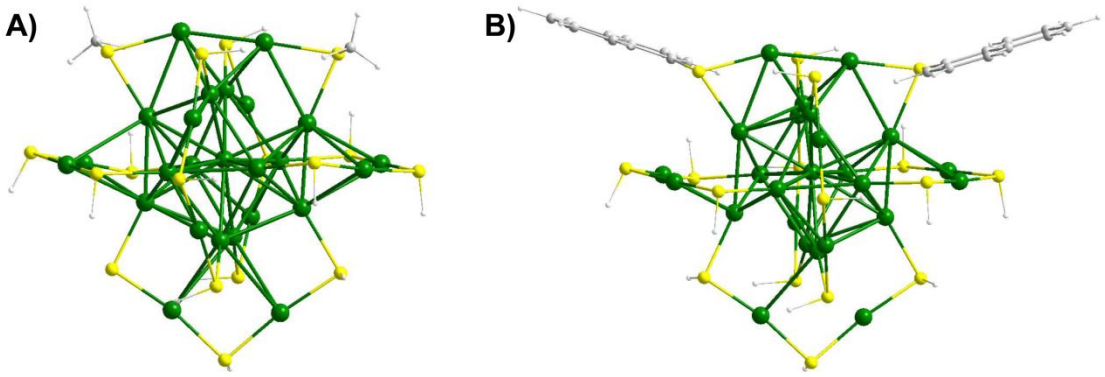

Figure 3.17. Optimized molecular structure of (A) $Au_{25}(SCH_3)_2(SH)_{15}$ and (B) $Au_{25}(SNap)_2(SH)_{15}$.

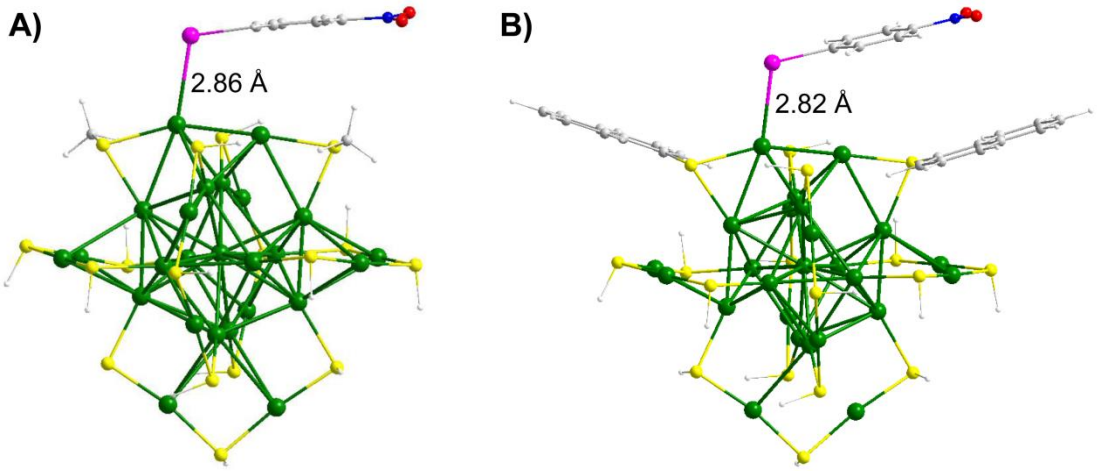

Figure 3.18. Interaction of 4-nitro-iodobenzene with the exposed gold atoms of (A) $Au_{25}(SCH_3)_2(SH)_{15}$ and (B) $Au_{25}(SNap)_2(SH)_{15}$.

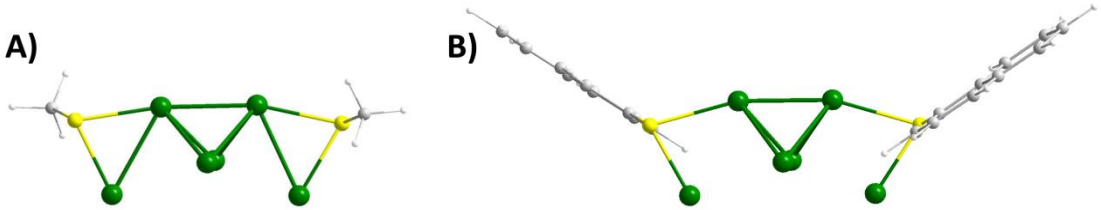

Figure 3.19. Models used for NEB calculation: (A) with -SCH_3 ligands and (B) with -SNap ligands.

the activation energy of hetero-coupling reaction is 2.7 kcal/mol less than that of homo-coupling if -SNap ligands are used (Figure 3.22b). These results altogether show that replacement of aliphatic thiolate ligands with aromatic ones not only increases the conversion rate of the reaction but also favors formation of hetero-coupled product over the homo-coupled one, consistent with our experimental results. Though our DFT calculations proposed that removal of some protecting ligands are required to provide catalytic active sites, the -SR ligands nearby the open metal sites play a key role in catalytic

efficiency and selectivity. In other words, DFT calculations suggest that $Au_{25}(SR)_{18-x}$ where $0 < x << 18$ is the active catalyst.

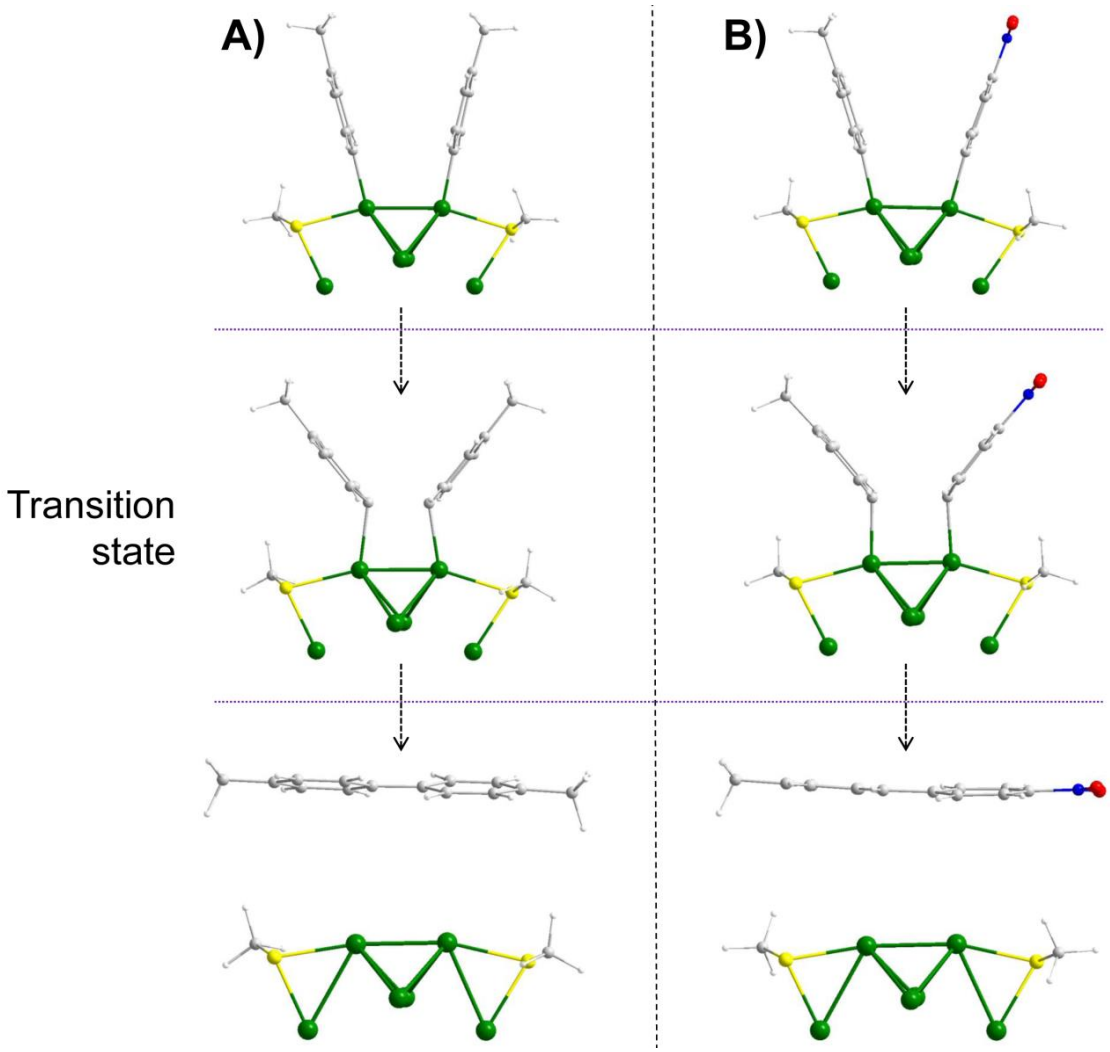

Figure 3.20. Proposed mechanism for (A) homo- and (B) hetero-coupling reactions with -SCH_3 ligands.

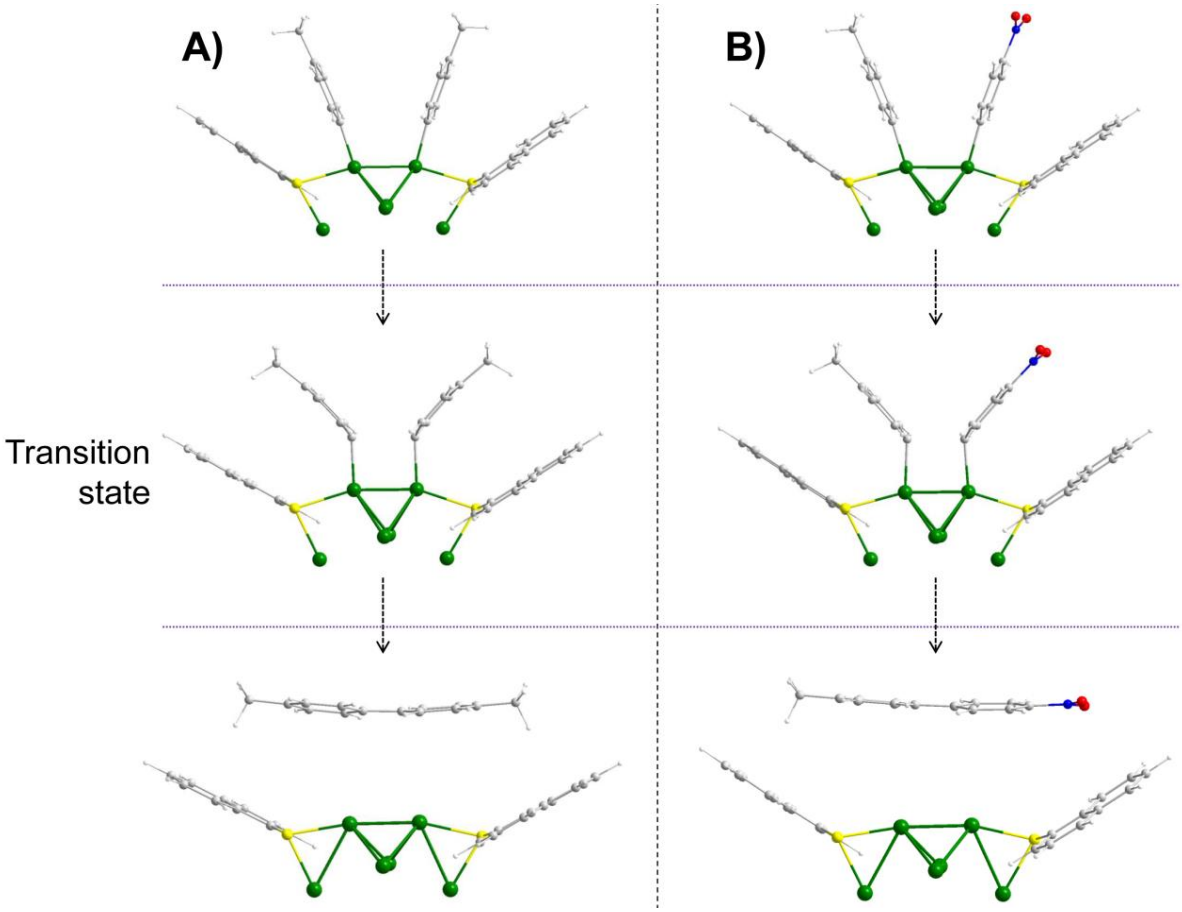

Figure 3.21. Proposed mechanism for (A) homo- and (B) hetero-coupling reactions with -SNap ligands.

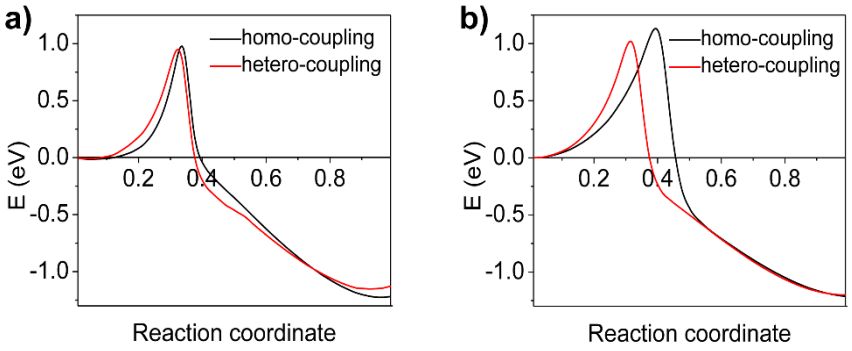

Figure 3.22. Energy vs. reaction coordinate of the hetero- and homo-coupling reactions with (a) $–SCH_3$ and (b) -SNap ligands.

3.5 Conclusions

In this study, computational tools are employed to investigate the activation of the $Au_{25}(SR)_{18}$ catalyst in the presence of transition metal Lewis-acids and imidazolium-based ionic liquids. Results show the presence of the promoters in solution can significantly enhance the catalytic activity of $Au_{25}(SR)_{18}$ nanoclusters via generation of new nanocluster species $Au_{25-n}(SR)_{18-n}$. The mechanisms of the removal of "–Au–SR–" fragments to produce $Au_{25-n}(SR)_{18-n}$ from the $Au_{25}(SR)_{18}$ parent nanoclusters in the presence of the promoters are proposed. DFT results indicate that either the surface gold atoms on the Au_{13}-core, staple shell, or the Lewis-acids bound on the Au_{13}-core provide catalytic active sites for the catalytic reactions. Using DFT calculations, we also resolved the effects of protecting thiolate ligands on the activation of the catalyst. Results show the activity and selectivity of the catalysts are largely enhanced by the nature of aromatic thiolate ligands.

3.6 Acknowledgments

This work is supported in part by NSF Grant No. CHE-1223988.

3.7 References

1) *Catalysis: From Principles to Applications*, edited by M. Beller, A. Renken and R. van Santen, Wiley-VCH Verlag GmbH & Co. KGaA, Weinheim, 2012.
2) *Applied Industrial Catalysis*, edited by L. Bruce, Academic press Inc., New York, 1983.
3) *Catalysis in Petroleum and Petrochemical Industries*, edited by A. K. Talukdar and K. G. Bhattacharyya, Narosa Publishing House, New Delhi, 2005.
4) *The Basis and Applications of Heterogeneous Catalysis*, edited by M. Bowker, Oxford University Press, Oxford, 1998.
5) *Catalysis: an Integrated Approach to Homogeneous, Heterogeneous and Industrial Catalysis*, edited by J.A. Moulijn, P.N.W.M. van Leeuwen and R.A. van Santen, Elsevier, Amsterdam, 1993.

6) R. A. Sheldon, I. W. C. E. Arends and U. Hanefeld, *Green Chemistry and Catalysis*, Wiley-VCH Verlag GmbH & Co. KGaA, Weinheim, 2007.
7) M. Poliakoff and P. Licence, *Nature*, 2007, **450**, 810–812.
8) J. H. Clark, *Green Chem.*, 1999, **1**, 1-8.
9) J. A. Linthorst, *Foundations of Chemistry*, 2010, **12**, 55-68.
10) G. Rothenberg, *Catalysis: Concepts and Green Applications*, Wiley-VCH Verlag GmbH & Co. KGaA, Weinheim, 2008.
11) http://www2.epa.gov/greenchemistry/basics-green-chemistry
12) D. Kubička, *Collect. Czech. Chem. Commun*., 2008, **73**, 1015-1044.
13) D. Kubička, I. Kubičková and J. Čejka, *Cat. Rev. - Sci. Eng.*, 2013, **55**, 1-78.
14) H. Szabolcs, O. György and K. Dénes, *Microporous Mesoporous Mater*., 2013, **167**, 109-116.
15) *Multimetallic Catalysts in Organic Synthesis*, edited by M. Shibasaki and Y. Yamamoto, Wiley-VCH Verlag GmbH & Co. KGaA, Weinheim, 2004.
16) *Innovative Catalysis in Organic Synthesis: Oxidation, Hydrogenation, and C-X Bond Forming Reactions*, edited by P. G. Andersson ,Wiley-VCH Verlag GmbH & Co. KGaA, Weinheim, 2012.
17) D. Astruc, *New J. Chem.*, 2005, **29**, 42–56.
18) T. M. Trnka and R. H. Grubbs, *Acc. Chem. Res*., 2001, **34**, 18–29.
19) *Applications of Transition Metal Catalysis in Drug Discovery and Development: An Industrial Perspective*, edited by M. L. Crawley and B. M. Trost, John Wiley & Sons, Inc., 2012.
20) M. Dusselier, P. Van Wouwe, A. Dewaele, P. A. Jacobs and B. F. Sels, *Science*, 2015, **349**, 78-80.
21) A. Z. Fadhel, P. Pollet, C. L. Liotta and C. A. Eckert, *Molecules*, 2010, **15**, 8400-8424.
22) J. Hagen, *Industrial Catalysis: A Practical Approach*, Wiley-VCH Verlag GmbH & Co. KGaA, Weinheim, 2006.
23) W.A. Herrmann and C.W. Kohlpaintner, *Angew. Chem.-Int. Ed. English*, 1993, **32**, 1524-1544.
24) F. Alonso, I. P. Beletskaya and M. Yus, *Tetrahedron*, 2008, **64**, 3047–3101.
25) G. Li and R. Jin, *Nanotechnol. Rev*., 2013, **5**, 529–545.
26) R. Jin, *Nanotechnol. Rev.*, 2012, **1**, 31–56.
27) K. Shimizu, *Catal. Sci. Technol*., 2015, **5**, 1412-1427.
28) K. Kaneda, K. Ebitani, T. Mizugaki and K. Mori, *Bull. Chem. Soc. Jpn*, 2006, **79**, 981-1016.
29) F. Felpin and E. Fouquet, *ChemSusChem*, 2008, **1**, 718-724.
30) M. J. Climent, A. Corma and S. Iborra, *Chem. Rev*., 2011, **111**, 1072-1133.
31) M. Tamura, K. Shimizu and A. Satsuma, *Chem. Lett*., 2012, **41**, 1397-1405.
32) *Renewable Resources and Renewable Energy: A Global Challenge*, edited by M. Graziani and P. Fornasiero, Taylor & Francis Eds., New York, 2006.
33) R. J. Farrauto, Y. Liu, W. Ruettinger, O. Ilinich, L. Shore and T. Giroux, *Cat. Rev. Sci. Eng.*, 2007, **49**, 141-196.
34) R. M. Heck, R. J. Ferrauto and S. T. Gulati, *Catalytic Air Pollution Control: Commercial Technology*, John Wiley & Sons, Inc., Hoboken, 2009.
35) M. Stratakis and H. Garcia, *Chem. Rev*., 2012, **112**, 4469-4506.

36) X. Liu, L. He, Y. M. Liu and Y. Cao, *Acc. Chem. Res*., 2014, **47**, 793-804.
37) M. C. Daniel and D. Astruc, *Chem. Rev*., 2014, **104**, 293–346.
38) R. A. Sperling, P. R. Gil, F. Zhang, M. Zanella and W. J. Parak, *Chem. Soc. Rev*., 2008, **37**, 1896-1908.
39) B. Hvolbaek, T. V. W. Janssens, B. S. Clausen, H. Falsig, C. H. Christensen and J. K. Norskov, *Nano Today*, 2007, **2**, 14–18.
40) X. Zhou, W. Xu, G. Liu, D. Panda and P. Chen, *J. Am. Chem. Soc*., 2010, **132**, 138–146.
41) M. T. Sharbati, F. Panahi and A. Gharavi, *IEEE Photonics Technol. Lett*., 2010, **22**, 1695-1697.
42) M. T. Sharbati, M. N. Soltani Rad, S. Behrouz, A. Gharavi and F. Emami, *J. Lumin*., 2011, **131**, 553-558.
43) M.T. Sharbati, F. Panahi, A. Shourvarzi, S .Khademi and F. Emami, *Optik*, 2013, **124**, 52-54.
44) M. T. Sharbati, A. Gharavi and F. Emami, *Display Technol*., 2011, **4**, 181–185.
45) M. T. Sharbati, M. N. Soltani Rad, S. Behrouz, F. Emami and A.R. Nekoei, *Opt. Eng*. 2011, **50**, 044002-044006.
46) M. T. Sharbati, F. Panahi, A.R. Nekoei, F. Emami and K. Niknam, *J. Photon. Energy*. 2014, **4**(1), 043599-043599.
47) M. T. Sharbati, Graphene Quantum Dot-Based Organic Light Emitting Diodes, Diss. University of Pittsburgh, 2016.
48) M.T. Sharbati, F. Panahi, A. Gharavi, F. Emami, K. Niknam, Fabrication of a near infrared OLED, in: IEEE LEOS Annual Meeting Conference Proceedings, Turkey, 2009, pp. 90–91.
49) M. T. Sharbati, F. Emami and M. N. Soltani-Rad, Electrical characterization of NIR OLED fabricated using a linear oligomer, Solid-State and Organic Lighting. Optical Society of America, 2010.
50) M. T. Sharbati, F. Emami, A. Gharavi and F. Panahi, Fabrication of a near infrared OLED using a new organic chromophore. In Multitopic Conference, 2009. INMIC 2009. IEEE 13th International (pp. 1-3). IEEE.
51) D. H. Emon, M. Kim, M. T. Sharbati and H. K. Kim, *J. Vac. Sci. Technol. B*, 2016, 34(6), 06KJ01-06KJ06.
52) M. N. Soltani Rad, M. T. Sharbati, S. Behrouz and A. R. Nekoei, *Iranian Journal of Science and Technology*, 2015, **39**(A3), 297-304.
53) Q. Li, T. Y. Luo, M. Zhou, H. Abroshan, J. Huang, H. J. Kim, N. L. Rosi, Z. Shao and R. Jin, *ACS nano*, 2016, **10**, 8385-8393.
54) M. Kidwai, V. Bansal, A. Kumarb and S. Mozumdar, *Green Chem*., 2007, **9**, 742–745.
55) D. Aguilar, M. Contel and E. P. Urriolabeitia, *Chem. Eur. J*., 2010, **16**, 9287–9296.
56) L. Abahmane, J. M. Köhler and G. A. Grob, *Chem. Eur. J*., 2011, **17**, 3005–3010.
57) R. Jin, C. Zeng, M. Zhou and Y. Chen, *Chem. Rev.*, 2016, **116**, 10346–10413.
58) Z. Li, H. Abroshan, C. Liu and G. Li, *Curr. Org. Chem.*, 2017, **21**, 476-488.
59) Y. Chen, C. Liu, H. Abroshan, Z. Li, J. Wang, Li, G. and M. Haruta, *J. Catal.*, 2016, **340**, 287-294.
60) C. Liu, H. Abroshan, C. Yan, G. Li and M. Haruta, *ACS Catal.*, 2015, **6**, 92-99.

61) J. Lin, H. Abroshan, C. Liu, M. Zhu, G. Li and M. Haruta, *J. Catal.*, 2015, **330**, 354-361.
62) Y. Zhu, H. Qian and R. Jin, *Chem. Eur. J.*, 2010, **16**, 11455–11462.
63) G. Li, H. Abroshan, Y. Chen, R. Jin and H. J. Kim, *J. Am. Chem. Soc.*, 2015, **137**, 14295-14304.
64) S. Zhao, R. Jin, H. Abroshan, C. Zeng, H. Zhang, S. D. House, E. Gottlieb, H. J. Kim, J. C. Yang and Jin, R., *J. Am. Chem. Soc*., 2017, **139**, 1077–1080
65) G. Li, H. Abroshan, C. Liu, S. Zhuo, Z. Li, Y. Xie, H. J. Kim, N. L. Rosi and R. Jin,. *ACS Nano*, 2016, **10**, 7998-8005.
66) H. Abroshan, G. Li, J. Lin, H. J. Kim and R. Jin, *J. Catal.*, 2016, **337**, 72-79.
67) W. Li, C. Liu, H. Abroshan, Q. Ge, X. Yang, H. Xu and G. Li, *J. Phys. Chem. C*, 2016, **120**, 10261-10267.
68) C. Yan, C. Liu, H. Abroshan, Z. Li, R. Qiu and G. Li, *Phys. Chem. Chem. Phys.*, 2016, **18**, 23358-23364.
69) G. Li, D. Jiang, C. Liu, C. Yu and R. Jin, *J. Catal*., 2013, **306**, 177–183.
70) G. Li, C. Liu and R. Jin, *Chem. Commun*., 2012, **48**, 12005-12007.
71) Q. Li, A. Das, S. Wang, Y, Chen and R. Jin, *Chem. Commun.*, 2016, **52**, 14298-14301.
72) Z. Wu, D. Jiang, A. K. P. Mann, D. R. Mullins, Z. Qiao, L. F. Allard, C. Zeng, R. Jin and S. H. Overbury, *J. Am. Chem. Soc*., 2014, **136**, 6111–6122.
73) P. G. N. Mertens, J. Wahlen, X. Ye, H. Poelman and D. E. De Vos, *Catal. Lett*., 2007, **118**, 15–21.
74) P. G. N. Mertens, P. Vandezande, X. Ye, H. Poelman, I. F. J. Vankelecom and D. E. De Vos, *Appl. Catal., A: General*, 2009, **355**, 176–183.
75) V. Ponec, *Appl. Catal., A: General*, 1997, **149**, 27–48.
76) A. D. Becke, *Phys. Rev. A*, 1988, **38**, 3098–3100.
77) A. D. Becke, *J. Chem. Phys*., 1993, **98**, 5648–5652.
78) J. C. Burant, Scuseria, G. E.; Frisch, M. J. J. Chem. Phys. 1996, 105, 8969–8972.
79) Gaussian 09, Revision E.01, M. J. Frisch, G. W. Trucks, H. B. Schlegel, G. E. Scuseria, M. A. Robb, J. R. Cheeseman, G. Scalmani, V. Barone, B. Mennucci, G. A. Petersson, H. Nakatsuji, M. Caricato, X. Li, H. P. Hratchian, A. F. Izmaylov, J. Bloino, G. Zheng, J. L. Sonnenberg, M. Hada, M. Ehara, K. Toyota, R. Fukuda, J. Hasegawa, M. Ishida, T. Nakajima, Y. Honda, O. Kitao, H. Nakai, T. Vreven, J. A. Montgomery, Jr., J. E. Peralta, F. Ogliaro, M. Bearpark, J. J. Heyd, E. Brothers, K. N. Kudin, V. N. Staroverov, R. Kobayashi, J. Normand, K. Raghavachari, A. Rendell, J. C. Burant, S. S. Iyengar, J. Tomasi, M. Cossi, N. Rega, J. M. Millam, M. Klene, J. E. Knox, J. B. Cross, V. Bakken, C. Adamo, J. Jaramillo, R. Gomperts, R. E. Stratmann, O. Yazyev, A. J. Austin, R. Cammi, C. Pomelli, J. W. Ochterski, R. L. Martin, K. Morokuma, V. G. Zakrzewski, G. A. Voth, P. Salvador, J. J. Dannenberg, S. Dapprich, A. D. Daniels, Ö. Farkas, J. B. Foresman, J. V. Ortiz, J. Cioslowski and D. J. Fox, Gaussian, Inc., Wallingford CT, 2009.
80) T. H. Jr. Dunning, *J. Chem. Phys.*, 1989, **90**, 1007–1023.
81) P. Fuentealba, H. Preuss, H. Stoll and L. V. Szentpály, *Chem. Phys. Lett*., 1982, **89**, 418–422.
82) G. Igel-Mann, H. Stoll and H. Preuss, *Mol. Phys.*, 1988, **65**, 1321–1328.
83) P. J. Hay and W. R. Wadt, *J. Chem. Phys*., 1985, **82**, 299–310.

84) B. Assadollahzadeha and P. Schwerdtfegera, *J. Chem. Phys*., 2009, **131**, 064306-064311.
85) T. Taketsugu and A. Lyalin, *J. Phys. Chem. Lett*., 2010, *1*, 1752–1757.
86) O. N. Faza, R. Á. Rodríguez and C. S. López, *Theor. Chem. Acc*., 2011, **128**, 647–661.
87) D. Y. Zubarev and A. I. Boldyrev, *J. Phys. Chem. A*, 2009, **113**, 866–868.
88) G. Scalmani and M. J. Frisch, *J. Chem. Phys*., 2010, **132**, 114110–114115.
89) M. Zhu, C. M. Aikens, F. J. Hollander, G. C. Schatz and R. Jin, *J. Am. Chem. Soc*., 2008, **130**, 5883- 5885.
90) J. Li, C. J. Cramer and D. G. Truhlar, *Theor. Chem. Acc*. 1998, **99**, 192-196.
91) J. C. Phillips, R. Braun, W. Wang, J. Gumbart, E. Tajkhorshid, E. Villa, C. Chipot, R. D. Skeel, L. Kale and K. J. Schulten, *Comput. Chem.*, 2005, **26**, 1781-1802.
92) S. E. Feller, Y. H. Zhang, R. W. Pastor, and B. R. Brooks, *J. Chem. Phys.*, 1995, **103**, 4613-4621.
93) T. Darden, D. York and L. J. Pedersen, *Chem. Phys*., 1993, **98**, 10089-10092.
94) J. N. Canongia Lopes, J. Deschamps and A. A. H. Pádua, *J. Phys. Chem. B*, 2004, **108**, 2038-2047.
95) W. L. Jorgensen, D. S. Maxwell and J. Tirado-Rives, *J. Am. Chem. Soc*., 1996, **118**, 11225-11236.
96) P. Giannozzi, S. Baroni, N. Bonini, M. Calandra, R. Car, C. Cavazzoni, D. Ceresoli, G. L. Chiarotti, M. Cococcioni, I. Dabo, A. Dal Corso, S. Fabris, G. Fratesi, S. de Gironcoli, R. Gebauer, U. Gerstmann, C. Gougoussis, A. Kokalj, M. Lazzeri, L. Martin-Samos, N. Marzari, F. Mauri, R. Mazzarello, S. Paolini, A. Pasquarello, L. Paulatto, C. Sbraccia, S. Scandolo, G. Sclauzero, A. P. Seitsonen, A. Smogunov, P. Umari and R. M. Wentzcovitch, *J.Phys.:Condens.Matter*, 2009, **21**, 395502-395521.
97) P. E. Blöchl, *Phys. Rev. B*, 1994, **50**, 17953–17979.
98) J. P. Perdew, K. Burke and M. Ernzerhof, *Phys. Rev. Lett*., 1996, **77**, 3865–3868.
99) O. Lopez-Acevedo, K. A. Kacprzak, J. Akola and H. Häkkinen, *Nat. Chem.*, 2010, **2**, 329–334.
100) C. Liu, S. Lin, Y. Pei and X. C. Zeng, *J. Am. Chem. Soc*., 2013, **135**, 18067–18079.
101) O. Lopez-Acevedo and H. Hakkinen, *Eur. Phys. J. D*, 2011, **63**, 311–314.
102) M. W. Heaven, A. Dass, P. S. White, K. M. Holt and R. W. Murray, *J. Am. Chem. Soc*., 2008, **130**, 3754–3755.
103) T. Welton, Green Chem., 2011. **13**, 225.
104) M. J. Earle and K. R. Seddon, *Pure Appl. Chem*., 2000, **72**, 1391–1398.
105) J. Dupont and P. A. Z. Suarez, *Phys. Chem. Chem. Phys*.,2006, **8**, 2441-2452.
106) S. D. Zhu, Y. X. Wu, Q. M. Chen, Z. N. Yu, C. W. Wang, S. W. Jin, Y. G. Ding and G. Wu, Green Chem., **8**, 325- 327 (2006).
107) N. V. Plechkova and K. R. Seddon, *Applications of Ionic Liquids in the Chemical Industry*, *Chem. Soc. Rev*., 2008, **37**, 123-150.
108) T. Welton, Chem. Rev., **99**, 2071-2084 (1999).
109) C. Chiappe and D. Pieraccini, *J. Phys. Org. Chem.*, 2005, **18**, 275-297.
110) M. Ramdin, T. W. de Loos and T. J.H. Vlugt, *Ind. Eng. Chem. Res*., 2012, **51**, 8149–8177.
111) X. Li, L. Zhang, Y. Zheng and C. Zheng, *Ind. Eng. Chem. Res*., 2015, **54**, 8569–8578.

112) M. Garcia-Melchor, A. A. C. Braga, A. Lledos, G. Ujaque and F. Maseras, *Acc. Chem. Res*., 2013, **46**, 2626-2634.
113) G. B. Smith, G. C. Dezeny, D. L. Hughes, A. O. King and T. R. Verhoeven, *J. Org. Chem*., 1994, **59**, 8151-8156.
114) U. Christmann and R. Vilar, *Angew. Chem., Int. Ed*., 2005, **44**, 366-374.
115) S. Carrettin, J. Guzman and A. Corma, *Angew. Chem. Int. Ed*., 2005, **44**, 2242-2245.
116) J. P. Canal, T. Ramnial, D. A. Dickie and J. A. C. Clyburne, *Chem. Commun*., 2006, **17**, 1809-1818.
117) S. Sowmiah, V. Srinivasadesikan, M. C. Tseng and Y. H. Chu, *Molecules*, 2009, **14**, 3780-3813.
118) D. Andrae, U. Haussermann, M. Dolg, H. Stoll and H. Preuss, *Theor. Chim. Acta*, 1990, **77**, 123-141.
119) M. Dolg, U. W edig, H. Stoll and H. Preuss, *J. Chem. Phys*., 1987, **86**, 866-872.
120) T. Morita, B. M. Ladanyi and J. T. Hynes, *J. Phys. Chem*., 1989, **93**, 1386.
121) W. J. Plieth, *J. Phys. Chem*., 1982, **86**, 3166-3170.
122) O. S. Ivanova and F. P. Zamborini, *Anal. Chem*., 2010, **82**, 5844-5850.
123) O. S. Ivanova and F. P. Zamborini, *J. Am. Chem. Soc*., 2010, **132**, 70-72.
124) R. A. Masitas and F. P. Zamborini, *J. Am. Chem. Soc*., 2012, **134**, 5014-5017.
125) A. Henglein, *J. Phys. Chem*., 1993, **97**, 5457-5471.
126) R. Guo and R. W. Murray, *J. Am. Chem. Soc*., 2005, **127**, 12140–12143.
127) C. M. Aikens, *J. Phy. Chem. Lett*. 2010, **1**, 2594–2599.
128) A. Das, C. Liu, C. Zeng, G. Li, T. Li, N. L. Rosi and R. Jin, R, *J. Phys. Chem. A*, 2014, **118**, 8264–8269.
129) G. Henkelman, B. P. Uberuaga and H. A Jonsson, J. Chem. Phys., 2000, **113**, 9901−9904.

Chapter 4: *Mechanistic insights into preparation of single doped gold nanoparticles*

4.1 Abstract

Doping of metal nanoparticles with a specific number of hetero-metal atoms at specific positions has been a major challenge. We utilize density functional theory calculations to offer atomistic insight into preparation of gold nanoclusters doped with a single metal atom. The formation of rod shaped Au_{24} nanoparticle with a central cavity from its parent Au_{25} nanoparticle in the presence of phosphine ligands is studied. The Au_{24} nanoparticle is shown to be able to host a single silver (Ag) or copper (Cu) atom via a highly controllable fashion. The single Ag and Cu dopants are found to prefer different sites of the nanocluster to occupy. The preferred site for the dopants are mainly determined by their initial interactions with the protecting ligands. While doping of gold nanoparticles with Ag or Cu typically results in alloys with a non-specific number (i.e. a distribution) of Ag or Cu dopants, in this work a new strategy for single doping is offered based on preparation of hollow nanoparticles.

Keywords: Nanoclusters, Single Doping, DFT, NEB

4.2 Introduction

The research on metal alloy nanoparticles represents one of the key technology efforts for development of green sources of energy with a wide range of applications, including fuel cells,[1-4] Li batteries,[5] and catalysis.[6] A special attention should be given to controlling composition, size, and structure of alloy nanoparticles for systematic development of their properties toward target activity and selectivity.[7-11] The composition of an alloy in bulk limit is usually deemed to be the most important parameter to determine the alloy properties.[11] However, as the size of an alloy decreases, the physical, chemical, and catalytic properties of the alloy are not only dependent on the composition, but also the size, shape, and atomic configuration. For example, catalytic performance is shown to be influenced by surface atomic arrangement or coordination.[12-14]

Single-atom doping of nanoparticles is a rational approach to develop and design novel bi-functional heterogeneous catalysts with superior or new properties.[15] For example, previous studies demonstrated that thermal stability, optical, and catalytic properties of gold nanoparticles are significantly enhanced if the particles are doped by a single atom of Pd, Pt, Cd, and Hg.[16-20] Unfortunately, single-atom doping of gold nanoparticles is mainly limited to the use of heterometals from a different group of elements rather than the group IB (i.e., Cu and Ag). The synthesis of gold nanoparticles in the presence of Cu or Ag atom leads to the formation of a range of alloy nanoparticles with various numbers of Cu or Ag dopants, i.e., $Au_{25-x}Cu_x$ and $Au_{25-x}Ag_x$ with $0 < x < 25$.[21-25] This is mainly because of similar configuration of outmost electrons ($d^{10}s^1$) of Cu and Ag with Au.

Although the similarity in electronic structure of Ag and Cu with Au ($d^{10}s^1$) makes it difficult to dope a single-atom of coper and silver into gold nanoparticles, they should be

able to fill easily a pre-formed vacancy within the gold nanoparticle. We rationalize this method can overcome the limitation rising from the similar electron configuration of the same group metals. In this regard, we note Das et al. reported $[Au_{24}(PPh_3)_{10}(SC_2H_4Ph)_5Cl_2]^+$ nanoparticles with a central vacancy can be synthesized via thermal treatment of $[Au_{25}(PPh_3)_{10}(SC_2H_4Ph)_5Cl_2]^{2+}$ nanoparticles in the presence of excess triphenylphosphine (PPh_3).[26] Single crystal X-ray diffraction analysis shows that the $[Au_{24}(PPh_3)_{10}(SC_2H_4Ph)_5Cl_2]^+$ nanoparticle is composed of two incomplete icosahedral Au_{12} units that are linked by five thiolate linkages.[26] The later Au_{24} nanocluster lacks the central Au atom in comparison to the $[Au_{25}(PPh_3)_{10}(SC_2H_4Ph)_5X_2]^{2+}$ nanocluster. The vacancy shows to exert a major influence on the optical properties of the nanoparticle.[26] Re-filling the central vacancy of the Au_{24} nanoparticle by a metal atom from IB group (i.e., Cu, Ag, and Au) would be prudent to consider. It is expected that single-atom doping by Cu or Ag can be achieved by using the Au_{24} as a template because this nanocluster possesses *only* one vacancy. Furthermore, via a sequential hollowing and re-filling of resultant nanocluster, atom-by-atom doping in a highly controlled fashion is achievable. Using density functional theory (DFT) calculations, this chapter presents the shuttling pathway of an Ag or Cu atom in to gold nanoparticles. The Au_{24} nanocluster is used as a model for this study.

4.3 Computational Method

DFT calculations were carried out using the Quantum Espresso package.[27] The Projector Augmented-Wave (PAW) method was applied to describe the interaction between the electrons and nuclei.[28] The Perdew–Burke–Ernzerhof (PBE) form of the

generalized gradient approximation was employed for electron exchange and correlation.[29] The gold cluster was placed at the center of a cubic box of 30.0 Å × 30.0 Å × 30.0 Å. The kinetic energy cutoff was chosen to be 450 eV and integration in the reciprocal space was carried out at the Γ k-point of the Brillouin zone. The nudged elastic band (NEB) approach was used for finding minimum energy path of transitions.[30]

4.4 Results and Discussions

Experimental studies of Prof. Jin's group showed that reaction of Au_{24} with Au(I)Cl readily restores Au_{25} within a few seconds. Results show that addition of CuCl or AgCl to a solution of Au_{24} leads to the formation of new products doped with Cu or Ag. X-ray crystallography analysis show that Cu can occupy two different types of sites: *i*) at the apex of the rod-shaped nanoparticle, and *ii*) at the waist position of the nanoparticle, while silver was only found at the apex of the nanoparticle (Figure 4.1). Interestingly, the central position of the nanoparticle is 100% occupied by gold atom in both products, rather than a Cu or Ag atom as one would expect since the central vacancy is ready for filling.

The experimental results clearly demonstrate the success in single atom doping into the gold nanoparticle. The reactions of Au_{24} with AgCl and CuCl show that the copper or silver atom does not directly take the central empty position as one would initially expect, instead the Cu or Ag dopant should squeeze one surface gold atom into the central vacancy. To map out the mechanistic details, we carried out DFT simulations on the formation of Au_{24} from the Au_{25} nanoparticle and the back filling of Au_{24} to form MAu_{24} (M=Cu or Ag).

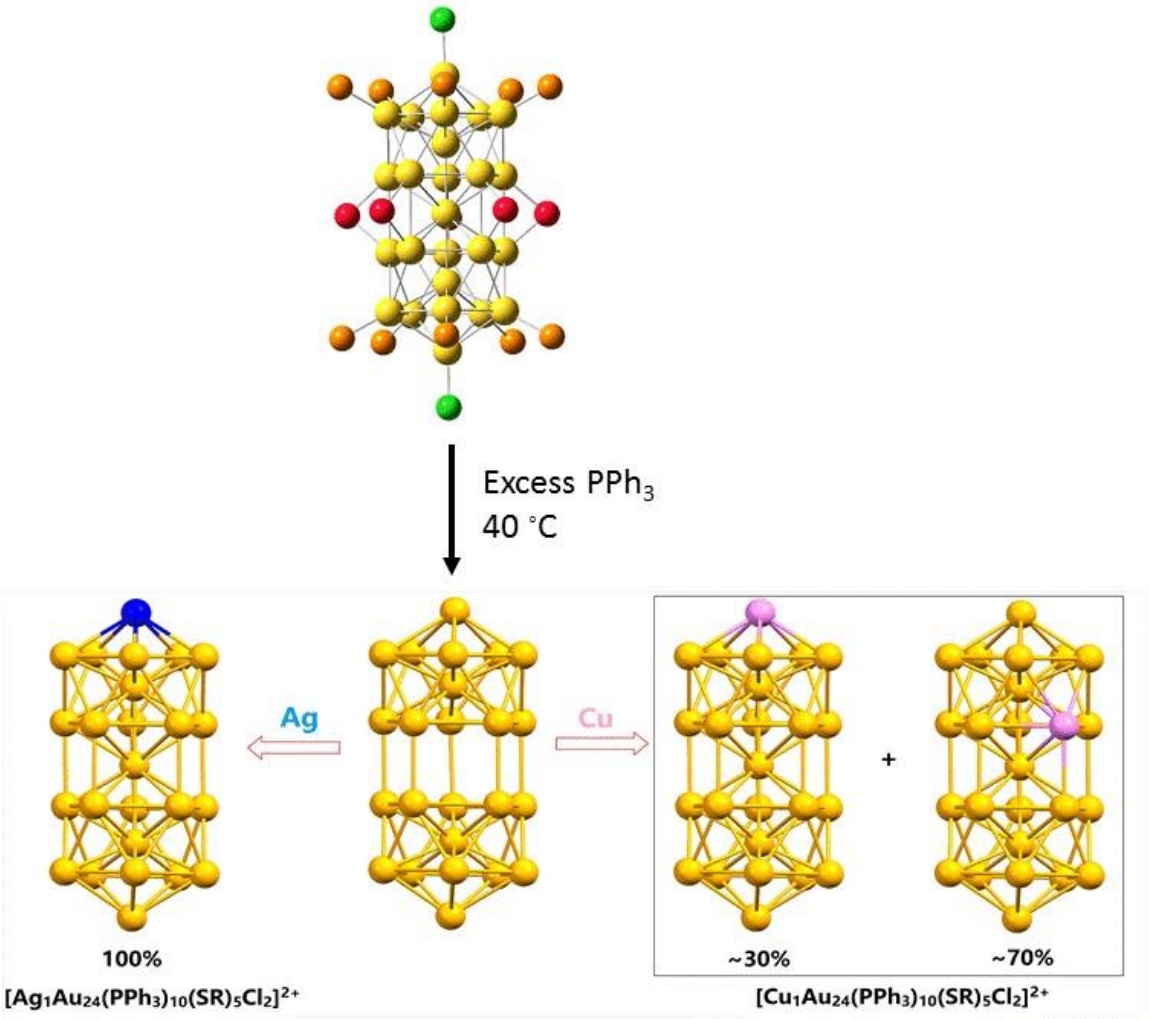

Figure 4.1. Shuttling out of the central gold atom of $[Au_{25}(PPh_3)_{10}(SR)_5Cl_2]^{2+}$ nanoparticle to form24-atom hollow gold nanoparticle. Shuttling in one Ag or Cu atom into the Au_{24} nanoparticle: pathways of single Ag/Cu entering the hollow Au_{24} nanoparticle. Color codes: Au, yellow; Ag, blue; Cu, orange; S, red; Cl, green; P, orange. Other non-metal atoms and bonds are not shown for clarity. In the lower panel, the protecting ligands are skipped for clarity.

4.4.1 Formation mechanism of the hollow Au_{24}. As mentioned above, it is found experimentally that excess phosphine ligands play a key role in the formation of hollow Au_{24} nanoparticle from its parent Au_{25} nanoparticle. DFT calculations were performed using $[Au_{25}(PH_3)_{10}(SH)_5Cl_2]^{2+}$ as a model of the experimental nanoparticle by simplifying

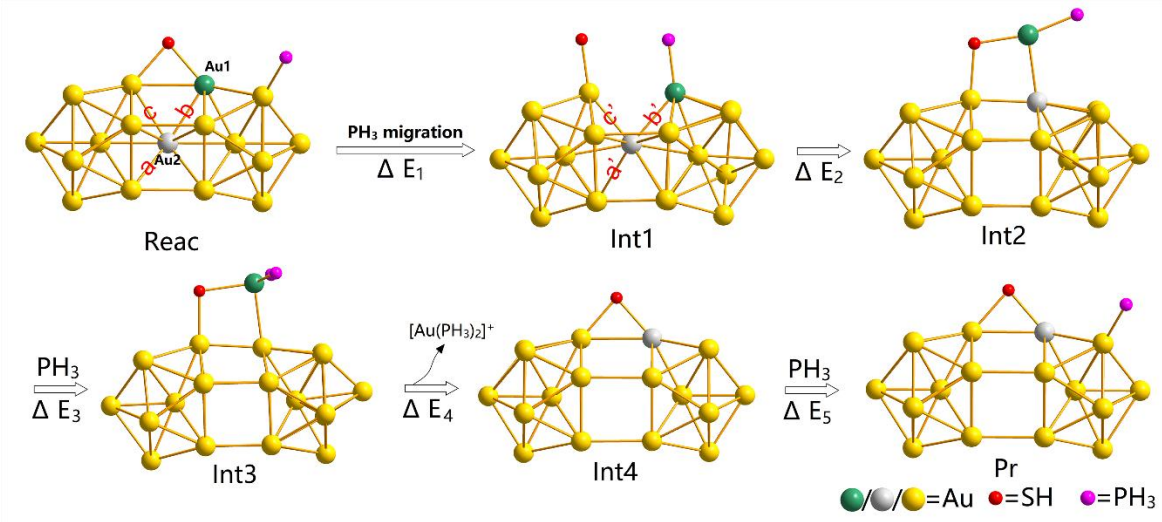

Figure 4.2. Mechanisms for the formation of hollow Au_{24} cluster. The values of interatomic distances are *a* = *b* = *c* = 2.97, *a*' = 3.23, *b*' = 2.90, and c' = 2.86 Å. DFT results show ΔE_1 = 25.9, ΔE_2 = 7.1, ΔE_3 = -5.2, ΔE_4 = 34.4, and ΔE_5 = -30.7 kcal/mol. Color codes: Au1, green; Au2, gray; other Au, yellow; S, red. Other atoms and bonds are not shown for clarity.

PPh_3 to PH_3 and SC_2H_4Ph to SH. Results show that adsorption of a PH_3 onto a gold atom located at the waist position (Au1, Figure 4.2, green ball) of the nanoparticle is the most likely mechanism to initiate the reaction. A PH_3 of the rod via a migration process (Reac → Int1) may form a bond with the Au1. Of note, the Au—PPh_3 bond is flexible, which allows rapid exchange between the free and bound PPh_3.[31]

Upon the formation of Au—PH_3 bond and subsequent Au—S bond breaking (Int1, Figure 4.2), the gold atom at the center of the nanoparticle (Au2, Figure 4.2, grey ball) dislocates towards the surface of the nanoparticle, evidenced by changes in the Au—Au atomic distances (Figure 4.2). The Au1—Au2 bond distance becomes 2.90 Å (*b*' in Figure 4.2) which is considerably less than the bond distance between Au2 and gold atoms located at the lower side of the waist position (*a'* = 3.23 Å, Figure 4.2). Next, the Au2 is completely pulled up to the surface of the nanoparticle (Int1 → Int2). In turn, this exposes the Au1 to

PH_3 ligands in the reaction medium to form $Au(PH_3)_2$ on the surface of the nanoparticle (Int2 → Int3). The $Au(PH_3)_2^+$ moiety eventually detaches from the nanoparticle to result in the $[Au_{24}(PPh_3)_9(SR)_5Cl_2]^+$ nanoparticle (Int3 → Int4). The generation of $Au(PPh_3)_2^+$ ion is indeed experimentally confirmed later by our experimental collaborators using ESI-MS. Finally, the as-formed $[Au_{24}(PPh_3)_9(SR)_5Cl_2]^+$ nanoparticle reacts with a PH_3 to result in the hollow $[Au_{24}(PPh_3)_{10}(SR)_5Cl_2]^+$ nanoparticle (Int4 → Pr).

4.4.2 Formation mechanism of MAu_{24} (M=Cu or Ag). The MAu_{24} nanoparticle has five non-equivalent types of metal positions (P1 to P5 as indicated in Figure 4.3a). Geometry optimizations of MAu_{24} with M located at the different positions show that both Cu and Ag energetically disfavor to occupy positions of P2 and P4 (Table 4.1), in good agreement with the X-ray crystallography analysis. However, relative energetics of the nanoparticles with M at positions P1, P3, and P5 are not in line with the experimental results. DFT results show that Cu prefers to occupy the sites in the order of P1 ≈ P5 > P3, while for the case of Ag, the order is P5 > P3 > P1 (Table 4.1). For completeness, the Grimme-D2 (36) and the Exchange-hole dipole-moment (XDM) methods were used to incorporate the van der Waals (vdW) interactions into the systems.[32-34] As Table 4.1 shows, DFT-D2 and DFT-XDM calculations yield almost the same conclusions as DFT does. The X-ray crystallography analysis indicates that Ag prefers to locate at site P1 and Cu at P3 (Figure 4.1); therefore, our calculations reveal that in addition to the relative stability of the nanoparticles based on their energetics, other factors such as reaction kinetics and entropy effects (ten P3 sites vs two P1 sites) also play significant roles in the formation of MAu_{24}.

We next considered whether the location of incoming M (Cu or Ag) is dictated by the initial interaction of M^+ with the capping ligands of the nanoparticle (-SR and Cl-Au, see Figure

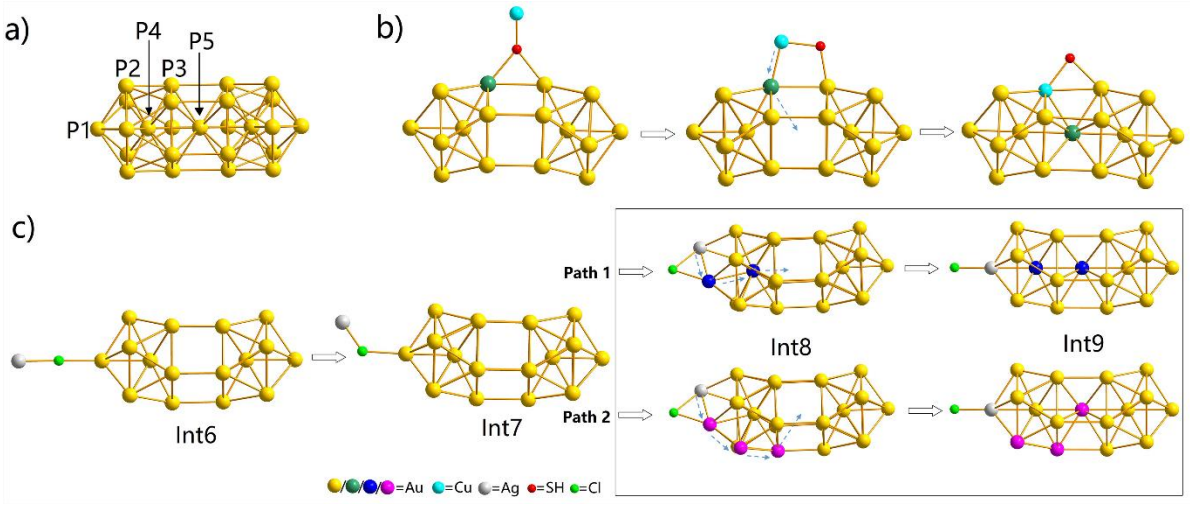

Figure 4.3. a) Designation of P1 to P5 sites in the MAu_{24} structure. DFT-calculated mechanisms for MAu_{24} (M = Cu or Ag) formation with M at b) waist and c) apex positions. Color code: Au, yellow; S, green; Cl, cyan; Ag, blue; Cu, orange. Other atoms and bonds are not shown for clarity.

Table 4.1. Energy (kcal/mol) of optimized $AgAu_{24}$ nanoclusters with Ag located at the different positions (see Figure 4.3a). The energy of the most stable system is set to 0.00. Energy of the other systems are reported relative to the most stable system. Results of DFT with van der Waals (vdW) corrections using the Grimme-D2 and the Exchange-hole dipole-moment (XDM) methods are also presented.

Position	*DFT*	*DFT-D2*	*DFT-XDM*
P1	5.69 (0.00)	2.89 (2.44)	6.12 (0.00)
P2	9.09 (6.53)	7.91 (7.64)	9.62 (6.77)
P3	3.97 (2.29)	4.09 (6.42)	3.87 (2.04)
P4	20.12 (10.22)	16.83 (8.42)	21.24 (9.28)
P5	0.00 (0.22)	0.00 (0.00)	0.00 (0.13)

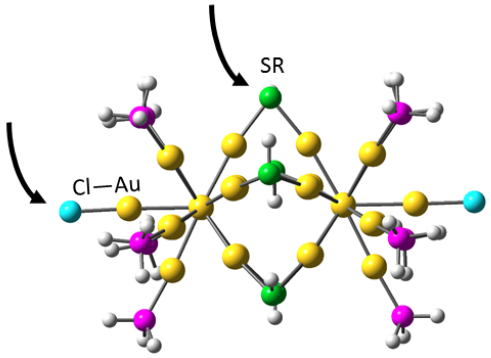

$\Delta E(Ag^+) = E_{Ag+.....Cl—Au} - E_{Ag+ .....SR} = -9.6$ kcal/mol

$\Delta E(Cu^+) = E_{Cu+.....Cl—Au} - E_{Cu+ .....SR} = -8.0$ kcal/mol

Figure 4.4. There are two possible sites for M-Cl or M^+ (M = Cu or Ag) with the capping ligands of the nanoparticle. Color code: Au, yellow; S, green; Cl, cyan; P, pink.

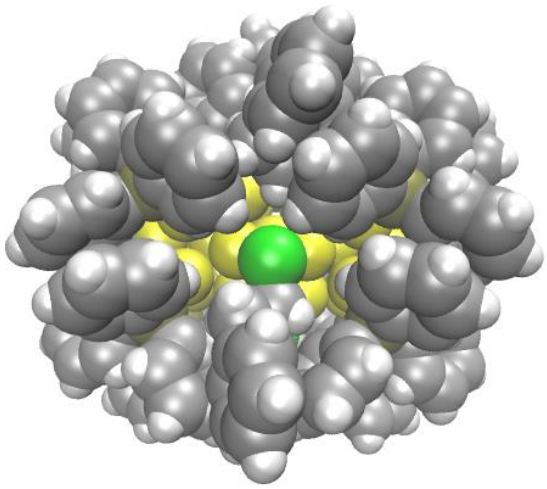

Figure 4.5. The bigger vdW radii of Ag (in comparison to that of Cu) prevents the silver atoms to interact efficiently with S atom (green) of –SR groups.

4.4). Interaction energy of Ag^+ and Cu^+ with Cl-Au is found to be 9.6 and 8.0 kcal/mol, respectively, more favorable than those with –SR. These results show that the interaction of Cl-Au with Ag is stronger than with Cu. This may indicate the single atom transfer and its possible location is determined by the interaction of the M (Cu or Ag) with capping ligands of the nanoparticle, in agreement with our experimental trend. In addition,

compared to Cu, the larger vdW radius of Ag also prevents the silver atoms from interacting efficiently with –S– due to steric hindrance. Of note, the protecting ligands of the nanoparticle make the particle surface considerably packed, which causes high spatial hindrance for Ag^+ to pass through and approach the –SR group (see Figure 4.5). However, Cu has a smaller vdW radius and can interact with surface thiolate ligand which eventually pushes a gold atom at the waist position into the vacancy at the center of Au_{24} to form $CuAu_{24}$.

Further, we consider possible mechanisms to from $AgAu_{24}$ with Ag located at the apical site of the nanoparticle. An Ag^+ may interact with the Cl atom at the apex of the nanoparticle (Int6, Figure 4.3c), which eventually moves to interact with three gold atoms located at the apical as well as the end positions of the nanoparticle (Int6 → Int7 → Int8, Figure 4.3c). There are two possible pathways for the Ag at this position to locate at the apical site by squeezing a gold atom at sites of I) icosahedral center (Figure 4.3c, Path1, shown by blue arrows) and II) waist (Figure 4.3c, Path 2, shown by red arrows). Our calculations using the nudged elastic band (NEB) approach[30] show barrier energy of mechanism II is 19.8 kcal/mol lower than that for mechanism I. This result indicates metal mobility is most likely to happen through the surface of the nanoparticle rather than the core of the icosahedron, in agreement with the mechanism for the Au_{24} formation.

4.5 Conclusion

In summary, we have successfully demonstrated the single-metal-atom shuttling in atomically precise metal nanoparticle, i.e., the conversion between Au_{24} and Au_{25}

nanoparticles. Our results provide a clear map of how single metal atom transfer occurs between two atomically precise nanoparticles. Based on the theoretical results, the driven force of single atom transfer is caused by the ligand. i.e., the free PPh_3 for the shuttling-out process, and the surface –Cl and –SR ligands for the shuttling-in process. The stronger binding between Ag and -Cl compared with Ag-SR leads to the exclusive Ag atom doping at the apex of the nanoparticle, while the similar energy of Cu-Cl and Cu-SR leads to the Cu atom doping into both the apex and waist positions. This work provides fundamental understanding of how to shuttle single atom in and out of metal nanoparticles by a chemical method. The ligand-induced single atom shuttling process also provides a new strategy for controlling the doping position and the doping number of heteroatoms in alloy nanoparticles.

4.6 Acknowledgments

This work was supported in part by NSF Grant No. CHE-1223988.

4.7 References

1) C. Baldizzone, S. Mezzavilla, H. W. P. Carvalho, J. C. Meier, A. K. Schuppert, M. Heggen, C. Galeano, J.-D. Grunwaldt, F. Schüth and K. J. Mayrhofer, *Angew. Chem., Int. Ed.*, 2014, **53**, 14250−14254.
2) V. R. Stamenkovic, B. S. Mun, M. Arenz, K. J. J. Mayrhofer, C. A. Lucas, G. Wang, P. N. Ross and N. M. Markovic, *Nat. Mater*., 2007, **6**, 241−247.
3) Y.-J. Wang, N. Zhao, B. Fang, H. Li, X. T. Bi, H. Wang, *Chem. Rev*., 2015, **115**, 3433−3467.
4) G. Hu, F. Nitze, E. Gracia-Espino, J. Ma, H. R. Barzegar, T. Sharifi, X. Jia, A. Shchukarev, L. Lu, C. Ma, G. Yang and T. Wågberg, *Nat. Commun*., 2014, **5**, 5253.
5) M. N. Obrovac and V. L. Chevrier, *Chem. Rev*., 2014, **114**, 11444−11502.
6) K. Maeda, K. Teramura, H. Masuda, T. Takata, N. Saito, Y. Inoue and K. J. Domen, *Phys. Chem. B*, 2006, **110**, 13107−13112.

7) C. Cui, L. Gan, H. Li, S. Yu, M. Heggen and P. Strasser, *Nano Lett*., 2012, **12**, 5885−5889.
8) C. Cui, L. Gan, M. Heggen, S. Rudi and P. Strasser, *Nat. Mater*., 2013, **12**, 765−771.
9) H. Li, C. Cui, S. Zhao, H. Yao, M. Gao, F. Fan and S. Yu, *Adv.Energy Mater*., 2012, **2**, 1182−1187.
10) S. Rawalekar and T. Mokari, *Adv. Energy Mater*., 2013, **3**, 12−27.
11) H. You, S. Yang, B. Ding and H. Yang, *Chem. Soc. Rev*., 2013, **42**, 2880−2904.
12) J. Zhang, K. Sasaki, E. Sutter and R. R. Adzic, *Science*, 2007, **315**, 220–222.
13) E. Casado-Rivera, D. J. Volpe, L. Alden, C. Lind, C. Downie, T. Vazquez-Alvarez, A. C. D. Angelo, F. J. DiSalvo and H. D. Abruna, *J. Am. Chem. Soc*., 2004, **126**, 4043–4049.
14) V. R. Stamenkovic, B. Fowler, B. S. Mun, G. Wang, P. N. Ross, C. A. Lucas and N. M. Markovic, *Science*, 2007, **315**, 493–497.
15) H. L. Tierney, A. E. Baber, J. R. Kitchin and E. C. H. Sykes, *Phys. Rev. Lett.*, 2009, **103**, 246102-246104.
16) Y. Negishi, W. Kurashige, Y. Niihori, T. Iwasa and K. Nobusada K, *Phys. Chem. Chem. Phys.*, 2010, **12**, 6219-6225.
17) H. Qian, D. Jiang, G. Li, C. Gayathri, A. Das, R. G. Gil and R. Jin, *J. Am. Chem. Soc.*, 2012, **134**,16159-16162.
18) S. Wang, Y. Song, S. Jin, X. Liu, J. Zhang, Y. Pei, X. Meng, M. Chen, P. Li and M. Zhu, *J. Am. Chem. Soc.*, 2015, **137**, 4018-4021.
19) S. Xie, H. Tsunoyama, W. Kurashige, Y. Negishi and T. Tsukuda, *ACS Catal.*, 2012, **2**, 1519-1523.
20) H. Deng, S. Wang, S. Jin, S. Yang, Y. Xu, L. Liu, J. Xiang, D. Hu and M. Zhu, *Gold Bull.*, 2015, **48**, 161-167.
21) Y. Negishi, T. Iwai and M. Ide, *Chem. Commun.*, 2010, **46**, 4713-4715.
22) Y. Negishi, K. Munakata, W. Ohgake and K. Nobusada, *J. Phys. Chem. Lett.*, 2012, **3**, 2209-2214.
23) M. Walter and M. Moseler, *J. Phys. Chem. C*, 2009, **113**, 15834-15837.
24) D. Jiang and S. Dai, *Inorg. Chem.*, 2009, **48**, 2720-2722.
25) E. Gottlieb, H. Qian and R. Jin, *Chem. –Eur. J.*, 2013, **19**, 4238-4243.
26) A. Das, T. Li, K. Nobusada, Q. Zeng, N. L. Rosi and R. Jin, *J. Am. Chem. Soc.*, 2012, **134**, 20286-20289.
27) P. Giannozzi, S. Baroni, N. Bonini, M. Calandra, R. Car, C. Cavazzoni, D. Ceresoli, G. L. Chiarotti, M. Cococcioni, I. Dabo, A. Dal Corso, S. Fabris, G. Fratesi, S. de Gironcoli, R. Gebauer, U. Gerstmann, C. Gougoussis, A. Kokalj, M. Lazzeri, L. Martin-Samos, N. Marzari, F. Mauri, R. Mazzarello, S. Paolini, A. Pasquarello, L. Paulatto, C. Sbraccia, S. Scandolo, G. Sclauzero, A. P. Seitsonen, A. Smogunov, P. Umari and R. M. Wentzcovitch, *J.Phys.:Condens.Matter*, 2009, **21**, 395502-395521.
28) P. E. Blöchl, *Phys. Rev. B*, 1994, **50**, 17953–17979.
29) J. P. Perdew, K. Burke and M. Ernzerhof, *Phys. Rev. Lett*., 1996, **77**, 3865–3868.
30) G. Henkelman, B. P. Uberuaga and H. Jonsson, *J. Chem. Phys*., 2000, **113**, 9901−9904.
31) J. Petroski, M. H. Chou and C. Creutz, *Inorg. Chem.*, 2004, **43**, 1579-1599.
32) S. J. Grimme, *Comput. Chem.*, 2006, **27**, 1787–1799
33) A. D. Becke and E. R. Johnson, *J. Chem. Phys.*, 2007, **127**, 154108-154116
34) A. Otero de la Roza and E. R. Johnson, *J. Chem. Phys.*, 2012, **136**, 174109-174118.

Chapter 5: *Mechanistic insights into organocatalytic properties of imidazolium-based ionic liquids*

5.1 Abstract

This chapter presents molecular insights into promotional effects of imidazolium-based ionic liquids on transesterification of cellulose. As a model for the reaction, we studied methanol transesterification with isopropenyl acetate in the presence of dialkylimidazolium acetate. Results show that acetate anions of the IL play the most essential role to promote chemical rate of the reaction. The mechanistic insights offered via this study could lead our experimental collaborators in Kanazawa University to optimize protocol of IL-catalyzed transesterification reactions with a considerable high conversion rate.

Keywords: organocatalysis, imidazolium-based ionic liquid, transesterification, cellulose

5.2 Introduction

Biomass-derived chemicals have received much attention because of ever growing importance of "Sustainability" and "Green Chemistry" in the chemical industry.[1, 2] Wood-biomass, also known as lignocellulose, is one of the most important biomass-based resources for chemical feedstock due to its natural availability in large scales. Although cellulose, hemicellulose, and lignin comprise the main components of lignocellulose, cellulose is commonly considered as the most important chemical resource. This is mainly due to higher abundance of cellulose and its clear and homogenous structures that enable a rational molecular design of derivatives materials. Unfortunately, application of cellulose and its derivatives has been minimal because of their processing difficulties, including poor solubility in a wide range of aqueous and organic solvents.

Ionic liquids have received overwhelming interests in biomass processing ever since Rogers et al. reported the solubility of cellulose in ILs.[3-5] Because of ILs' unique properties, they have been extensively used in organocatalytic synthetic chemistry.[6-13] A key advantage of application of ILs in synthetic chemistry is their simultaneous roles as solvents for reactants and catalysts for chemical transformation.[13] For example, Kakuchi et al. reported that 1-ethyl-3-methylimidazolium acetate (EmimOAc) is able to not only facilitate cellulose solubility but also accelerate transesterification reaction of cellulose with isopropenyl acetate (IPA, Figure 5.1).[14] The reported synthetic protocol offers cellulose transesterification reactions in the absence of any activating reagents. However, a fairly large amount of reactants is required in comparison to the reaction in the presence of activated chemical reagents. As this significantly limits the applicability of ILs in

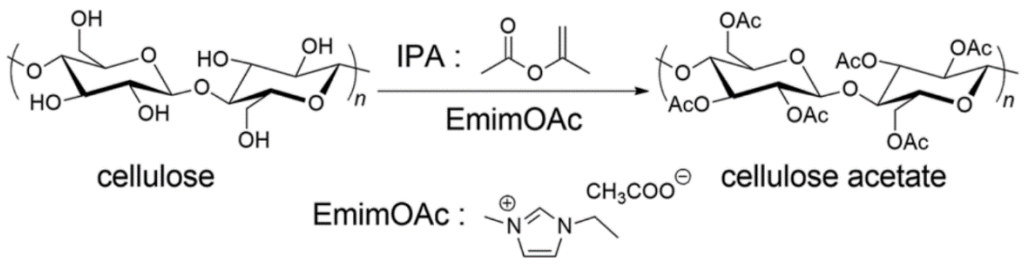

Figure 5.1. Schematic representation of the transesterification reaction of cellulose in EmimOAc.[15]

synthetic polymer chemistry, it is both desirable and valuable to improve the reaction conditions for practical applications.

A molecular understanding of transesterification reaction in the presence of imidazolium-based ionic liquids is required to improve the synthetic protocol,[14] Mechanistic insights into reactions can shed lights on potentials roles played by anions and cations, which in turn help to find greener conditions for cellulose modification reactions. Herein, we investigate the catalytic activities of imidazolium-based ionic by employing a model reaction system. Our results indicate the promotional effects of the ILs is mainly due to the hydrogen bond interactions of anions with hydroxyl group of cellulose. Based on this understanding, our experimental collaborators in Kanazawa University in Japan rationally optimize the transesterification reaction processes.[15]

5.3 Computational Method

Density functional theory (DFT) calculations were performed to investigate possible mechanisms of transesterification reaction promoted by imidazolium-based ionic liquids.

The Synchronous Transit-Guided Quasi-Newton (STQN) Method is used for locating of transition states.[16,17] The partial atomic charges are determined with the electro-static potential (ESP) method.[18-20] The Gaussian 09 package is used for geometry optimizations with the B3LYP hybrid density functional and 6-31G(d,p) basis sets.[21-24]

5.4 Results and Discussions

For efficient calculations, the imidazolium cation and the alcohol were modelled as 1,3-dimethylimidazolium (DMIM) and methanol, respectively. We first investigated the reaction pathway in the absence of the ILs. DFT results indicate that barrier height for the reaction is rather high, 30.9 kcal/mol (Reac → 1TS1, Figure 5.2), which explains no conversion in the absence of catalysts. Next, we studied the effect of IL anion, acetate, on the energy profile of the reaction. As illustrated in Figure 5.2, acetate interacts strongly with proton of methanol's hydroxy group (26.5 kcal/mol, Reac → 1Int1). This leads to significant elongation of O—H bond by 0.04 Å, which in turn changes the partial charge of the alcohol's oxygen from -0.60 to -0.70 (Figure 5.3). We would thus expect that the alcohol's oxygen becomes "activated" and hence enabled to react with carbonyl group of the ester. As expected, DFT predicts that the barrier height for the reaction between the $[CH_3OH\ldots OAc]^-$ complex and ester is 2.6 kcal/mol, markedly lower than 30.9 kcal/mol in the absence of the anion above (1Int1 → 1TS2, Figure 5.2). This result is in good agreement with the experimental observation of our collaborators,[15] i.e., an increase in the basicity of IL anions leads to a higher reaction conversion (Table 5.1).[15] The transition state

1TS2 eventually converts to products through an exothermic step of 1.1 kcal/mol (1TS2 → Pro).

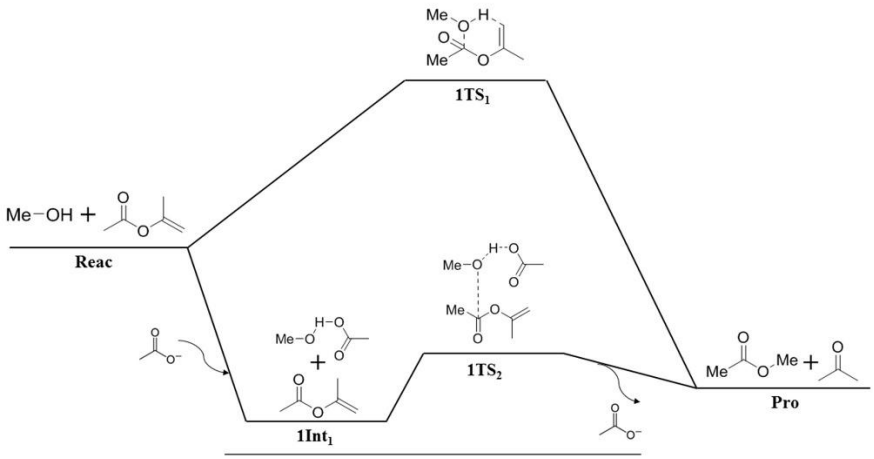

Step	ΔE(kcal/mol)
Reac → $1TS_1$	+30.9
$1TS_1$ → Pro	-55.9
Reac → $1Int_1$	-26.5
$1Int_1$ → $1TS_2$	+2.6
$1TS_2$ → Pro	-1.1

Figure 5.2. Proposed reaction Mechanism 1 for transesterification reactions in the absence (upper pathway) and presence (lower pathway) of acetate anion of the ionic liquids along with the calculated energies for different elementary steps.

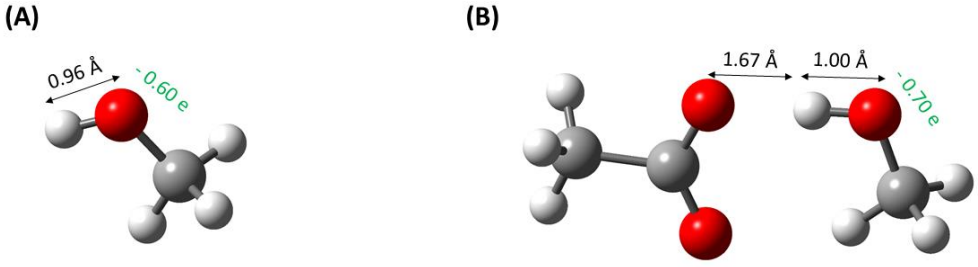

Figure 5.3. Optimized structure of (A) an isolated methanol molecule and (B) an acetate-methanol complex. Color code: O, C and H atoms are shown in red, dark grey, and light grey, respectively. The partial charge for the oxygen atom of methanol is given in green.

Table 5.1. An effect of anion structures on the transesterification reaction of 2-PA and IPA catalyzed by imidazolium based ILs with diverse anions.[a, 15]

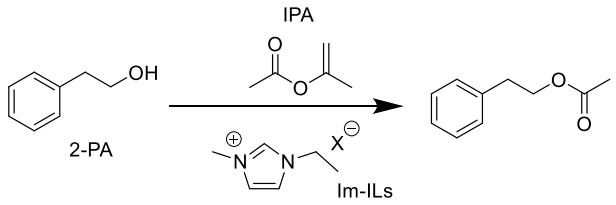

[2-PA]/[IPA]/[Im-ILs] = 1/1.5/0.1

Run	*Anion (X^-)*	pK_a[b]	*Conv. (%)*[c]
1	CH_3COO^-	12.3	63
2	Cl^-	1.8	1
3	Br^-	0.9	1
4	CF_3COO^-	3.45	2

[a]The reaction conditions for the transesterification reaction of PA and IPA are as follows; neat condition; the reaction was conducted for 16 hours; Ar atmosphere. [b]The pK_a values in DMSO.[25] [c]Determined by 1H NMR in CDCl3.

Turning to imidazolium cations, we mainly focus on the acidic hydrogen at the C-2 position, which tends to interact strongly with negatively charged sites compared to other ring or alkyl chain hydrogen atoms. As demonstrated above, it plays a significant role in transesterification reaction kinetics, whereas chemical substitutions at other positions have only a minor effect. DFT predicts that the interaction of the acidic proton at the C-2 position of DMIM with the carbonyl oxygen of the ester induces a pronounced conformational deformation of the ester's skeleton–i.e., the latter changes from a planar to a twisted geometry (Figure 5.4). As such, the cation-ester interaction via the acidic proton and carbonyl oxygen is expected to exert a considerable influence on the reaction energetics (Figure 5.5). According to DFT calculations, this interaction reduces the transesterification

reaction activation energy by 2.8 kcal/mol (2Int → 2TS, Figure 5.5, Table 5.2), compared to that in its absence (Reac → 1TS1, Figure 5.2). This result is in concert with findings of our experimental collaborators, i.e., methylation of C-2 lowers the reaction conversion from 63% to 29%. It is also noteworthy that the effect of the acidic proton is considerably weaker than that of the anion, as evidenced by the DFT results (2.8 vs. 28.3 kcal/mol in the barrier height reduction) and confirmed by experimental results.

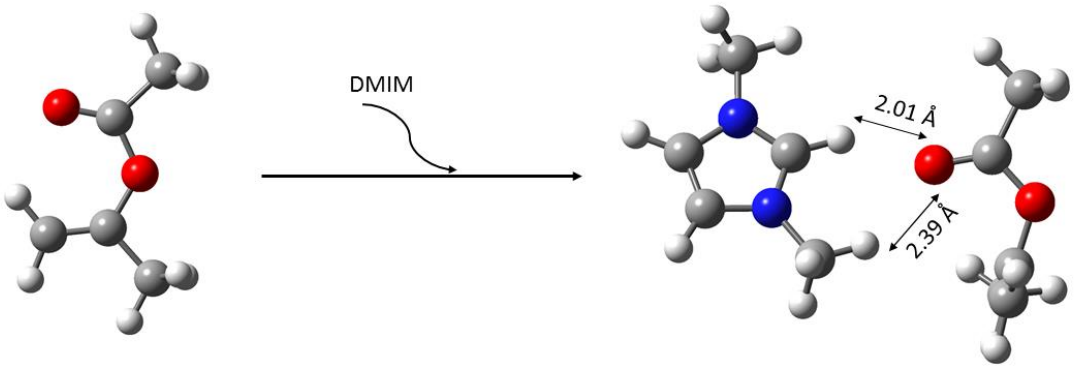

Figure 5.4. Deformation of isopropenyl acetate structure upon interaction with 1,3-dimethylimidazolium (DMIM). In the absence of DMIM, all carbon and oxygen atoms of the ester lie on a single plane; i.e., the plane defined by three C atoms of the isopropenyl group and the plane defined by two O and two C atoms of the acetate group are co-planar. Upon interaction with DMIM, the isopropenyl group twists along the O-C bond such that the two planes become perpendicular. Color code: O, N, C and H atoms are shown in red, blue, dark grey, and light grey, respectively.

In view of the experimental and computational results discussed above, we propose a reaction mechanism for the transesterification reaction of alcohol and ester catalyzed by imidazolium based ILs as follows (Figure 5.6): First, the O—H group of alcohol is activated by acetate anions, while the carbonyl group of ester is activated by interacting

with acidic proton of the ILs. Next, alcohol and ester thus activated couple to form a transition state, characterized by a strong C---O interaction between the two. Eventually, this activated complex becomes a product with the conversion of the C---O interaction to a new ester bond and the release of ions for the regeneration of the catalytic species (Figure 5.6).

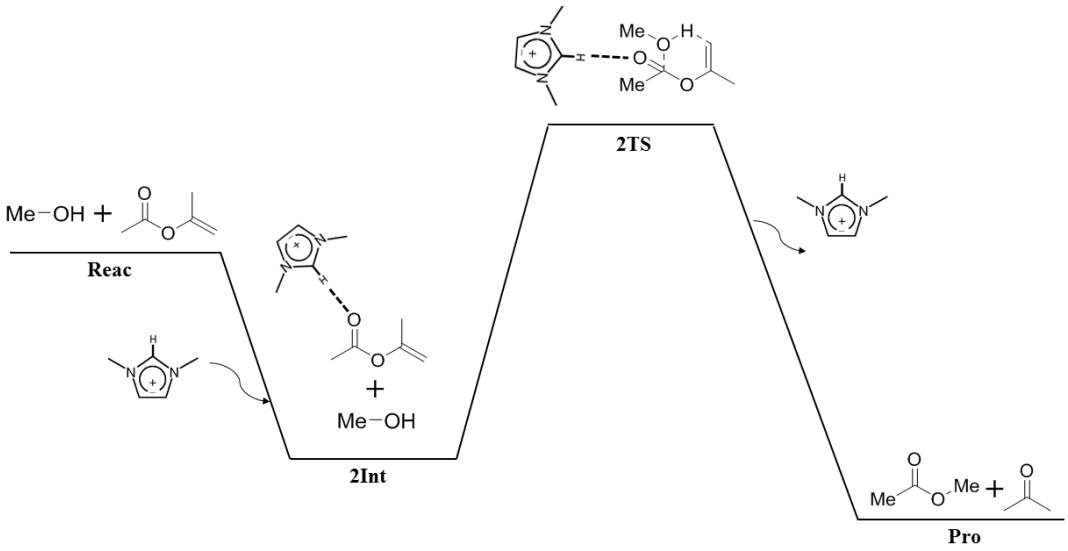

Figure 5.5. Proposed reaction Mechanism 2 for transesterification reactions in the presence of a 1,3-dimethylimidazolium cation. The calculated energies for different steps are given in Table 5.2.

Table 5.2. DFT results for ΔE for elementary steps of Mechanism 2 (Figure 5.4).

Step	ΔE(kcal/mol)
Reac → 2Int	-15.8
2Int → 2TS	28.1
2TS → Pro	-37.3

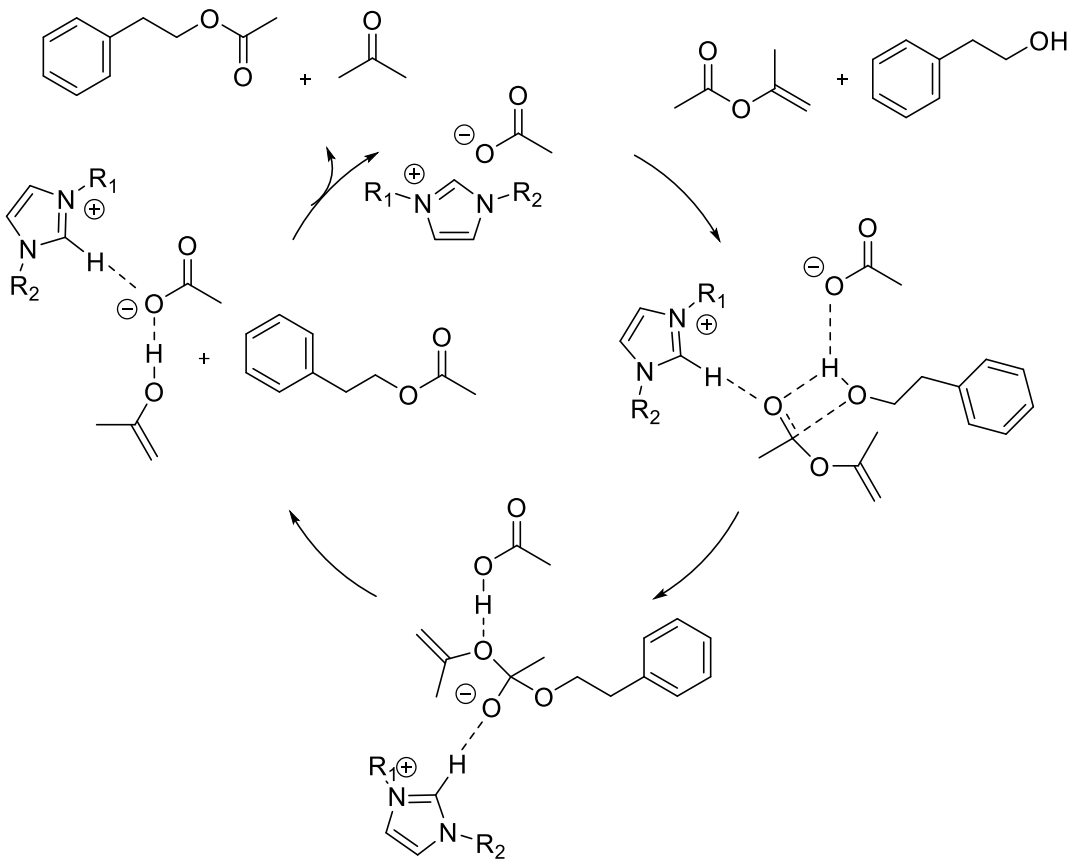

Figure 5.6. Plausible reaction mechanism for the transesterification reaction of 2-PA and IPA catalyzed by imidazolium acetates.

According to the proposed reaction mechanism, the promotional effects of the ILs is mainly because of hydrogen bond formation between IL anions and alcoholic species. This mechanism suggest that the addition of an aprotic solvent, such as DMSO, that interacts with ILs cations would have a large influence on the reactions conversion. Isolation of cations by DMSO would facilitate the generation of "naked" anions by dissociation of ion pairs.[26,27] This, based on the proposed mechanism, would promote the reactivity of hydroxyl group of reactants. To test this, our experimental collaborators performed the reactions in the presence of DMSO. As expected, conversion of transesterification reaction between 2-PA and IPA was considerably increased with the

addition of DMSO, compared to the reaction in the absence of the co-solvent (Figure 5.7).[15] This indicates that our computational analysis via DFT, though qualitative, properly captures energetics of transesterification reaction.

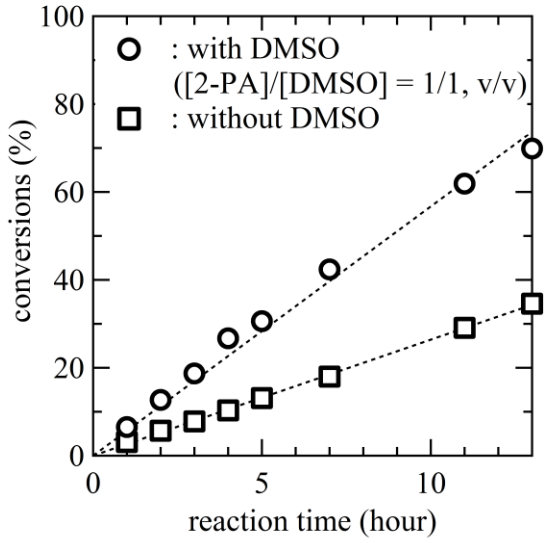

Figure 5.7. An effect of DMSO addition on the transesterification reaction of the 2-PA and IPA catalyzed by EmimOAc (line; guidance).[15]

5.5 Conclusions

Using DFT calculations, molecular insights are provided into the organocatalytic properties of imidazolium salts for transesterification reactions. Our results on a model reaction system show that reactions are most probably facilitated by anionic species of ILs. The computational analysis could successfully lead our experimental collaborators to strategically apply co-solvent effect to increase conversion rate of the cellulose modification reactions in the presence of ILs.

5.6 Acknowledgments

This work was supported in part by NSF Grant No. CHE-1223988.

5.7 References

1) H. Kopetz, *Nature*, 2013, **494**, 29-31.
2) R. Rinaldi, *Angew. Chem. Int. Ed*., 2014, **53**, 8559-8560.
3) R. P. Swatloski, S. K. Spear, J. D. Holbrey and R. D. Rogers, J. Am. Chem. Soc., 2002, **124**, 4974-4975.
4) M. Gericke, P. Fardim and T. Heinze, Molecules, 2012, **17**, 7458-7502.
5) A. Pinkert, K. N. Marsh, S. Pang and M. P. Staiger, *Chem. Rev*., 2009, **109**, 6712-6728.
6) A. Jordan and N. Gathergood, *Chem. Soc. Rev*., 2015, **44**, 8200-8237.
7) N. V. Plechkova and K. R. Seddon, *Chem. Soc. Rev*., 2008, **37**, 123-150.
8) H. Wang, G. Gurau and R. D. Rogers, *Chem. Soc. Rev*., 2012, **41**, 1519-1537.
9) F. Zhou, Y. Liang and W. Liu, *Chem. Soc. Rev*., 2009, **38**, 2590-2599.
10) W. Miao and T. H. Chan, Acc. *Chem. Res*., 2006, **39**, 897-908.
11) J. Dupont, R. F. de Souza and P. A. Z. Suarez, *Chem. Rev*., 2002, **102**, 3667-3692.
12) Q. Zhang and J. n. M. Shreeve, *Chem. Rev*., 2014, **114**, 10527-10574.
13) T. Welton, Coord. *Chem. Rev*., 2004, **248**, 2459-2477.
14) R. Kakuchi, M. Yamaguchi, T. Endo, Y. Shibata, K. Ninomiya, T. Ikai, K. Maeda and K. Takahashi, *RSC Adv*., 2015, **5**, 72071-72074.
15) R. Kakuchi, R. Ito, S. Nomura, H. Abroshan, K. Ninomiya, T. Ikai, K. Maeda, H. J. Kim and K. Takahashi, *RSC Adv*., 2017, **7**, 9423-9430.
16) C. Peng and H. Bernhard Schlegel, Isr. J. Chem., 1993, 33, 449-454.
17) C. Peng, P. Y. Ayala, H. B. Schlegel and M. J. Frisch, J. Comput. Chem., 1996, 17, 49-56.
18) A. D. Becke, Phys. Rev. A, 1988, 38, 3098-3100.
19) C. M. Breneman and K. B. Wiberg, J. Comput. Chem., 1990, 11, 361-373.
20) C. I. Bayly, P. Cieplak, W. Cornell and P. A. Kollman, J. Phys. Chem., 1993, 97, 10269-10280.
21) A. D. Becke, J. Chem. Phys., 1993, 98, 5648-5652.
22) J. C. Burant, G. E. Scuseria and M. J. Frisch, J. Chem. Phys., 1996, 105, 8969-8972.
23) A. Laio, J. VandeVondele and U. Rothlisberger, J. Phys. Chem. B, 2002, 106, 7300-7307.
24) R. D. Gaussian 09, , M. J. Frisch, G. W. Trucks, H. B. Schlegel, G. E. Scuseria, M. A. Robb, J. R. Cheeseman, G. Scalmani, V. Barone, B. Mennucci, G. A. Petersson, H. Nakatsuji, M. Caricato, X. Li, H. P. Hratchian, A. F. Izmaylov, J. Bloino, G. Zheng, J. L. Sonnenberg, M. Hada, M. Ehara, K. Toyota, R. Fukuda, J. Hasegawa, M. Ishida, T. Nakajima, Y. Honda, O. Kitao, H. Nakai, T. Vreven, J. A. Montgomery, Jr., J. E. Peralta, F. Ogliaro, M. Bearpark, J. J. Heyd, E. Brothers, K. N. Kudin, V. N. Staroverov, R. Kobayashi, J. Normand, K. Raghavachari, A. Rendell, J. C. Burant, S.

S. Iyengar, J. Tomasi, M. Cossi, N. Rega, J. M. Millam, M. Klene, J. E. Knox, J. B. Cross, V. Bakken, C. Adamo, J. Jaramillo, R. Gomperts, R. E. Stratmann, O. Yazyev, A. J. Austin, R. Cammi, C. Pomelli, J. W. Ochterski, R. L. Martin, K. Morokuma, V. G. Zakrzewski, G. A. Voth, P. Salvador, J. J. Dannenberg, S. Dapprich, A. D. Daniels, Ö. Farkas, J. B. Foresman, J. V. Ortiz, J. Cioslowski, and D. J. Fox, Gaussian, Inc., Wallingford CT, 2009.
25) F. G. Bordwell, Acc. Chem. Res., 1988, 21, 456-463.
26) A. Xu, Y. Zhang, Y. Zhao and J. Wang, Carbohyd. Polym., 2013, 92, 540-544.
27) W. R. Fawcett, P. Brooksby, D. Verbovy, I. Bakó and G. Pálinkás, J. Mol. Liq., 2005, 118, 171-178